UNIVERSITY OF SOUTHAMPTON

A Far Ultraviolet Study of the Globular Clusters NGC 1851 & NGC 6681

by

David R. Zurek

A thesis submitted in partial fulfillment for the degree of Doctor of Philosophy

in the

Faculty of Physical Sciences and Engineering

Physics and Astronomy

July 2017

UNIVERSITY OF SOUTHAMPTON

ABSTRACT

FACULTY OF PHYSICAL SCIENCES AND ENGINEERING
PHYSICS AND ASTRONOMY

Doctor of Philosophy

by David R. Zurek

I present a far-ultraviolet study, taken with the Hubble Space Telescope (HST), of the globular clusters NGC 1851 and NGC 6681. My focus is primarily on the time-domain, and I present searches for – and classification of – far-ultraviolet variables and transients in my data. The far-ultraviolet sources have been cross-identified with objects detected at near-ultraviolet and optical wavelengths in archival HST imaging. The combined photometric catalogs were used to identify several core populations, including some that are likely to be binaries containing a hot component.

In NGC 1851, I identified 36 variable candidates in the 273 exposures taken over 3 HST visits of 4 orbits each. Twenty five of the variable candidates are distributed along the horizontal branch, 12 are likely RR Lyraes and 13 are on the blue horizontal branch. Five variable candidates are located among the blue straggler populations with one of them a likely SX Phoenicis pulsator. The remaining six variable candidates have photometric properties that point to white dwarf + main sequence binary systems.

One of the far-ultraviolet variables in NGC 1851, **FUV1**, was found to have a period of ~ 18 minutes in our far-ultraviolet time-series photometry. The two possibilities for the nature of this far-ultraviolet variable are: (i) it may be an intermediate polar (i.e. a compact binary containing an accreting magnetic white dwarf), or (ii) it may be an AM CVn (i.e. and interacting double-white dwarf system). The AM CVn interpretation is favoured because of the lack of an X-ray detection in $\simeq 65$ ksec of Chandra imaging.

I also present a search for transients (e.g. dwarf novae) in ~ 20 years of far-ultraviolet imaging of the core of globular cluster NGC 6681. No such transients were found in the ~ 80 epochs of observations. If all of these epochs can be considered independent, the search should be nearly 100% complete for dwarf novae with duty cycles $\gtrsim 5\%$, and still $\simeq 60\%$ complete for systems with duty cycles of $\approx 1\%$. The detection of of zero outbursts allows me to place a $2-\sigma$ upper limit of 3 on the mean number that might have been detected in similar surveys. This places strongish constraints on models for the cataclysmic variable populations.

Contents

List of Figures

List of Tables

Acknowledgements

I would like to thank Thomas Maccarone for being persistent in getting me to enroll in a PhD program. I would like to thank Christian Knigge for being a mentor and a friend during the PhD process and well before. The Curators, especially Michael Shara, in the Division of Physical Sciences at the American Museum of Natural History have been exceptionally understanding while I've taken time to work on my thesis. I'd like to thank Southampton University for allowing me to chase my a dream of obtaining a PhD. Finally, I'd like to thank all my friends and family who have provided enormous support in the process.

To Mom & Dad

Chapter 1

Introduction

There are approximately 150 globular clusters (GCs) that orbit throughout the Milky Way's (MW) halo and bulge (Harris 1996). GCs are generally between 10 and 13 billion years old (VandenBerg et al. 1996) and are remnants of the earliest era of galaxy formation. The present theory for the formation of galaxies (White & Frenk 1991), and thus the MW, is a hierarchical process of galaxies merging. The earliest merging galaxies were a fraction of the size of the present MW, but, over time, the range of mass ratios of merging events increased. This process continues to happen, with examples of large galaxy mergers such as the Antenae (Whitmore et al 2005) and small mergers such as the Sagittarius dwarf galaxy (Ibata et al 1994). The later is being tidally shredded by the MW and is thought to be the most common type of merger for the MW.

The study of GCs has many unique advantages over the study of the field star population. The stars in a GC can be thought of as being all at the same distance and reddening (see for example Piotto et al. 2012), thus the relative magnitudes and colours of the stars can be determined very precisely. The stars in a GC, also to first approximation, represent a "simple" stellar population, in that they have a single age and metallicity. Initially stars of all masses, $\sim 0.05 M_{\odot}$ to $\gtrsim 50 M_{\odot}$, formed in GCs, but only stars with masses $\leq 1 M_{\odot}$ exist in present-day GCs. Since there is no ongoing star formation in GCs, stars more massive than $\sim 1 M_{\odot}$ have already evolved to become black holes, neutron stars and white dwarfs. GCs contain between a few $\times 10^4$ and a few $\times 10^6$ stars today, and every evolutionary state is represented, as demonstrated by the colour magnitude diagram (CMD; Figure 1.1).

In order to interpret GC CMDs, it is helpful to construct synthetic versions for simple, single-age populations from theoretical stellar evolution models (e.g. VandenBerg 2000). These synthetic CMDs are typically referred to as isochrones. Isochrones can be used to determine the age of a cluster by fitting the magnitude and colour of the turnoff of the main sequence stars (Figure 1.2).

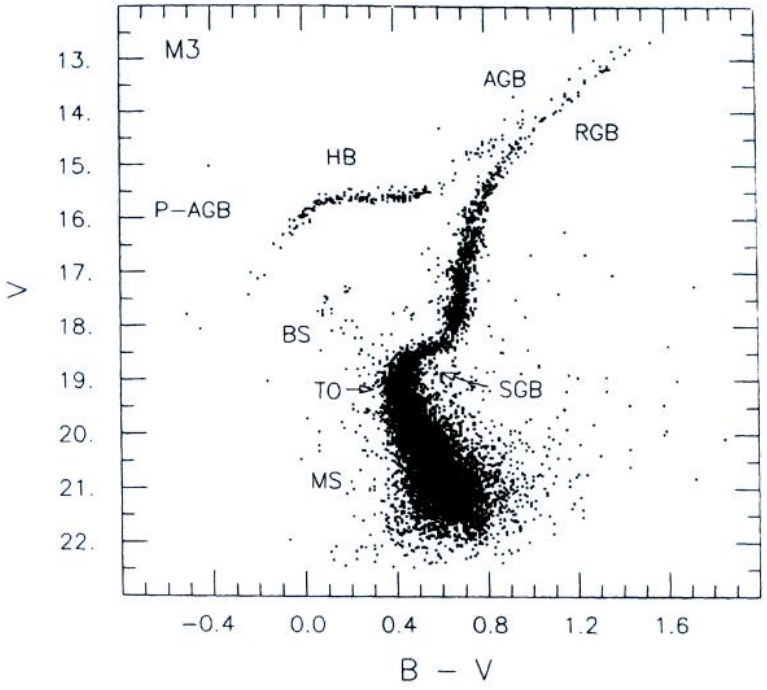

FIGURE 1.1: An example of the various populations. This CMD, from Renzini & Fusi Pecci (1988), is of the GC M3 (NGC 5272) and demonstrates the various stages of a stars evolution from the main sequence to the horizontal branch.

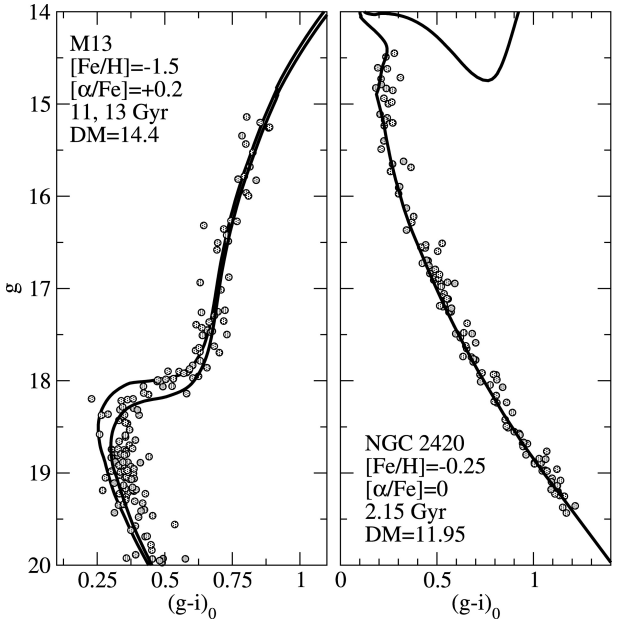

FIGURE 1.2: Figure from Dotter et al (2008) with the photometry from Lee et al (2008). These two examples demonstrate how isochrones can be used to determine ages for a wide range of cluster properties.

1.1 "Simple" Stellar Populations

The last decade has seen a revolution in our thinking about GCs. Precision photometry with second and third generation cameras on the Hubble Space Telescope (HST), the Advanced Camera for Surveys (ACS) and the Wide Field Camera 3 (WFC3), has resulted in the discovery that many (perhaps all) GCs are not "simple" single populations, but are rather composed of at least two populations and perhaps more. One of the GCs studied in this thesis, NGC 1851, has been shown to have at least two distinct populations (Milone et al. 2008). The multiple populations in NGC 1851 reveal themselves with sufficient photometric precision as a split of the subgiant branch (i.e. there are two subgiant branches; see Figure 1.3).

The existence of multiple populations in a GC may reveal itself at various stages of a star's evolution (e.g. Ω Cen; Bedin et al. 2004 and NGC 2808; Milone et al. 2012). In the following sections, we discuss these evolutionary stages – the main sequence, subgiant branch, red giant branch, horizontal branch, asymptotic giant branch and white dwarf sequence – and their relationship to the multiple populations we now know to be present in GCs.

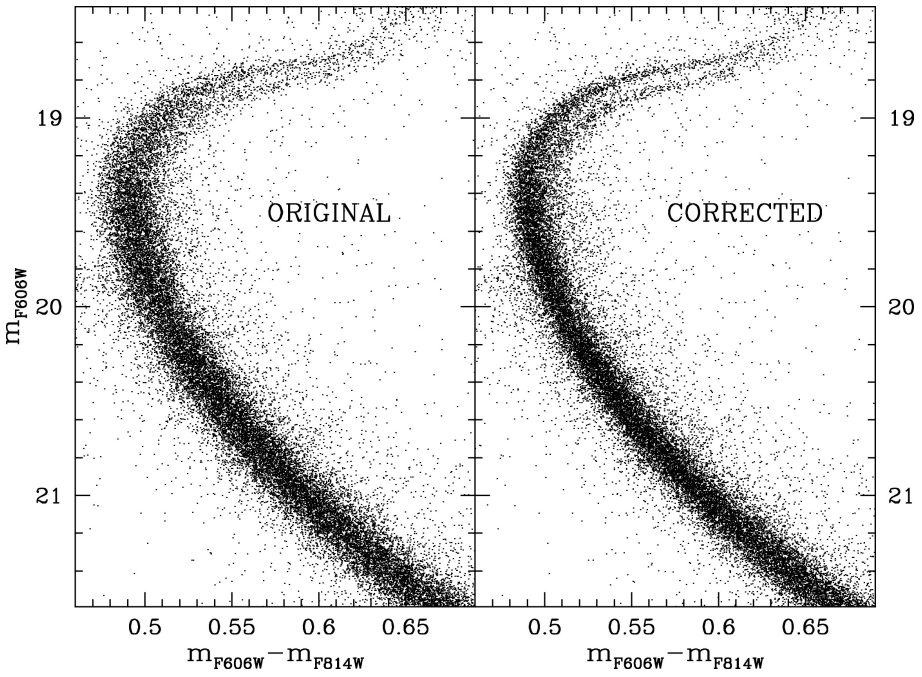

FIGURE 1.3: Figure from Milone et al (2008). Notice two concentrations of stars in the SGB region (i.e.two SGBs). The difference between the original and corrected CMDS (explained in Milone et al (2008)) is that the corrected has taken into account tiny variations in the colour and magnitude as a function of the position in the field of view. It is comforting to see the two SGBs without the correction.

1.1.1 Main Sequence

Stars spend $\sim$ 90% of their life on the main sequence (see the area labeled MS in Figure 1.1 and Figure 1.4). Once a star has formed from collapsing gas it continues to decrease in radius under its own gravity until the temperature and pressure in the star's core is large enough to initiate the fusion of hydrogen (astronomers often refer to the fusion process as "burning", though strictly speaking this is inaccurate). The star is on the MS when the outward radiative pressure produced by fusion balances the gravitational pressure. A star remains on the MS until hydrogen is exhausted in the core.

The total length of time a star is on a main sequence depends primarily on the mass of that star. A star like our Sun, with $M = 1M_{\odot}$, is on the main sequence for about 10^{10} yrs, while a star near the hydrogen burning limit, $\sim 0.08M_{\odot}$, is on the main sequence for $\gtrsim 5 \times 10^{12}$ yrs. This dependence of MS lifetime on stellar mass means that the age of a GC can be accurately obtained if the location of the point stars are leaving the main sequence can be determined. While it is difficult to directly measure the masses of stars, their luminosity, which is usually easier to estimate, can be used as a tracer, since it depends on mass roughly as

$$L = L_{\odot}(M/M_{\odot})^{3.5}$$

.

A more sophisticated method that can be used to determine the age of a GC, called isochrone fitting, was developed by stellar evolution modelers (e.g. VandenBerg et al. 2014). An isochrone is the result of extracting the luminosity and temperature from the stellar evolution models for stars from $\sim 1.2M_{\odot}$ to $\sim 0.4M_{\odot}$ at the same age. Overlaying isochrones onto the colour magnitude diagrams of GCs allows the age to be determined by the "best" fit isochrone. (It should be noted that in general the determination of "best" fit is done "by eye".)

Multiple populations are evident in some GCs such as NGC 5139 (Ω Cen; Bedin et al. 2004) and NGC 2808 (Milone et al. 2012) as distinct main sequences. In other GCs, like NGC 104 (47 Tuc; Anderson et al. 2009), the main sequence is wider than photometric errors allow. This suggests that the GC was created during an extended period of star formation or from an inhomogeneous gas reservoir (or both).

The two GCs studied in this thesis, NGC 1851 and NGC 6681, have main sequences consistent with a single sequence, though, at least in the case of NGC 1851, a splitting into two populations can be seen at the turn off and onto the sub giant branch (Figure 1.3). The MS turn-off indicates the end of core hydrogen burning. Stars located at this point of the CMD contain a core composed mainly of helium, while hydrogen continues to be

fused in a shell surrounding the core. Beyond this point, stars begin to cool and enter the subgiant branch stage of their evolution.

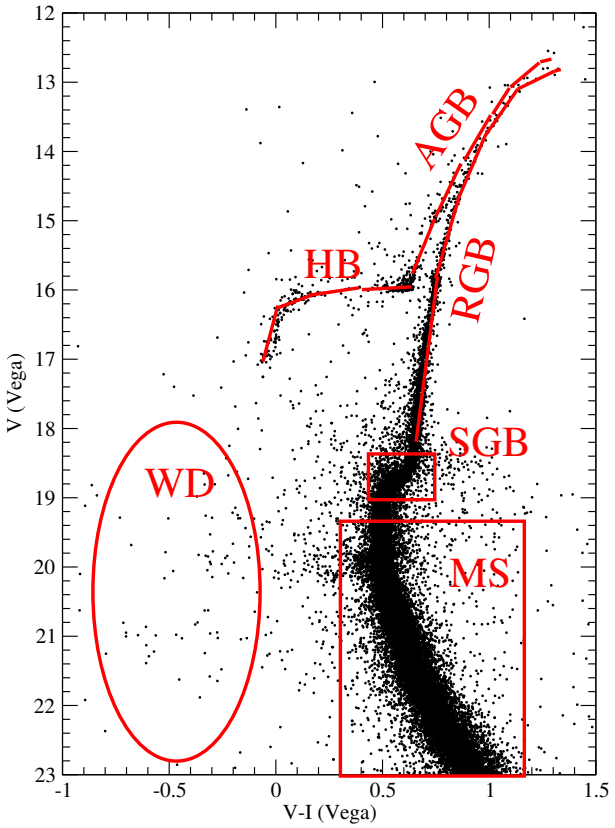

FIGURE 1.4: The optical CMD for NGC 1851 with the Photometry from Milone et al (2008). We have labeled the various stages of stellar evolution.

1.1.2 Subgiant Branch

Once a star has exhausted the hydrogen in the core, the star leaves the main sequence and begins to cool. The star's structure now consists of mostly a helium core, with hydrogen being burned in a shell around the core. The core itself is producing less energy and begins to cool and collapse. The hydrogen burning shell is producing more energy, which is mostly being put into the volume of the star outside the hydrogen burning shell. The heated outer parts of the star then expand to compensate for this energy input. (Note: This is a somewhat simplistic explanation of the process, but a better simple explanation has yet to be found though all stellar evolution models produce this outcome.)

Observationally, even this evolutionary stage is seen in the CMD of a GC as the distribution of stars from the top of the main sequence to the base of the red giant branch (Figure 1.1 and Figure 1.4). This distribution, depending on the filters chosen, is spread out mostly in colour (or temperature) rather than luminosity.

If a cluster, such as NGC 1851, has multiple populations, it is this location where it is often most evident (Figure 1.3). The implication for the two distinct populations in NGC 1851 is that most of the difference between the two populations is age (Milone et al. 2008) while in a cluster such as NGC 2808, which also exhibits multiple main sequences, there is also a clear difference in chemical composition (i.e. the abundances) of the sequences (Milone et al. 2012).

A star can be considered to be on the red giant branch once most of its change is an increasing radius (and thus luminosity).

1.1.3 Red Giant Branch

As a star evolves from the subgiant branch, its changing position in the CMD is mainly determined by its increasing radius. The star still decreases in temperature but the increase in radius (and luminosity) is significantly greater than the decrease in temperature. Specifically, the luminosity of the star depends on radius and temperature as

$$L \propto R^2 T^4,$$

and even though the temperature of the star is still decreasing slightly along the red giant branch (RGB), this is greatly outweighed by the tremendous increase in its radius. As a result, the star's luminosity increases significantly, and it moves up almost vertically in the CMD.

While the star is expanding, two essential things are occurring which relate to the future evolution of the star. The first thing is that hydrogen continues to burn in a shell around the helium core. This hydrogen burning shell moves outwards as it exhausts the hydrogen, leaving helium "ash" behind and increasing the size and mass of the core. The evolution along the RGB is terminated when the helium core reaches sufficient mass and pressure to ignite helium. This ignition is known as the helium flash. Once this occurs, the star continues its evolution on the horizontal branch.

The second essential thing which occurs to a star on the RGB is mass loss in the form of stellar winds. This significantly reduces the mass of the star and thus affects its future evolution. The empirically determined mass loss relation for RGB stars known as Reimers Law (Reimers 1975), which is still used today, is

$$\dot{M} = 4 \times 10^{-13}\, \eta_{\mathrm{R}}\, \frac{LR}{M} [\mathrm{M}_{\odot}\mathrm{yr}^{-1}],$$

where $\dot{M}$ is the mass loss rate in solar units, L is the luminosity, R is the radius, M is the mass, and $\eta_{\rm R}$ is an efficiency scaling factor of order unity. McDonald & Zijlstra (2015) found that $\eta_{\rm R} = 0.477 \pm 0.070$ from their in depth examination of $\eta_{\rm R}$. Their study found no significant dependence of $\eta_{\rm R}$ on abundance. The mass loss on the red giant branch determines the distribution of the stars on the horizontal branch and their subsequent evolution.

1.1.4 Horizontal Branch

The helium flash at the tip of the red giant branch ignites helium in the core of the star. The star then quickly (on a time-scale of a few thousand years) moves to the horizontal branch (see the line labeled HB in Figure 1.4) and continues its evolution. The colour/temperature at which the star begins its subsequent evolution is dictated by the amount of mass lost on the RGB (as mentioned above). This appears to depend on metallicity, [Fe/H]. Metal poor (low [Fe/H]) clusters contain predominately blue/hot HB stars, while more metal rich (high [Fe/H]) clusters have redder/cooler HB populations. This dependence on [Fe/H] is a result of two effects: (1) low [Fe/H] GCs are generally older, and therefore the stars have a lower mass and envelope mass; (2) RGB stars in low [Fe/H] GCs are hotter than RGB stars in higher [Fe/H] GCs, so their luminosity is higher. As can be seen from the equation for $\dot{M}$ above, this is expected to result in a higher mass loss rate on the RGB in lower-[Fe/H] GCs.

A star on the HB is fusing helium in the core and may also continue to fuse hydrogen in a shell surrounding the core. The amount of mass lost on the RGB determines if there is enough material in the outer envelope to continue hydrogen shell burning. When the star exhausts helium in the core, leaving carbon-oxygen as a product of that burning, the star evolves similarly to a main sequence star exhausting hydrogen in its core. Specifically, the star increases in radius and cools, thus beginning its evolution on to the asymptotic giant branch. If, however, most of the outer envelope of the star was lost prior to arriving on the horizontal branch, it may bypass the asymptotic giant branch evolution and evolve directly to the white dwarf cooling sequence (Brown et al. 2010).

While metallicity is the dominant parameter that determines the shape of a cluster's horizontal branch (presumably via its effect on mass loss along the RGB), it cannot fully account for the diverse morphologies of GC horizontal branches. This long-standing issue in GC research is known as the second-parameter problem.

1.1.4.1 The Second-Parameter Problem

The second-parameter problem refers to clear differences in the HB morphologies for GCs with similar ages and metallicities. An example of this is the GC pair NGC 288

and NGC 362. NGC 288 has a predominantly blue HB, while NGC 362 has a red HB (Figure 1.5). These two clusters have been thought to have nearly the same age and metallicity. The HB discrepancy between two clusters such as these is known as the second-parameter problem, since the first parameter determining HB morphology is metallicity, [Fe/H]. (See Stetson et al 1996 and Sarajedini et al 1997 for extensive discussions of these GCs and the second parameter.)

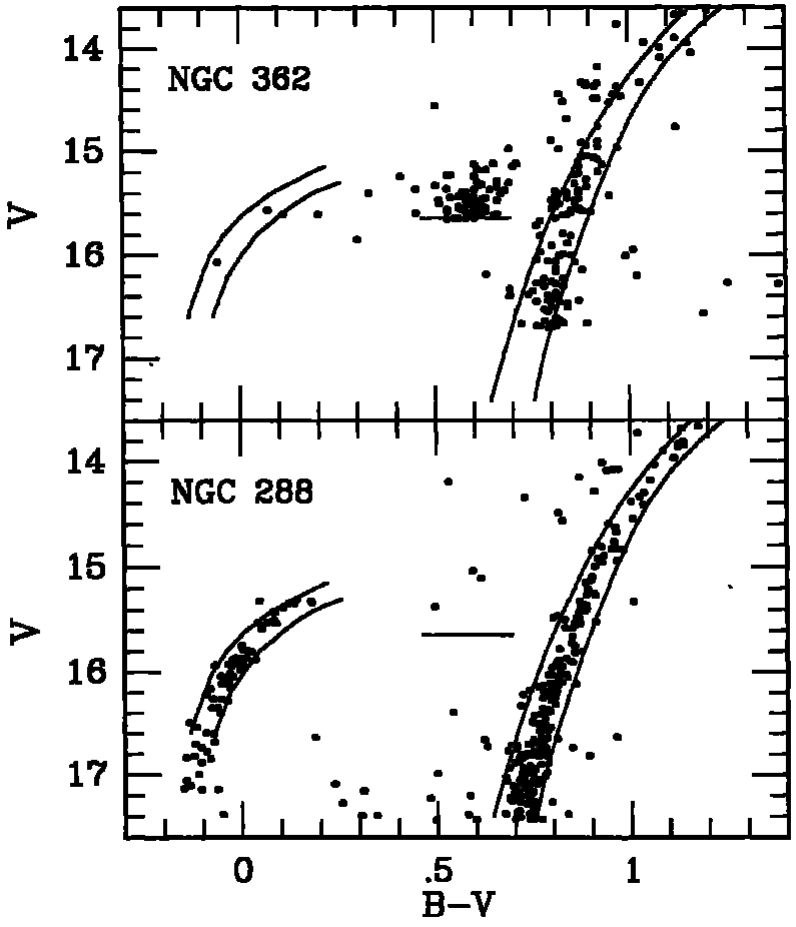

FIGURE 1.5: Figure from Stetson et al (1996) comparing the two GCs NGC 362 and NGC 288. The photometry for NGC 362 is from Bergbusch (1993) and the photometry for NGC 288 is from Harris (1982). The distributions of HB stars are completely different between these two clusters but the [Fe/H] and age are apparently very similar.

One of the interesting things about one of the clusters being studied here, NGC 1851, is that it apparently exhibits the second parameter problem in a single cluster (Figure 1.6). In other words, its HB is split into two distinct groupings. One grouping is located on the hot or blue end of the HB, the other on the cool or red end of the HB.

The relatively recent discovery of two populations on the SGB of NGC 1851 (Milone et al. 2008) may suggest a solution for the second parameter problem in this cluster. If a direct relationship can be drawn between the HB morphology and the SGB populations,

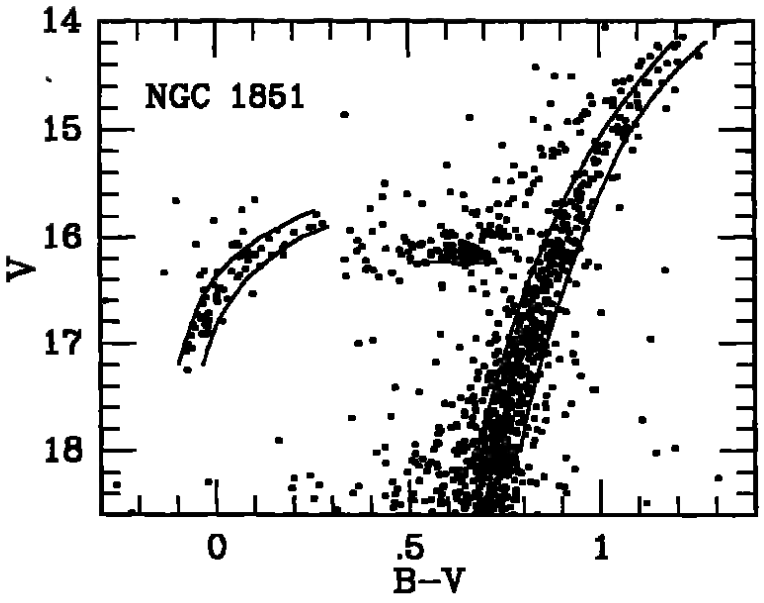

FIGURE 1.6: Figure from Stetson et al (1996) with the photometry coming from Walker (1992). The two distributions of HB stars are clearly visible. The lines drawn are the same lines in Figure 1.5.

this would produce a more complete picture of the processes that determine a stars location on the HB.

1.1.5 Asymptotic Giant Branch

Once a star exhausts helium in the core, it begins to cool while continuing to burn helium in a shell around the carbon-oxygen core. The star expands and cools, like on the sub-giant branch and red giant branch, thus increasing in luminosity while becoming redder. Mass loss, similar to what occurs on the red giant branch, takes place. However, since asymptotic giant branch (AGB) stars reach a higher luminosity and lower temperature than RGB stars, dust is thought to form in the atmosphere of an AGB star. Radiation pressure on their dust causes an increased mass-loss rate. The result is that the entire outer envelope is lost from the star, leaving a hot remnant composed mostly of carbon and oxygen. The total mass and pressure exerted on the carbon-oxygen remnant is insufficient to ignite, even though initially it is very hot ($> 150,000$ K). The post-AGB remnant then cools and contracts towards the white dwarf sequence.

1.1.6 White Dwarfs

All stars less massive than about $8M_{\odot}$ (Reimers & Koester 1982) end their lives as white dwarfs (WDs). Most white dwarfs are composed of carbon and oxygen, with a thin layer

of helium and/or hydrogen on the surface. The most massive white dwarfs, which are likely the remnants of higher mass stars (i.e. $\sim 8M_{\odot}$), may be composed of oxygen and neon (Gil-Pons et al. 2005). These objects may exist in globular clusters, but are expected to be extremely faint ($> 25^{th}$ magnitude in V or F606W), since they have had more than 10 Gyrs to cool down (Hansen et al. 2007).

The lowest mass stars (i.e. $< 0.5M_{\odot}$) evolve to form white dwarfs composed of helium rather than carbon and oxygen. However, unless something happens to affect a star's evolution, these stars will take many tens of Gyrs to evolve to the point of producing a helium white dwarf. Helium white dwarfs likely do exist in globular clusters, though not as a result of single star evolution. We discuss these objects in the next section.

A white dwarf's evolution is dictated by its rate of cooling. Young white dwarfs in the immediate aftermath of the AGB are hot (Teff $> 10^5$ K) and, they cool monotonically, reaching Teff $\sim 10^4$ K after $\sim 10^9$ years. The region labeled WD in Figure 1.4 may contain hot WDs, but most of single WDs are fainter than the limits plotted in Figure 1.4 and are likely at magnitudes of ~ 27 (see Hansen et al. 2007). All white dwarfs end up at these very faint and cool magnitudes and colours unless they are reheated by some mechanism. These mechanisms are discussed in the next section.

1.2 Exotic Populations, Binaries and Variables

In the previous sections I described how the vast majority of stars evolve – MS $\rightarrow$ SGB $\rightarrow$ RGB $\rightarrow$ HB $\rightarrow$ AGB $\rightarrow$ WD – whether they are in a cluster or in the field. Stars can deviate from this relatively simple evolution through interactions with other stars. Interactions in the field are limited to interactions between small numbers ($\lesssim 5$) of stars, with most of the interactions occurring in binaries (two stars). Observations indicate that about 50% of the stars in the field population are binaries (Parker & Meyer 2014). The fraction of those binaries actually in triples or quadruples is an unknown, and it may be that as much as 50% of the binaries are actually higher-order multiple systems (Elliott et al. 2014).

In a GC, the number density of stars is orders of magnitude higher than in the field. This greatly increases the probability that a star will interact with one or more other stars over its lifetime. These interactions mean that binaries (or multiple systems) with large separations do not survive for a long period of time.

Another process that occurs in clusters is mass segregation. Roughly speaking, this can be understood as a form of energy equipartition enforced by dynamical interactions between cluster members. Such interactions tend to rob massive objects of kinetic energy, causing them to sink to the cluster core. By contrast, low-mass objects tend to gain kinetic energy in dynamical encounters, causing them to move to the periphery

of the cluster. Since binaries and other multiple stars are typically more massive than single stars, they are expected to become more centrally concentrated over time. This in turn increases the number of interactions that each of these systems undergoes, as they reside within a region of higher density.

It has been shown, through N-body simulations (Portegies Zwart, et al. 1997), that interactions with binaries typically result in a binary with a smaller separation and a third star with added kinetic energy. It should be noted that the resultant binary may not be composed of the same two stars that were in the binary prior to the interaction. It should also be noted that the single star at the end of the encounter could have sufficient velocity to escape the cluster. It is through processes like this that a globular cluster loses mass over its lifetime. It is also through processes like this that "exotic" systems are produced.

The separation at which binaries survive in a globular cluster is known as the hard-soft boundary and is related to the Heggie-Hills law (Heggie 1975; Hills 1975): *Soft binaries soften and cool a cluster, while hard binaries harden and heat a cluster.*

While it is true that all of the "exotic" populations found in globular clusters do exist in the field, it is the stellar dynamics in GCs, and the associated star-star, binary-star, and binary-binary interactions, which increase the number of these "exotic" objects (Di Stefano & Rappaport 1994). The results of all these interactions between stars, binaries and triples are thought to increase the production of stellar exotica, including low mass X-ray binaries, millisecond pulsars, blue stragglers, cataclysmic variables, helium white dwarfs, and sub-sub-giant branch stars (e.g. Geller et al. 2017, Bahramian et al. 2013, and, Ivanova et al. 2006). They may even alter the distribution of stars on the horizontal branch (Pasquato et al 2014). Each of these systems are discussed below.

1.2.1 Blue Stragglers

It was noticed early on in the study of globular clusters (Sandage 1953) that there appeared to be stars which were younger and more massive than the turnoff stars. As more clusters were investigated, it was found that these stars are in fact common and appear to exist in all old ($\sim$ 1 Gyr) stellar clusters (both globular and open clusters). Their location in the CMD (Figure 1.7) implies that these stars are more massive than turnoff stars and are on or near the main sequence. This gives the appearance that these stars are "straggling" behind the main population of stars in their evolution. They are also typically blueward of the turnoff colour, thus giving us the name – blue straggler (BSS).

The fact that blue stragglers are brighter than turnoff stars implies that they are more massive than turnoff stars as well. It could be that they are composed of more than one star, such as a binary, and therefore brighter because we see the combined light of

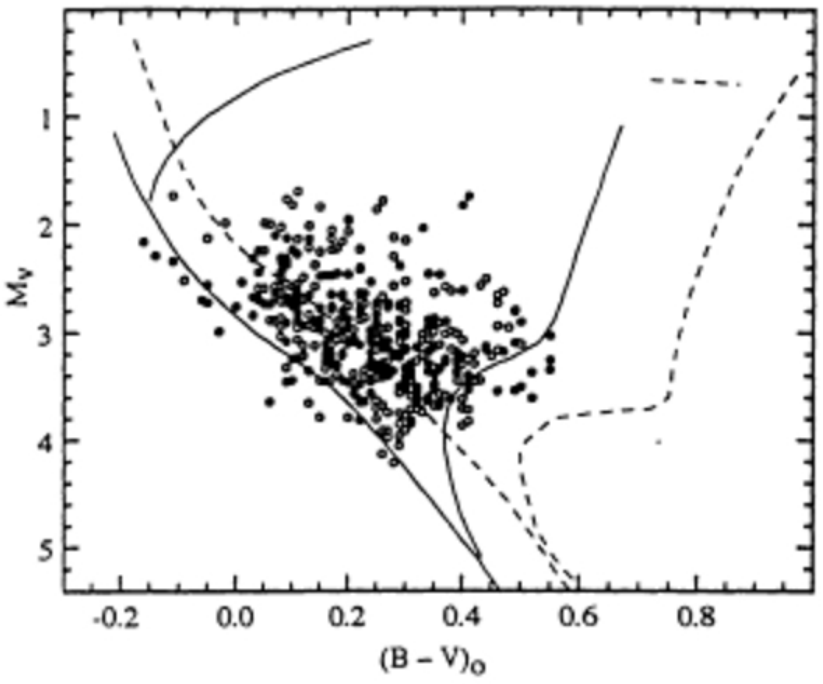

FIGURE 1.7: Hertzsprung-Russell diagram of 409 GC blue stragglers (from Bailyn 1995). The solid lines represent the stellar sequences from the metal-poor ([Fe/H]~ -2.31) GC M92 (NGC 6341). The dashed lines are the same stellar sequences from the metal-rich ([Fe/H]~ -0.72) GC 47 Tucanae (NGC 104).

multiple stars. If a blue straggler is a binary composed of normal main sequence stars, then the brightest it could be is 0.75 magnitudes brighter than the turnoff magnitude. This is because turnoff stars are the most massive stars in the cluster, and therefore the most massive binary is an equal-mass binary composed of two turnoff stars. Such a binary has twice the luminosity of its components, which corresponds to a brightness increase of $2.5log(2) \simeq 0.75$ magnitudes.

There are certainly blue stragglers which are $\lesssim 0.75$ magnitudes brighter than the turnoff and, some or all of those could be binaries. However, there are also blue stragglers which are one or more magnitudes brighter than the turnoff. A simple binary model thus cannot account for all sources defined as blue stragglers.

As the stellar densities are higher in a cluster, it is possible that collisions between single stars could take place, though the number of such collisions (~ 90) over the lifetime of the average GC is small (Hills & Day 1976). This means that direct collisions between single stars, probably do not contribute significantly to the BSS population.

If instead of single stars we consider binaries, which present a much larger interaction cross-section, we find the probability of a close encounter is significantly larger (Chatterjee et al. 2013). These encounters can lead to a number of outcomes. They can (1) alter the binary parameters, but leave the stars in the binary unchanged; (2) cause stars

to swap into and out of binaries involved; (3) lead to direct collisions between one or more of the interacting stars (Chatterjee et al. 2013).

Direct collisions are the least likely outcome of any one interaction and would produce similar systems to the single-single collisions mentioned above (Chatterjee et al. 2013). However, the cumulative effect of several interactions (or the subsequent stellar/binary evolution) can produce systems in which mass is exchanged between two stars.

If one of the stars in the binary evolves onto the subgiant branch, thus increasing in radius, its the outer envelope may transfer to the other star in the binary, thus increasing its mass. The resulting binary will contain a more massive star with a naked stellar core as a companion. The naked stellar core in turn will become a helium white dwarf (we discuss these in detail below).

Finally, it is possible that the binary may evolve so that the two stars enter into a common envelope, in which case the stars may inspiral toward each other and merge (Iaconi et al. 2017; Ivanova & Nandez 2016). Note this is distinct from a collision as the timescale of such a merger is significantly longer. It is also expected that the stellar structure of the resulting object will be different from that of a collision product.

Recent studies have revealed evidence for one of these outcomes. Gosnell et al (2014) have shown that some of the BSS in the old open cluster NGC 188 have an ultraviolet excess consistent with hot low-mass white dwarf companions. While this result is for an old open cluster, it is expected that such systems exist in globular clusters as well.

It should be noted that BSS do occur in the field also. It is unknown how common BSS are in the field, as the identification of them as BSS is much more difficult than in a cluster. In a cluster, the CMD makes it easy to identify likely BSS. In the field population, a CMD is not useful as the field stars could have a wide distribution of distances and ages. We note that the European Space Agencies Gaia mission will provide distances and proper motions for a large fraction of the Galaxy, and this will make identifying field BSS significantly easier. Presently, the identification of a field star as a BSS requires an accumulation of circumstantial evidence, as demonstrated by Schirbel et al (2015).

Until recently it was unknown if collisions or mass exchange through binary evolution and interactions was the dominant mechanism for the creation of BSS. However, Knigge et al. (2009) and Leigh et al. (2010) show – via an examination of the BSS populations in the cores of about 50 GCs that the dominant BSS formation mechanism appears to involve binaries.

There are a number of BSS that, given their location in the CMD, appear to have masses in excess of twice the turnoff. This would seem to indicate that the binary process occurs multiple times and/or collisions do occur, even if they may not be the dominant BSS formation mechanism. The number of binaries, cluster density and cluster mass all seem

to be important factors with regards to the total blue straggler population. In this thesis, I have attempted to identify the blue stragglers in the GC NGC 1851 and determine if they are in binaries and/or have an ultraviolet excess indicative of a hot companion.

1.2.2 Cataclysmic Variables

Cataclysmic variables (CVs) are binaries composed of a white dwarf and (typically) a main sequence star. The binary has a separation such that the main sequence star is filling its Roche lobe. The Roche lobe is the volume around each star in a binary system in which the material is bound to the star. If a star in a binary system fills its Roche lobe, mass is transferred through the inner Lagrangian point to its companion (Figure 1.8). In a CV, the mass gainer is a WD.

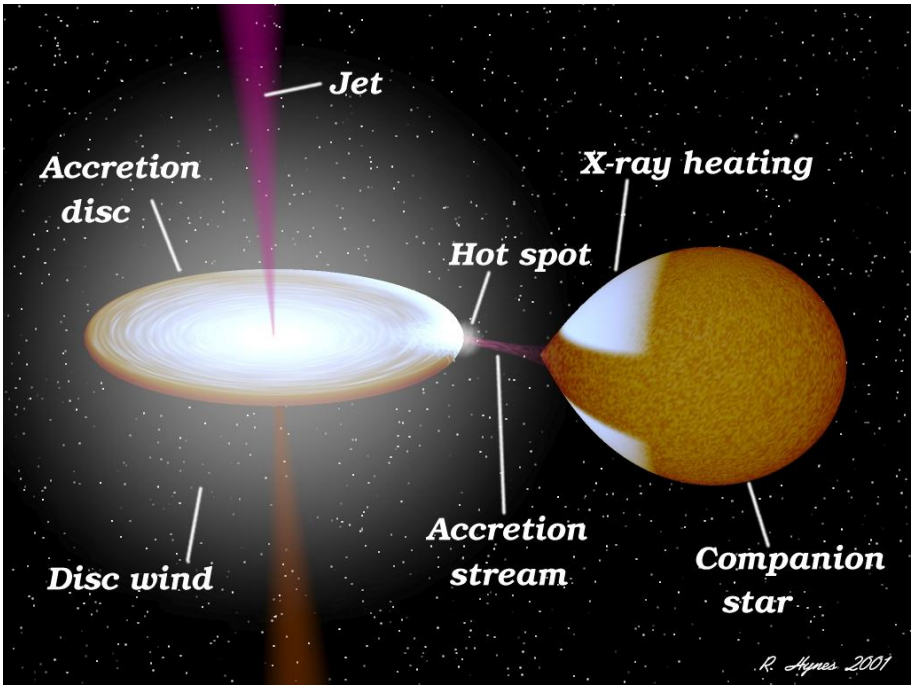

FIGURE 1.8: The process of mass transfer from a Roche lobe filling main sequence star onto a white dwarf (copyright Rob Hynes 2001).

There are two broad families of CVs: magnetic and non-magnetic. The astrophysics community has defined a plethora of subclasses within each of these broad families. For our purposes, this detailed classification scheme is unnecessary. Instead, we will simply consider non-magnetic CVs (in which the WD always accretes via an accretion disk), magnetic systems that contain at least a partial disk around the WD, and magnetic systems in which the accretion flow is channeled entirely along the magnetic field lines anchored on the WD.

The material from the main sequence companion in a non-magnetic CV forms an accretion disk that extends to the surface of the white dwarf, where the material is deposited

(e.g. Figure 1.8). In some systems – the so-called dwarf novae – the accretion disk is subject to an instability, as a result of which material is transferred onto the WD in quasi-periodic (i.e. weeks to years) bursts. During these outbursts, the system brightens by several magnitudes.

If the accumulation of material on the surface of the white dwarf reaches a critical mass, dictated by the mass and temperature of the white dwarf, it undergoes a thermonuclear runaway of the accreted material. During this explosive event, known as a nova eruption, the system brightens by many orders of magnitude, reaching absolute magnitudes of -10 in the optical. The time for the material to reaccumulate and the process to repeat is of order 10^4 years (Shara et al 2012; Yaron et al. 2005).

If the WD in a CV has a strong magnetic field ($\gtrsim 10^7$ Gauss), material leaving the L_1 point is channeled directly onto the magnetic poles of the WD. These systems are known as polars or AM Her stars (after the proto-type of the class; Cropper 1990). As there is no accretion disk in these systems they do not exhibit dwarf nova outbursts. However, since material still accumulates on the WD, they do undergo nova eruptions once the critical envelope mass has been reached.

Finally, if the WD has a magnetic field of intermediate strength (10^6 to 10^7 Gauss), the system will contain a partial accretion disk. Material leaving the L_1 point is initially deposited into the outer disk and transferred inwards. However, the WD magnetic field truncates the inner disk at $R > R_{WD}$. At this point, material latches onto the field lines and is once again channeled onto the magnetic poles. These systems are called intermediate polars or DQ Her stars (again, after the proto-type; Patterson 1994). Like non-magnetic CVs, they can exhibit both dwarf nova outbursts and nova eruptions.

CVs exist in the field population of the galaxy, and the studies of Pretorius & Knigge (2012) and Pretorius et al. (2013) provide the best determination to date of the space density of these systems. Analytic calculations (Di Stefano & Rappaport 1994) predicted a greater number of CVs in globular clusters due to stellar interactions. A number of studies attempting to find this excess of CVs in GCs using various techniques have yet to establish a significantly enhanced abundance of CVs. A recent study using simulations (Belloni et al. 2016) suggests that the actual number of CVs today in GCs may not be significantly enhanced.

The ultraviolet, specifically the far-ultraviolet (< 1800Å), may be the best way of detecting CVs. While a majority of stars in a GC are extremely faint in the FUV, as most of the flux is coming out in the optical, CVs will still have significant flux in the FUV. The FUV flux in a non-magnetic CV comes from a combination of the white dwarf, accretion disk, and the impact point of the material onto the accretion disk. In magnetic CVs, the FUV flux comes from the stream and accretion curtains that follow the magnetic field to magnetic poles of the WD. In this thesis, I have attempted to discover the CV

population by their inherent variability and FUV fluxes in the globular clusters NGC 1851 and NGC 6681.

1.2.3 Low-mass X-ray Binaries

Low-mass X-ray binaries (LMXBs) are composed of a neutron star (or black hole) and generally a main sequence star (a small subset of LMXBs have a white dwarf companion, as discussed below). As in CVs, the companion star is filling its Roche lobe, and material is being transferred to the neutron star via an accretion disk (Figure 1.8). Neutron stars are often magnetic, so the accretion disk may be truncated, as in intermediate polars.

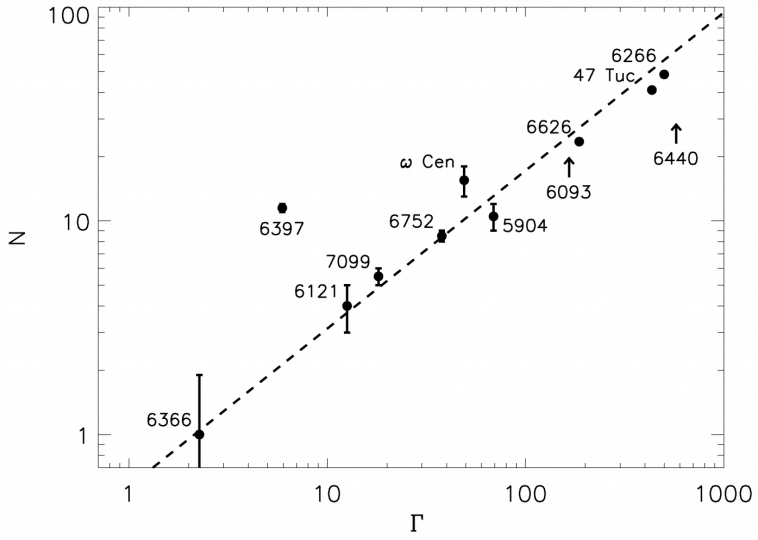

FIGURE 1.9: The Number of globular cluster X-ray sources (N) with $L_x \gtrsim 4 \times 10^{30}$ ergs s^{-1} versus the normalized encounter rate Γ of the cluster (Pooley et al 2003).

The flux from LMXBs has three sources: (1) the main-sequence companion, which emits primarily in the optical band, (2) the accretion disk, and, (3) the impact regions on the neutron star. The flux from the accretion disk and impact regions is mostly in the X-rays though may extend to longer wavelengths such as the ultraviolet. The identification of x-ray sources in the ultraviolet provides a secure method of identifying the optical counterparts.

A subclass of LMXBs have a white dwarf companion rather than a main sequence star. These systems are are known as ultracompact X-ray binaries. In these cases, a white dwarf is filling its Roche lobe, which is only possible for extremely small binary separations (corresponding to orbital periods of < 100 minutes). There are about ~ 17 UCXBs known to date in the Milky Way (Cartwright et al. 2013), and 5 of them are in globular clusters. In fact, one of these systems is in NGC 1851 and has a period of ~ 16.8 minutes (Zurek et al 2009). While this is certainly small number statistics, it is suggestive of an enhancement of such systems in globular clusters.

LMXBs in general seem to be enhanced in GCs over what would be expected from stellar and binary evolution (Katz 1975). More recently, Pooley et al (2003) found that there is a correlation between the collision rate (defined as $\Gamma \propto \rho_0^{1.5} r_c^2$ where ρ_0 is the stellar density and r_c is the core radius) and the number of LMXBs in globular clusters (Figure 1.9). The higher incidence of LMXBs in globular clusters and the correlation with collision rate suggests that the stellar dynamics in a GC enhances the likelihood of creating LMXBs.

1.2.4 Millisecond Pulsars

Millisecond pulsars (MSPs) are, as their name suggests, magnetic neutron stars (pulsars) with rotation periods of a few $\times 10^{-3}$ seconds (Lyne 1998). Pulsars spin down from when they are first formed, and thus the spin periods of MSPs are too fast for a clearly old population. This means that the MSPs must have been spun up.

A likely mechanism is a transfer of angular momentum through mass exchange (Urpin et al. 1998). The likely candidate for this spin up is the mass accretion in an LMXB. At some point accretion must stop or be significantly reduced, as generally MSPs are not detected in LMXBs. The link between LMXBs and MSPs has been observationally confirmed with the discovery of "transitional" MSPs that switch between the two states (Archibald et al 2009).

A high fraction of MSPs are in binaries, and it is the companion properties that have allowed some optical counterparts to be identified (e.g. Edmonds et al. 2002). For MSPs in GCs, it is quite possible that the binary that the MSP is in today is not the binary that spun it up, but rather it is a system that the MSP has been exchanged into through dynamical interactions.

In the two clusters studied in this thesis, there is only one known MSP, J0514-4002A, which is in NGC 1851. The companion to this MSP is estimated to have a mass $> 0.96 M_\odot$ (Freire et al. 2007). It is, therefore, quite possible that the companion is in fact a blue straggler. If this is true, the observations analyzed in this thesis may be able to identify this source.

1.2.5 Helium White Dwarfs

One of the possible consequences of binary evolution is the stripping of the outer envelopes of a star, as it evolves from the main sequence onto the sub giant branch and red giant branch. It is thought that this occurs because, as the more massive star evolves, it expands to engulf its lower mass companion. This leads to a so-called common-envelope phase, in which the companion orbits within the envelope of the more massive star. During this phase, the companion loses orbital energy and spirals towards the primary,

while the envelope gains orbital energy and is fully or partly ejected. The physics of common envelope evolution involves a huge range of size and time-scales and remains poorly understood (Iaconi et al. 2017).

One of the things we do know is that something like the above must occur. There have been a number of detections of objects that are best explained with a low mass ($< 0.3 M_{\odot}$) helium white dwarf (Cool et al. 1998). However, to produce a helium white dwarf through normal stellar evolution would take much longer than the age of any globular cluster (i.e. > 13 Gyr). This means that some process is occurring to higher mass stars that causes them to lose their outer envelopes and prevents the ignition of helium. It is believed that this process is common envelope evolution.

In a globular cluster, helium WDs may be found as isolated objects or as companions to other stars, such as blue stragglers. If a helium WD is in a binary, with a blue straggler for example, observations will show a blue or ultraviolet excess from the hot helium WD. These sources will be identifiable with the observations used in this thesis.

1.2.6 Double White Dwarfs

Double white dwarfs (DWD) are an important type of binary specifically because they may be the progenitors of supernovae type Ia and/or gravitational wave sources (Wang & Han 2012). DWDs are binaries composed of two white dwarfs where the white dwarfs are composed of either carbon-oxygen (CO) or helium (He) (Figure 1.10).

The known DWDs in the field that are composed of two CO white dwarfs appear to have periods that would not coalesce in a Hubble time ($\sim$ 13 Gyr), and thus the so-called "smoking gun" (or rather the 'loaded gun') for producing Type Ia supernovae via this channel remains to be found (Rebassa-Mansergas et al. 2017). It is possible that such systems are created or enhanced in globular clusters through dynamical interactions. Theoretical studies such as Shara & Hurley (2002) suggest that the number of DWD systems in a globular cluster may be enhanced over the field.

There are also about 40 DWDs in the field in which a CO WD is accreting from a low-mass helium WD via Roche-lobe overflow (Solheim 2010). These systems are known as AM CVns, after the prototype. Their orbital periods range from $\sim$ 5 minutes to $\sim$ 70 minutes. These systems are similar to cataclysmic variables in that material from the He WD is transferring to the CO WD through Roche lobe overflow (Figure 1.8) onto an accretion disk and subsequently onto the CO WD's surface. It is thought that once sufficient helium has accumulated on the CO white dwarf's surface, the helium may ignite in an eruption akin to a nova, though with helium rather than hydrogen undergoing thermo-nuclear runaway. This "nova" eruption may cause a compression of the CO white dwarf and possibly a subsequent explosion as a supernova Ia (Wang & Han 2012). These helium "nova" eruptions may have been detected already and may explain

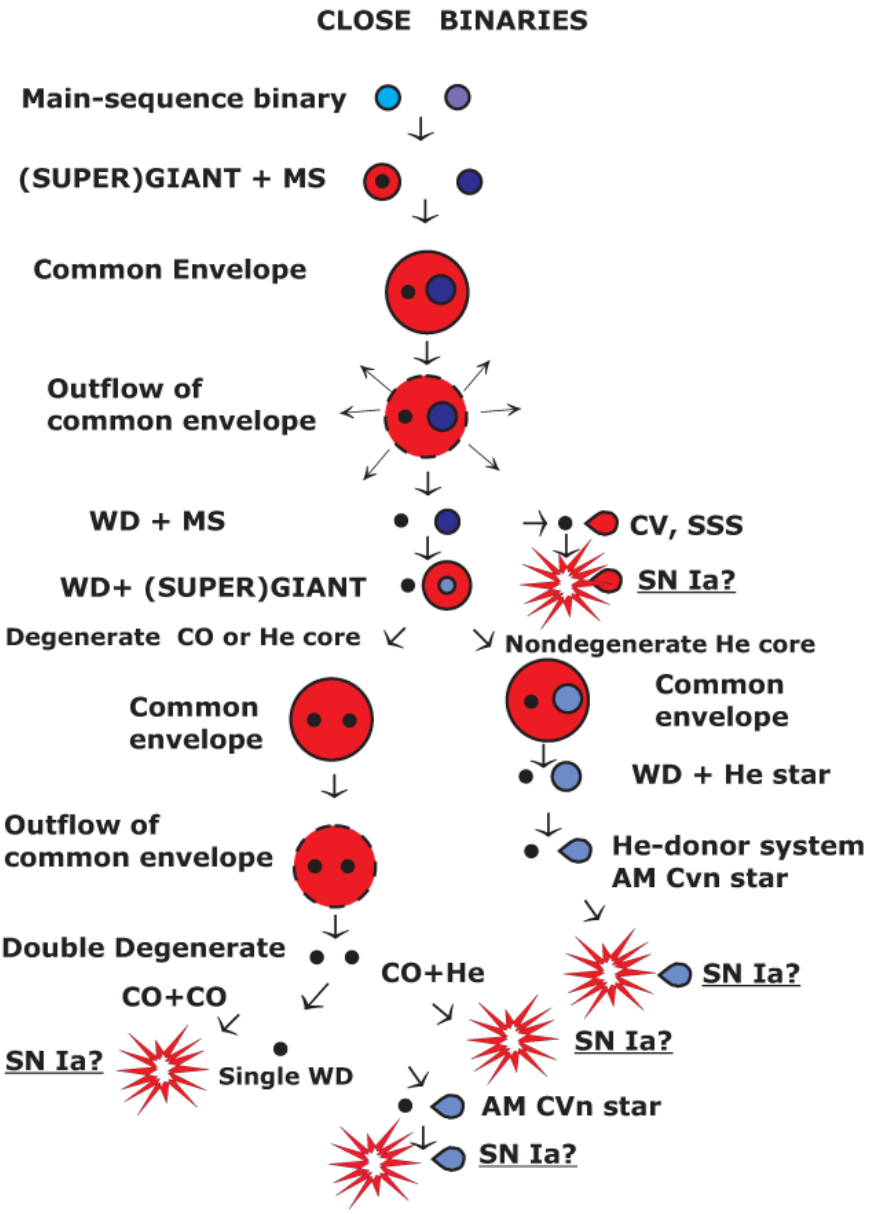

FIGURE 1.10: The evolutionary path of close Binary Evolution with the end products of double white dwarfs and possibly supernova Ia. This chart taken from Solheim (2010) represents the accepted scenario of close binary evolution, however, some of the stages of evolution (e.g. common envelope) are poorly understood.

a new type of transient named supernova .Ia (note the ".") because their appearance is that of a much less luminous supernova Ia (Brooks et al. 2015, Bildsten et al. 2007).

DDs in globular clusters, if they exist, will be very faint in the optical, and only the very deepest observations may photometrically detect these systems (e.g. Kalirai et al. 2012). Active (i.e. accreting) DDs, such as AM CVn, may be visible in the ultraviolet because of the accretion disk and the heating of the white dwarf. These systems will still be very faint in the optical, making the ultraviolet the ideal wavelengths to discover

them. In Chapter 7, we present the possible discovery of the first AM CVn in a globular cluster.

1.2.7 Symbiotic Binaries

Symbiotic binaries are another class of systems in which a compact object (white dwarf, neutron star or black hole) is accreting material through an accretion disk. Two aspects of these systems differentiate them from systems like CVs and LMXBs; (1) the companion is an evolved giant (i.e. red giant or asymptotic giant) star, and (2) the accretion disk is wind-fed, rather than fed via Roche lobe overflow.

The population density of symbiotic binaries (Magrini et al. 2003) would suggest that there should be $\sim 1 \pm 1$ symbiotic binary in the average GC. Yet no symbiotic binaries have been discovered so far in any GC. This may imply that these systems do not exist in GCs, perhaps because their separations are too large (> 1 AU) for them to survive interactions with other cluster members. This might reduce the expected number of symbiotic binaries to $<< 1$ per GC.

One of the best methods for discovering symbiotic stars would be to observe an ultraviolet excess of in evolved star, indicating a possible hot white dwarf and accretion disk. Confirmation of a candidate as a symbiotic binary would require the detection of emission lines in the optical, such as oxygen, helium or hydrogen lines. One of the possible interpretations for the object discussed in Chapter 7 is a symbiotic binary.

1.2.8 Extreme Horizontal Branch

There are a number of hot horizontal branch stars in globular clusters which have, apparently, lost more mass on the red giant branch than the majority of the other horizontal branch stars. These systems have field analogs known as subdwarf O (sdO) and B (sdB) stars (Brown et al. 2010). Observations of the field population indicate that there is a very high fraction of binaries among the field sdO and sdB stars; in fact, this binary fraction is consistent with 100% (Copperwheat et al. 2011). In contrast, studies of these systems in globular clusters have found very few are in binaries (Moni Bidin et al. 2009).

One explanation for this discrepancy is that some extreme HB stars in GCs were in a binary that was subsequently broken apart through dynamical interactions. However, in this case we would still expect that a significant fraction of extreme HBs would remain in binaries today. If this is the case, then monitoring these stars for variability and looking for excesses in the spectral energy distribution (e.g. an excess of red flux) may be the best methods of determining possible binarity efficiently. The data used in this thesis may be able to shed some light on this.

1.2.9 Sub-Subgiant Stars

A relatively new class of peculiar systems detected in stellar clusters is known as sub-sub-giants. These are defined as stars that appear in a cluster's colour-magnitude diagram at the same colour as the red giant branch, but are fainter than the subgiant branch (Figure 1.11). For an overview of the known systems and their properties, see Geller et al (2017).

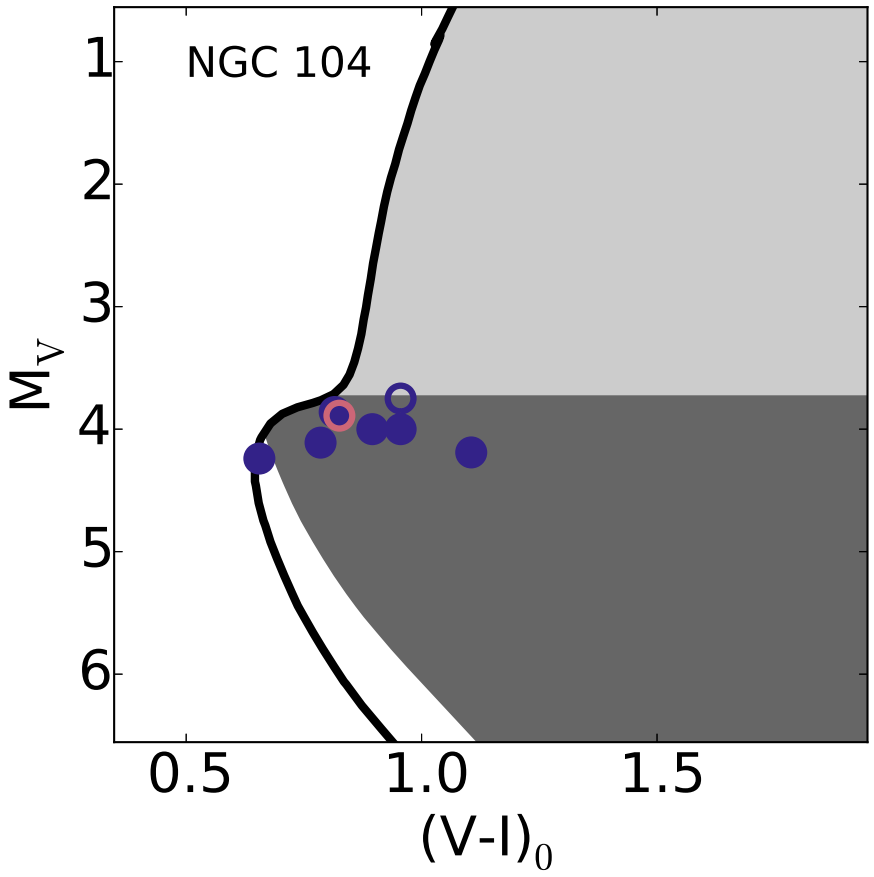

FIGURE 1.11: The solid line represents the stellar sequence for NGC 104 (47 Tucanae). If a stars photometry places it in the dark gray region it is classified as a sub-sub-giant. If a stars photometry places in in the light gray region it is classified as a red straggler. The circles are candidate sub-sub-giant stars in NGC 104. (From Geller et al. 2017)

These systems may exist in the field. However, as for blue stragglers, the identification of these stars as something other than a normal sub-giant or red giant branch star is difficult, since there is no single-age and single-metallicity stellar sequence against which they can be compared.

Very little is known about these systems, and their properties and formation mechanisms are poorly understood. There are relatively few, ~ 65, systems known throughout all stellar clusters (both open and globular). Thus the discovery of additional members of

this class is essential if we hope to understand them. Some of the objects discussed in Chapter 4 may belong to this new population.

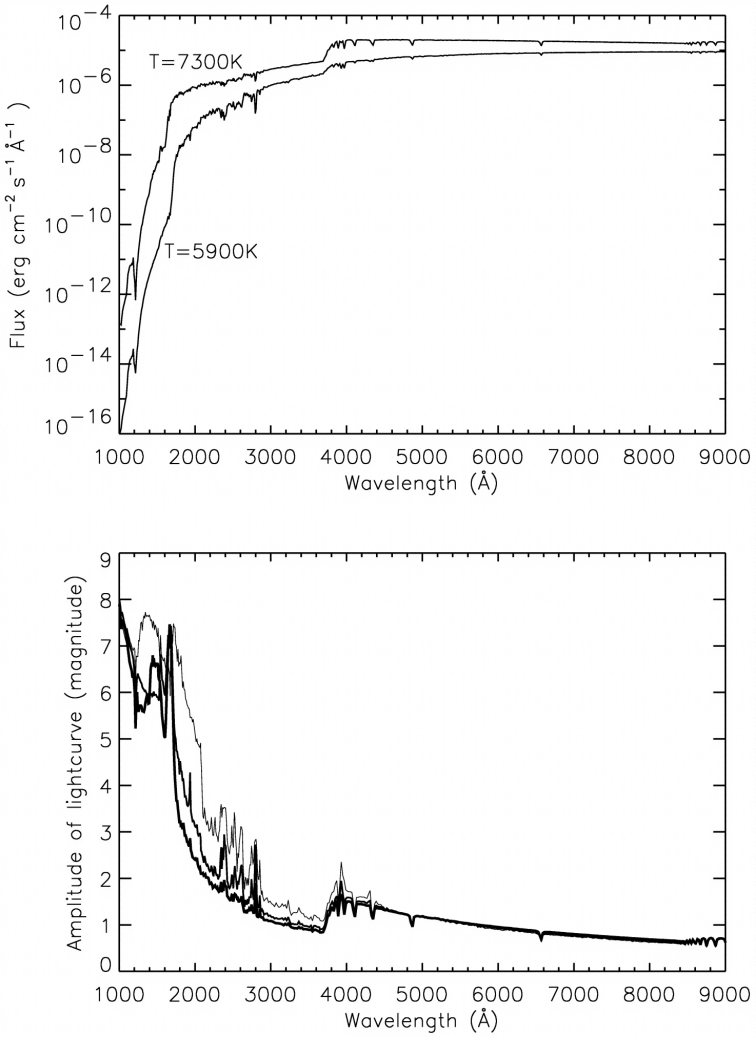

FIGURE 1.12: Top panel: Model spectra at maximum light (7300 K) and minimum light (5900 K) for a RR Lyrae with [Fe/H]=-1.25. Bottom panel: Predicted difference between maximum and minimum brightness. The maximum difference is at wavelengths shortward of 2000 Å. Wheatley et al (2005)

1.2.10 RR Lyrae

RR Lyraes are pulsational variables on the horizontal branch. The region of the colour magnitude diagram they occupy is known as the instability strip. The instability strip extends from higher-mass Cepheid variables to the lower-mass main sequence δ Scuti variables. The study of RR Lyraes is a field of research that is relevant particularly in older populations, such as globular clusters, and the periods of the pulsations are known to correlate with the star's mean luminosity in what is known as the period-luminosity relation. The period-luminosity relation for RR Lyraes (actually each type

of pulsational variable has a period-luminosity relation) has been used to determine distances to globular clusters and local group galaxies.

The driving mechanism for pulsating variables like RR Lyraes is known as the κ-mechanism (Baker & Kippenhahn 1962). A compressed layer of a star's atmosphere becomes fully ionized (i.e. $He^{+} \rightarrow He^{++}$) increasing the opacity (κ) absorbing more energy and increasing in temperature. The increase in temperature results in an increase in pressure and the increase in pressure forces the layer to expand outwards. As the layer expands the pressure and temperature decrease allowing the layer to become partially ionized (i.e. $He^{++} \rightarrow He^{+}$) with a corresponding decrease in opacity (κ) allowing more energy to pass through. The layer, now no longer retaining heat because of the decrease in opacity (κ), contracts toward the stellar core (i.e. where the process started). This whole process continues until the star evolves and the atmosphere is able to maintain stability (or the process is unobservable).

Wheatley et al (2005) found that RR Lyraes brighten by as much as a factor of 1000 in the GALEX FUV ($\sim 1400 \rightarrow 1800$ Å) which is similar to the wavelength coverage of the ACS/SBC filter, F140LP, used in this thesis. As can be seen in Figure 1.12, taken from Wheatley et al (2005), the greatest change in flux is at wavelengths < 2000 Åas the star's effective temperature changes with pulsations cycled from ~ 5900 K to ~ 7200 K. This is highlighted by the bottom panel of Figure 1.12 which is the difference between the SEDs at minimum and maximum brightness.

1.3 Previous Far-ultraviolet Studies of Globular Clusters

The study of hot populations in GCs, such as CVs, has benefited significantly from the far-ultraviolet capabilities and spatial resolution of the Hubble Space Telescope, especially in combination with its upgraded, "solar-blind" UV instruments/detectors, i.e. the Space Telescope Imaging Spectrograph (using the FUV-MAMAor NUV-MAMA) and the Advanced Camera for Surveys (using the Solar Blind Channel). The first dedicated far-UV imaging study of a GC with one of these instruments was carried out by Knigge et al. (2002) on NGC 104 (GO-8219 PI: Knigge). This resulted in the identification of hot white dwarfs, blue straggler stars, and, candidate cataclysmic variables (Knigge et al. 2002). The observations were carried out using the FUV-MAMA on the Space Telescope Imaging Spectrograph to perform a combination of imaging with the F25QTZ filter and slitless spectroscopy with the G140L grating. Knigge et al (2003) identified the previously puzzling object AKO9 as a long-period (1.1 days) cataclysmic variable. This was the first spectroscopically confirmed CV in NGC 104. Knigge et al. (2008) spectroscopically confirmed two additional CVs, V1 and V2, and detected variability of 3 CVs (AKO9, V1, and V2) and 3 blue stragglers.

The Knigge et al. (2002) study was the basis for a number of studies of globular clusters: NGC 2808 (Dieball et al. 2005), NGC 6093 (Dieball et al. 2010; Thomson et al. 2010), NGC 6397 (Dieball et al. 2017; Shara et al. 2005), NGC 6752 (Thomson et al. 2012), and NGC 7078 (Dieball et al. 2007). A summary of the findings for each of these clusters is as follows:

- **NGC 2808** Dieball et al. (2005) identified based on their location in the far-ultraviolet CMD $\sim$ 40 white dwarfs, $\sim$ 60 blue stragglers, and $\sim$ 60 cataclysmic variable candidates. They found 28 variable candidates based on an excess sigma from the mean sigma for sources of similar magnitude. There is insufficient temporal coverage to determine periods, though six of these candidates are clearly variable when the individual images are inspected, and, one is identified as an RR Lyrae (V22; Corwin et al. 2004).

- **NGC 6093** Dieball et al. (2010) identified $\sim$ 117 blue and extreme horizontal branch stars, $\sim$ 75 blue stragglers, $\sim$ 32 white dwarfs, and $\sim$ 59 main sequence-white dwarf candidates (or cataclysmic variable candidates). Dieball et al. (2010) also identified six far-ultraviolet counterparts to the X-ray sources found by Heinke et al. (2003). One of these sources, CX01, is identified with the nova T Sco. Thomson et al. (2010) identified three variables, two RR Lyraes and one SX Phoenicis with a $\sim$ 55.4 min period. No variation was detected for the known variables T Sco and the dwarf nova DN1 (Shara & Drissen 1995) implying that the amplitude of variation is too small and/or the temporal coverage is insufficient.

- **NGC 6397** Shara et al. (2005) found that two of the cataclysmic variable candidates of Grindlay et al. (2001) appear to have variations between epochs that are consistent with these sources being dwarf novae. Dieball et al. (2017) carried out a more thorough analysis of the far-ultraviolet data and identified three likely blue horizontal branch stars, eleven blue stragglers, and 16 white dwarf and/or white dwarf binaries. There were too few (4) FUV exposures to determine variability, however, Dieball et al. (2017) looked at the larger NUV data set and found that there appeared to be variations of $\sim 0.1 - 0.5$ mag among the five CVs within the field-of-view. They suggested that this variability may be an indication of the flickering that is often observed in CVs.

- **NGC 6752** Thomson et al. (2012) identified numerous horizontal branch stars, blue stragglers and white dwarfs, as well as 87 sources populating the region between the white dwarf sequence and main sequence in the CMD. Only a fraction of these sources were identified in the FUV as the field-of-view is significantly smaller ($\sim 36\times$) than that of the WFC3. Thomson et al. (2012) also conducted a search for variability and have found a number of sources with apparent variability. However, the data used has insufficient temporal coverage to indicate if the variability found is periodic.

- **NGC 7078** Dieball et al (2005) identified a FUV counterpart to the low-mass X-ray binary M15 X-2. In addition, they clearly detected a period of 22.58 minutes, which places this source among the ultra compact X-ray binaries. Dieball et al. (2007) found 41 sources that show signs of variability. These variables have been classified as 17 RR Lyraes, 6 CV candidates, 2 SX Phoenicis stars or candidates, 7 Cepheids or candidates, 1 low-mass X-ray binary (AC 211), and 8 suspected but as yet unclassified variables.

A number of studies (see shown above) have indicated the discovery of a number of likely variables, however, other than the Knigge et al. (2003) study of the object AKO9 in NGC 104 and Dieball et al. (2007) study of NGC 7078, these studies lack the temporal coverage to determine if the detected variability is periodic. The work presented for NGC 1851 in this thesis is qualitatively similar to that of Dieball et al. (2007).

Chapter 2

The Globular Clusters NGC 1851 & NGC 6681

The centers of globular clusters (GCs) are very crowded regions with 10^4 to 10^5 stars within the central few arcminutes. The point spread function wings of the brightest stars, such as red giants, increase the background and reduce the area which fainter sources can be detected. In the far ultraviolet, the brightest optical sources (e.g. red giants) are among the faintest detected sources, if they are detected at all. This increases the ability to identify compact binaries (e.g. cataclysmic variables, low mass X-ray binaries), hot white dwarfs, blue horizontal branch stars, and, blue straggler stars, as these sources are ultraviolet bright, even if they are optically faint.

A number of factors determine what is a suitable GC to observe in the far-ultraviolet. One of the constraints is the reddening or E(B-V). For every magnitude of reddening (i.e. E(B-V) = 1.0) in the far-ultraviolet is extincted by $\sim$ 7 magnitudes. Another consideration is the distance to the globular cluster. While many of the objects of interest emit a large fraction of their light in the ultraviolet, they are also intrinsically faint. Some examples of such sources are low mass X-ray binaries, cataclysmic variables, and AM CVn systems. The actual brightness in the ultraviolet of these sources is more dependent on the accretion rate and the accretion disk than on the donor stars. For example, in a cataclysmic variable, the secondary star, usually a low-mass main sequence star, effectively contributes no flux in the ultraviolet. The luminosity of the white dwarf in the system is determined by its radius and temperature. A white dwarf experiencing no accretion quickly cools, making it hard to detect, because $L \propto T^4$ (where L is luminosity and T is temperature). However, accretion in cataclysmic variables heats the white dwarf so that $L_{WD} \approx 0.2\dot{M}M_{WD}/R_{WD}$ (e.g. Townsley & Bildsten 2003, Sion 1995) Thus, the white dwarf luminosity is dictated by the accretion rate. The combination of a hotter white dwarf and its surrounding accretion disk make these sources observable in the ultraviolet. A low mass X-ray binary's flux in the ultraviolet

is nearly all from the accretion as the neutron star has a very small radius, which means that it contributes very little to the ultraviolet luminosity. Often, the ultraviolet, optical, and infrared emission in LMXBs is produced when X-rays heat the outer accretion disk.

Another consideration is the field of view of the available instruments. The two main far-ultraviolet cameras on the Hubble Space Telescope are the Advanced Camera for Surveys / Solar Blind Channel (ACS/SBC) and the Space Telescope Imaging Spectrograph / Far Ultraviolet Multi Anode Multiple Array (STIS/FUV-MAMA). In both cases, the field of view is about 25" $\times$ 25". The center of a globular cluster is where I expect to find a large fraction of the objects of interest, because they are formed there through interactions with other stars and binaries. Given time, many of these objects will also settle to the core through mass segregation as they are among the more massive objects in the globular cluster (but see Lugger et al 2017, Cohn et al. 2010).

Name	**NGC 1851**	**NGC 6681**
Other Name		M70
RA (J2000)	05:14:06.76	18:43:12.76
DEC (J2000)	-40:02:47.6	-32:17:31.6
R_{SUN} **(kpc)**	12.1	9.0
R_{GC} **(kpc)**	16.6	2.2
[Fe/H]	-1.18	-1.62
E(B-V)	0.02	0.07
$(m - M)_V$	15.47	14.99
$M_{V,t}$	-8.33	-7.12
c	1.86	2.50 c
r_c **(")**	5.4	1.8
r_h **(")**	30.6	42.6
μV **(Vmag/"^{2})**	14.25	14.25
$\rho_\odot$ **(log$L_\odot$/pc^3)**	5.09	5.82
t_c **(log(yrs))**	7.43	5.82

TABLE 2.1: The Basic Information for each cluster (Harris 1996). The variables in the right hand column have the following definitions: R_{SUN} - distance from the sun in kpc, R_{GC} - distance from the Galactic center, [Fe/H] - metallicity, E(B-V) - foreground reddening, $(m - M)_V$ - distance modulus in the visual, $M_{V,t}$ - Cluster absolute visual magnitude, c - central concentration ($c = log(r_t/r_c)$ core-collapse is denoted with a c), r_c - core radius, r_h - half-light radius, μV - central surface brightness, $\rho_\odot$ - central luminosity density, t_c - core relaxation time.

2.1 Why NGC 1851?

Given the importance of both reddening and distance, how does NGC 1851 compare as a choice for far-ultraviolet observations? In Table 2.1, we see that its reddening is small, $E(B - V) = 0.02$, but its distance, 12.1 kpc, is larger than the median distance, ~ 9 kpc, of globular clusters. The core radius is 5.4" which lies well within the field of view of both ACS/SBC and STIS/FUV-MAMA.

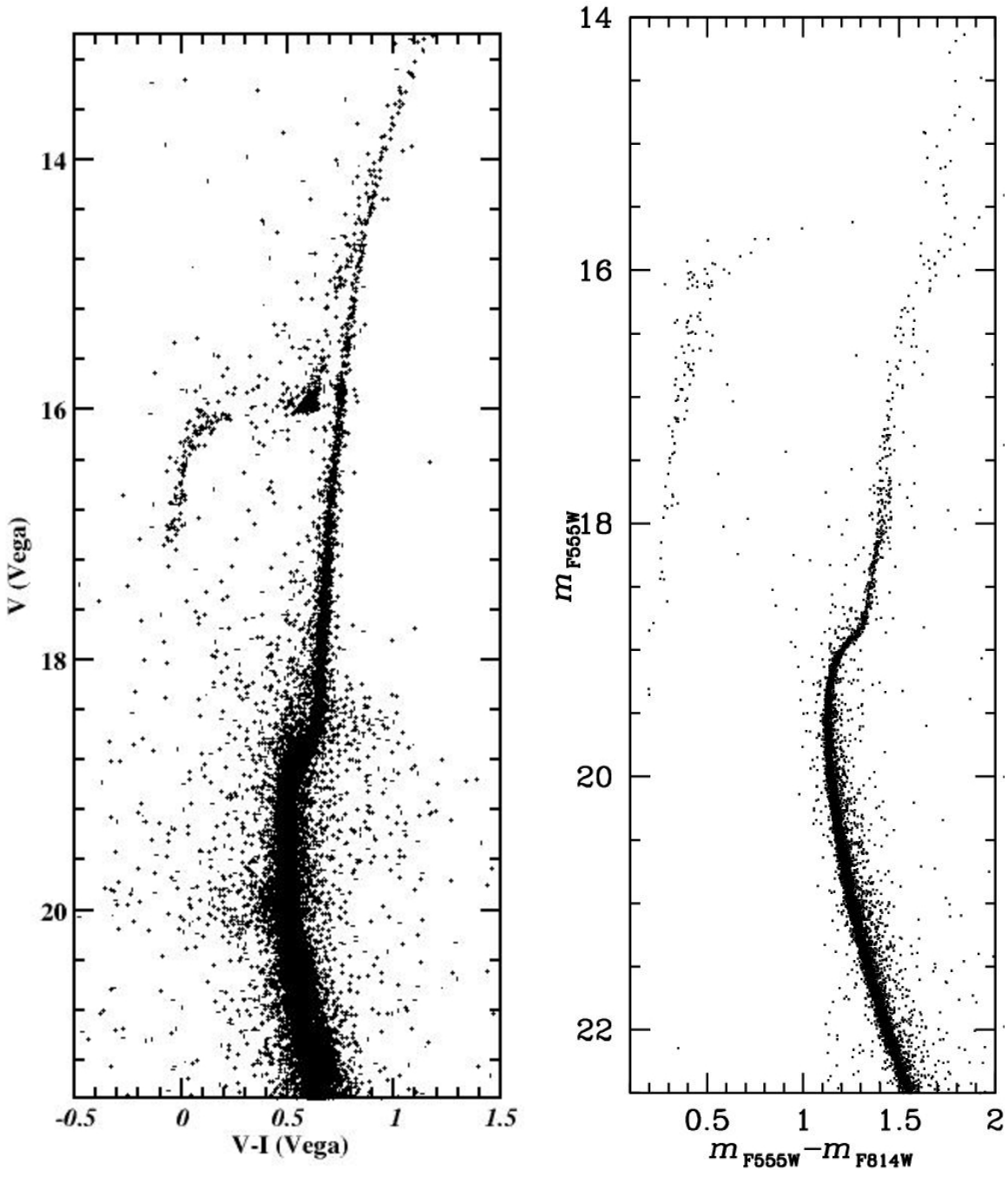

FIGURE 2.1: The colour magnitude diagrams for NGC 1851 (Milone et al 2008) on the left and NGC 6681 (Massari et al 2016) on the right. Both photometric datasets are from images taken with ACS/WFC on Hubble Space Telescope.

While the reddening and core radius are suitable for a far-ultraviolet study, more than half the Galactic globular clusters have smaller distances than NGC 1851. In fact, the nearest globular cluster has a distance 2.2 kpc. So why was this globular cluster chosen for a far-ultraviolet study?

NGC 1851 was originally observed in the FUV in order to determine the orbital period of a known X-ray binary (4U 0513-40). This program consists of a time-tag STIS/FUV

dataset available in the STScI archive (MAST - Mikulski Archive for Space Telescopes) with the proposal number 7363 and principal investigator Dr. Bruce Margon. The data span 4 orbits of Hubble Space Telescope time or a total of 11,000 seconds of on-source time for the purpose of determining the period of the ultracompact X-ray binary (4U 0513-40). While these data lacked the signal-to-noise to determine the period of 4U 0513-40 unambiguously, I subsequently examined the full dataset and found a significant number of other sources varying. However, the amount of data was insufficient to determine periods or otherwise characterize these variables. I therefore decided that a follow-up proposal was needed to better understand these sources.

The proposal I led (GO-10184) asked to replicate the observations of proposal 7363, but extending it to 12 orbits, split into 3 visits of 4 orbits each. Shortly after being granted time, the power supply on STIS failed, and my proposal was transfered to the ACS/SBC. The ACS/SBC does not have a timetag mode so discrete exposures were required. I decided on exposure durations of 90 seconds which gave me a total of 273 exposures over the 12 orbits. These observations are discussed in depth in Chapter 3.

2.1.1 The Peculiar Horizontal Branch

NGC 1851 is anything but a "normal" globular cluster. It has been recognized as odd for well over 30 years. The first thing that is apparent when looking at NGC 1851's optical colour magnitude diagram is that the horizontal branch has two distinct concentrations of stars (Figure 2.1). NGC 1851 is one of just a handful of globular clusters which demonstrate this distinct horizontal branch morphology.

The implication of this feature is that mass loss on the red giant branch must have taken place in a bimodal fashion, with one group of stars experiencing strong mass loss, and the other weak mass loss. Ideas about what could be causing the additional (or reduced - depending on what is interpreted as normal) mass loss are varied and follow the proposed explanations for the second parameter problem (as mentioned in Chapter 1). Age and abundance variations have historically been among the most promising explanations.

In the end, it turns out that with precision imaging and photometry from Hubble Space Telescope, using the Advanced Camera for Surveys / Wide Field Channel (ACS/WFC), a solution may have been found. These observations show two distinct sub-giant branches (Figure 1.3). To explain this, it turns out that age and abundance variations must both be present. The best interpretation for NGC 1851 is then that there were two distinct epochs of star formation, separated by 100-300 million years, with an increase in the Helium and/or C+N+O abundance in the second generation (D'Antona et al. 2016). The age gap and increase in Helium abundance seems to explain the multiple populations discovered. It is then natural to suggest that these two populations also map to the bi-modal distribution of the horizontal branch.

2.1.2 Ultra-compact X-ray Binary

NGC 1851 is also in a very small club as one of 5 (Cartwright et al. 2013) globular clusters which host an ultracompact X-ray binary. There are a total of 17 ultra-compact X-ray binaries in the Galaxy (Cartwright et al. 2013) and, while that is admittedly small number statistics, about a third of them are in globular clusters.

Luminous low-mass X-ray binaries are definitely more populous in globular clusters (Kundu et al. 2003) by about a factor of a thousand per unit stellar mass. The same would also appear to be true for ultracompact binaries (with the small number caveat mentioned above).

In my initial examination of the far-ultraviolet data, I determined the period of the object 4U 0513-40 to be 16.8 minutes and confirmed its ultracompact nature. The discovery of another ultracompact binary than became a goal of this work, and the subsequent discovery of FUV1 (Chapter 7) demonstrates that additional ultracompact binaries are indeed present in this cluster.

2.1.3 Blue Stragglers

In every cluster, globular or open, there exist stars which have the appearance of being younger than the age of the cluster itself. These stars are known as blue stragglers, and they lie on or near the main sequence, but at a luminosity greater than the luminosity of main sequence turnoff stars (see Chapter 1). Recently, Ferraro et al (2009) have apparently discovered, at least in one cluster, that the blue stragglers are distributed along two sequences. NGC 1851 does not have multiple sequences of blue stragglers in the optical (Saviane et al 1998).

When bluer colours are chosen a greater number of sources populate the region identified as blue stragglers. This may indicate that the selection of blue stragglers may depend on the wavelengths of the filters chosen. A possible explanation for this effect is that some of these systems harbour hot companions. A small hot companion would not contribute much to the spectral energy distribution in the mid-optical and beyond, but it might contribute significantly in bluer bands. The implication of a hot companion is that, depending on the total numbers, stripping of stars to expose the Helium core must occur relatively frequently. One of the formation scenarios of blue straggler stars is mass transfer in a binary of the outer envelope of one of the stars onto the other. This results in one of the stars in the binary having more mass (the blue straggler star) and the other would be the remaining hot stellar core. I present the total number of such systems found in Chapter 4.

2.1.4 Helium Stars - Horizontal Branch and White Dwarfs

When stars undergo a significant amount of mass loss, they either end up as Helium white dwarfs or on the extreme hot end of the horizontal branch. The main difference is a combination of when the mass loss occurred and if Helium is ignited. If Helium is ignited, the star will end up on the horizontal branch; if Helium fails to ignite, the star will end up on the Helium white dwarf cooling sequence. Helium white dwarf have yet to be identified in NGC 1851 though candidate Helium white dwarfs have been identified in the GC NGC 6397 (Cool et al 1998).

"Normal" mass loss is still poorly understood, in the sense that a full understanding of what contributes to mass loss is highly uncertain. For instance, the mass loss on the red giant branch may be affected by the abundance of various elements such as Helium, Oxygen, etc., though only weak evidence seems to be available (see Chapter 1).

Regardless, the production of a Helium white dwarf cannot be produced through "normal" (single star) stellar evolution and requires some additional mechanism for the star to lose its entire outer envelope. This is required to ensure that the pressure on the core remains insufficient to ignite Helium, i.e. to prevent a Helium flash. The leading mechanism seems to be mass transfer in a close binary and/or perhaps a number of interactions stripping material from the star.

2.2 Why NGC 6681?

NGC 6681 (Figure 2.2) is not a very well studied globular cluster, even though it is only 9 kpc away and has a low reddening $[E(B-V) = 0.07]$. In fact, a search using the Astrophysics Data System (ADS) revealed only eleven refereed papers. These eleven papers can be divided into four areas of research: (1) the search for variables (i.e. RR Lyraes) in the optical (Liller 1983; Kadia et al. 1996; Kadia et al. 1998), (2) the horizontal branch (Caloi et al. 1984; Watson et al. 1994; Brocato et al. 1996), (3) cluster structural parameters (Lugger et al. 1995; Han et al. 2017), and (4) proper motions (Massari et al. 2013; Bellini et al. 2014; Massari et al. 2016).

The core of NGC 6681 is very compact, and shows a core cusp, or core collapsed distribution of stars. This stellar density contributes to the calculations of Bahramian et al. (2013) showing that this GC has one of the highest interaction rates. This clusters parameters (see Table 2.1) would seem to make this cluster ideal for study, but other than the few studies identified above, it has largely been ignored.

The compactness of the core (Figure 2.2) and the plethora of blue horizontal branch stars (Figure 2.1) make this globular cluster ideal as a calibration target for the Hubble Space Telescope in the ultraviolet. The matching of the relatively bright horizontal branch

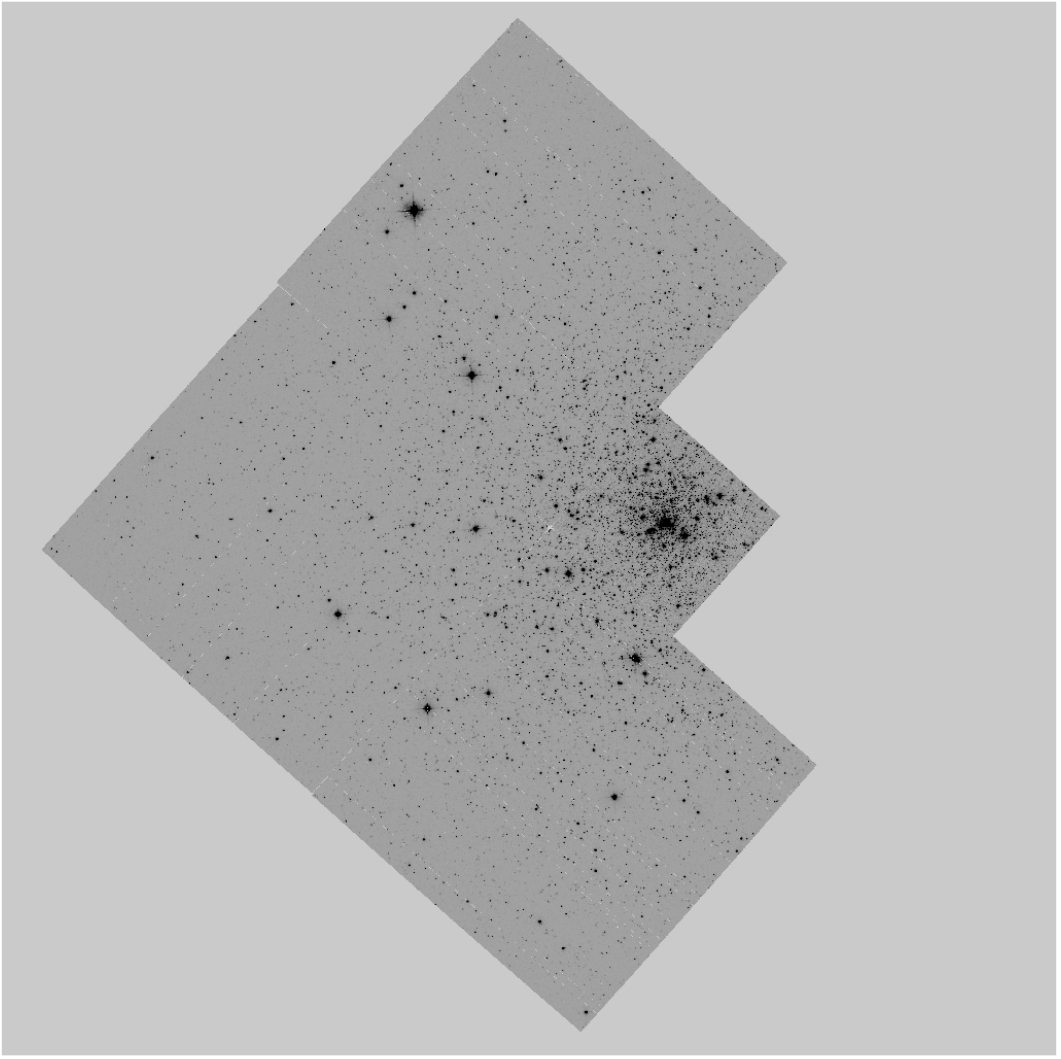

FIGURE 2.2: The center of NGC 6681 taken with WFPC2 on Hubble Space Telescope in the optical filter F555W (Watson et al. 1994). The image was obtained from the Mikulski Archive for Space Telescopes. North is towards the top and East to the left of the image.

stars between exposures allows one to calculate the transformation equations which will remove the geometric distortions in the ultraviolet detectors. Geometric distortions are present in all the cameras on the Hubble Space Telescope, because the area that each pixel covers on the sky varies as a function of the distance from the axis of the telescope. The on-axis camera WFC3 presently, WFPC2 in the past, has the least distortion, but still suffers from some. The rest of the cameras, ACS, STIS and NICMOS, are all off-axis cameras, and therefore have significant distortions. The distortion can be calculated empirically by determining the equation to transform the pixel positions from one frame to another.

NGC 6681 was chosen, by the instrument scientists, for calibration purposes to do exactly what is mentioned above. In addition, they monitored this globular cluster taking

exposures approximately every 4 to 6 months. This monitoring means that one can check for time dependent distortion changes. What this means for this thesis is that there are approximately 20 years of data and more than 80 epochs of imaging data for this globular cluster. The cluster with the next largest number of epochs is 47 Tucanae (NGC 104) at about 45 epochs, most of which are in the optical. This is thus a unique dataset that is ideal for a search for transients. This will put significant limits on the total numbers of transients, such as dwarf novae (see Chapter 6). In addition, NGC 6681 has also been imaged by every instrument that is capable of imaging in the ultraviolet and optical. Future studies of this globular cluster, such as an examination of the spectral energy distributions, will benefit from this large multi-wavelength dataset.

2.3 Final Thoughts

The clusters NGC 1851 and especially NGC 6681 have historically been understudied compared to other globular clusters such as NGC 7078 (M15) and NGC 104 (47 Tucanae) that have dominated photometric work. Recently, the survey of globular clusters by Ata Sarajedini (HST proposal GO10775), which imaged the core of about one third of the globular clusters in the Milky Way has led to the discovery of multiple populations. This put the spotlight on NGC 1851 as one of the first globular clusters with distinct multiple populations (Milone et al. 2008). A new result from spectroscopic analysis of stars in NGC 6681 suggests that two discrete populations exist (O'Malley et al 2017), however, two distinct sequences in the CMD have yet to be seen.

Bahramian et al. (2013) have calculated that these two clusters are among the ten clusters with the highest interaction rate. The correlation of the number of X-ray binaries specifically with interaction rate indicates that both NGC 1851 and NGC 6681 should have a population of X-ray binaries at least as large as what has been found in 47 Tucanae (NGC 104). If cataclysmic variables correlate with interaction rate in the same manner, I would expect to find a substantial population.

Chapter 3

Data Analysis of NGC 1851

All of the observations used in this thesis were obtained using the Hubble Space Telescope. I have made use of Chandra X-ray observations in Chapter 7. The analysis of the Chandra data was conducted by David Pooley, and I use his analysis in Chapter 7. I processed all of the Hubble Space Telescope data, including the ACS/WFC images of NGC 1851, for this thesis. The photometric catalogs for the ACS/WFC images, presented in Milone et al (2008), were provided by Ata Sarajedini.

3.1 Data Sets

The optical and ultraviolet observations used in this study are listed in Table 3.1 and were retrieved from the Mikulski Archive for Space Telescopes (MAST). During retrieval, the data were calibrated or recalibrated with the best available calibration files. This is known as "on-the-fly" calibration and is the standard practice in the analysis of HST observations.

In addition to the ultraviolet/optical Hubble Space Telescope imaging observations we also made some use of Chandra X-ray imaging and optical spectroscopy using the Hubble Space Telescope/ Space Telescope Imaging Spectrograph. These observations are utilized in Chapter 7 and explained in greater detail there.

In Figure 3.1, I present the central section of the F606W (see Table 3.1 for central wavelength and effective width of this filter) image of NGC 1851 taken with the Advanced Camera for Surveys/ Wide Field Channel. The red outline laid over the core of NGC 1851 represents the field of view of the Advanced Camera for Surveys/ Solar Blind Channel. Note that the dark starless stripe going from the top left to the bottom right in Figure 3.1 is the chip gap between the two Charged Couple Devices (CCDs) which compose the Wide Field Channel.

All of the exposures for each filter/camera were combined using the drizzlepac software (Gonzaga et al. 2012), which is a package of python codes that are used in the data reduction environment pyraf or as native python routines. Examples of these combined images can be seen in Figure 3.2 which also shows several circled sources which are common to all the images.

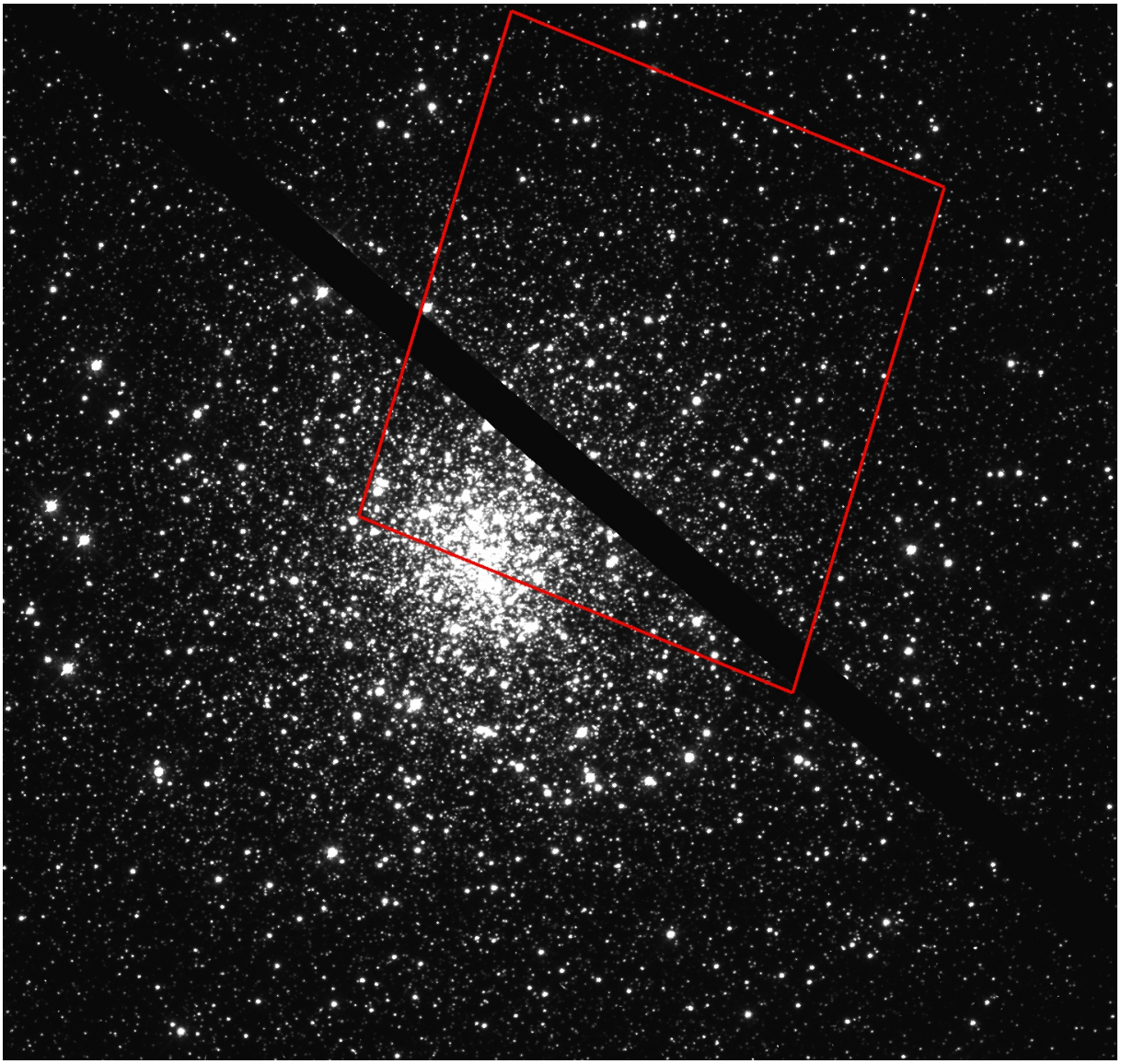

FIGURE 3.1: A F606W ACS/WFC image of the core of NGC 1851 with the red outline marking the field of view of our ACS/SBC data. The dark stripe (going from top left to lower right) is the chip gap between the two chips which make up the ACS/WFC. The image is North up and East left.

3.2 Catalog Construction

A catalog of the positions of all the stars in each combined image (the photometric catalog of Milone et al (2008) was used for the ACS/WFC images) was generated using

Proposal ID	Filter Name	Central Wavelength (Å)	Effective Width (Å)	Camera	Observation Date	Exposure Time (sec)	Number of Exposures
6095	F555W	5464.6	1228.4	WFPC2	1995-10-05	6	1
6095	F555W	5464.6	1228.4	WFPC2	1995-10-05	40	1
6095	F439W	4316.0	473.2	WFPC2	1995-10-05	40	1
6095	F439W	4316.0	473.2	WFPC2	1995-10-05	160	2
6095	F218W	2209.6	395.0	WFPC2	1995-10-05	600	1
6095	F218W	2209.6	395.0	WFPC2	1995-10-05	1000	1
5696	F439W	4316.0	473.2	WFPC2	1996-04-10	300	4
5696	F336W	3348.2	374.3	WFPC2	1996-04-10	900	4
11975	F555W	5464.6	1228.4	WFPC2	2009-05-02	1	1
11975	F555W	5464.6	1228.4	WFPC2	2009-05-02	40	1
11975	F555W	5464.6	1228.4	WFPC2	2009-05-02	50	2
11975	F336W	3348.2	374.3	WFPC2	2009-05-02	40	1
11975	F336W	3348.2	374.3	WFPC2	2009-05-02	800	3
11975	F255W	2604.9	395.1	WFPC2	2009-05-02	1200	2
11975	F255W	2604.9	385.1	WFPC2	2009-05-02	1300	1
11975	F170W	1786.3	545.1	WFPC2	2009-05-02	700	3
10775	F606W	5921.1	1502.4	ACS/WFC	2006-05-01	1770	1
10775	F814W	8057.0	1539.4	ACS/WFC	2006-05-01	1770	1
7363	F25QTZ	1596.2	231.6	STIS/FUV	1999-03-24	1300	2
7363	F25QTZ	1596.2	231.6	STIS/FUV	1999-03-24	1400	6
10184	F140LP	1528.0	253.4	ACS/SBC	2006-08-15	90	91
10184	F140LP	1528.0	253.4	ACS/SBC	2006-08-17	90	91
10184	F140LP	1528.0	253.4	ACS/SBC	2006-08-23	90	91

TABLE 3.1: The Hubble Space Telescope observations used in this thesis. The Central Wavelength and Effective Width are taken from the instrument handbooks for WFPC2 (McMaster & Biretta 2008), ACS (Avila et al. 2017), and, STIS (Riley et al. 2017). The rest of the information shown here is from the the Mikulski Archive for Space Telescopes (it is also in the image headers for each of the exposures).

DAOfind, which is one of the programs in the DAOphot package of programs written and distributed by P. Stetson (Stetson 1994). The DAOphot package allows the user to identify the stellar sources in an image and perform aperture and point spread function (PSF) photometry for the sources.

Photometry is the determination of the brightness of an object and placing that brightness onto a standard system. I have chosen to use the HST native system, known as STMagnitude (or STMag for short), where $m_{STMag} = -2.5\log(F_\lambda) - 21.1$ for a source with F_λ =constant. In an uncrowded field (i.e. objects PSF do not overlap) aperture photometry is normally sufficient for determining an object's brightness. In a crowded field, however, a more sophisticated technique is required to obtain precise photometry. This technique is known as point spread function fitting, or PSF photometry.

PSF photometry fits a three-dimensional model to each star on the image. The three dimensions of a star are its X and Y pixel position and its flux. The distribution of flux around the stars position is known as the PSF and is determined by a combination of the optics, detector and, in the case of ground based observations, the atmosphere (or "seeing"). PSF photometry involves fitting a model to this distribution, and, in a crowded field, the fitting of multiple overlapping PSFs simultaneously.

I chose to use DAOphot, which is one of the oldest, best supported and best established sets of software for PSF photometry. The model DAOphot uses to fit the PSFs of stars has an analytic component and a series of empirical lookup tables that map the residuals of the analytic model from the true PSF. The empirical lookup tables are generated from the data itself through an iterative process of creating the model, subtracting neighbour stars from the stars chosen to create the model and then rebuilding the PSF model from the neighbour-subtracted image. This process is repeated until the PSF model results in a clean subtraction of the stars from the image.

It should be pointed out that the PSF can vary across the image in both X and Y. DAOphot allows the user to solve for this variation, which can be modelled as a linear or quadratic variation in both X and Y.

There is a choice for the analytic model used as well. Three of the more common choices are Gaussian, Moffat and Lorentz functions. The general idea is to choose a model that best describes the shape of the PSF. I only considered space-based observations from HST, therefore I do not have the atmosphere to consider, and thus the PSF is shaped only by the optics and detector. I chose to use the Lorentz analytic model, as it appears to best represent the overall shape of the PSF. The effects of the chosen model are mitigated by the implementation of the residual lookup tables.

3.3 Matches between Filters

The photometry of the sources in our field of view require matching between filters and this is made difficult by the difference in number of sources detected in the different filters. There is also roughly a factor of two difference in the pixel scale between the far-ultraviolet cameras, ACS/SBC and STIS/FUV-MAMA, and the optical cameras, WFPC2 and ACS/WFC.

In order to cross match our sources, I utilized, once again, software created by P. Stetson as part of the DAOphot suite of programs. The programs in question are DAOmatch and DAOmaster. DAOmatch provides an initial transformation of the source positions from one frame to another. These transformations are linear and incorporate rotation, scale and offsets. Once an initial transformation is determined, DAOmaster can be used to refine the transformation by incorporating all the available sources. DAOmaster has the option of allowing for nonlinear (distortion) effects in X and Y. I solved for a quadratic solution in both X and Y, resulting in a transformation with 20 terms and significantly better matches across the entire field of view. For comparison, the initial rough transformation provided by DAOmatch consisted of 7 terms.

The resulting transformations between images is very good, but, given the changes in pixel scale between the far ultraviolet and optical detectors, I limited the accepted match

radius to the size of the (larger) optical pixels, which corresponds to roughly two far ultraviolet pixels.

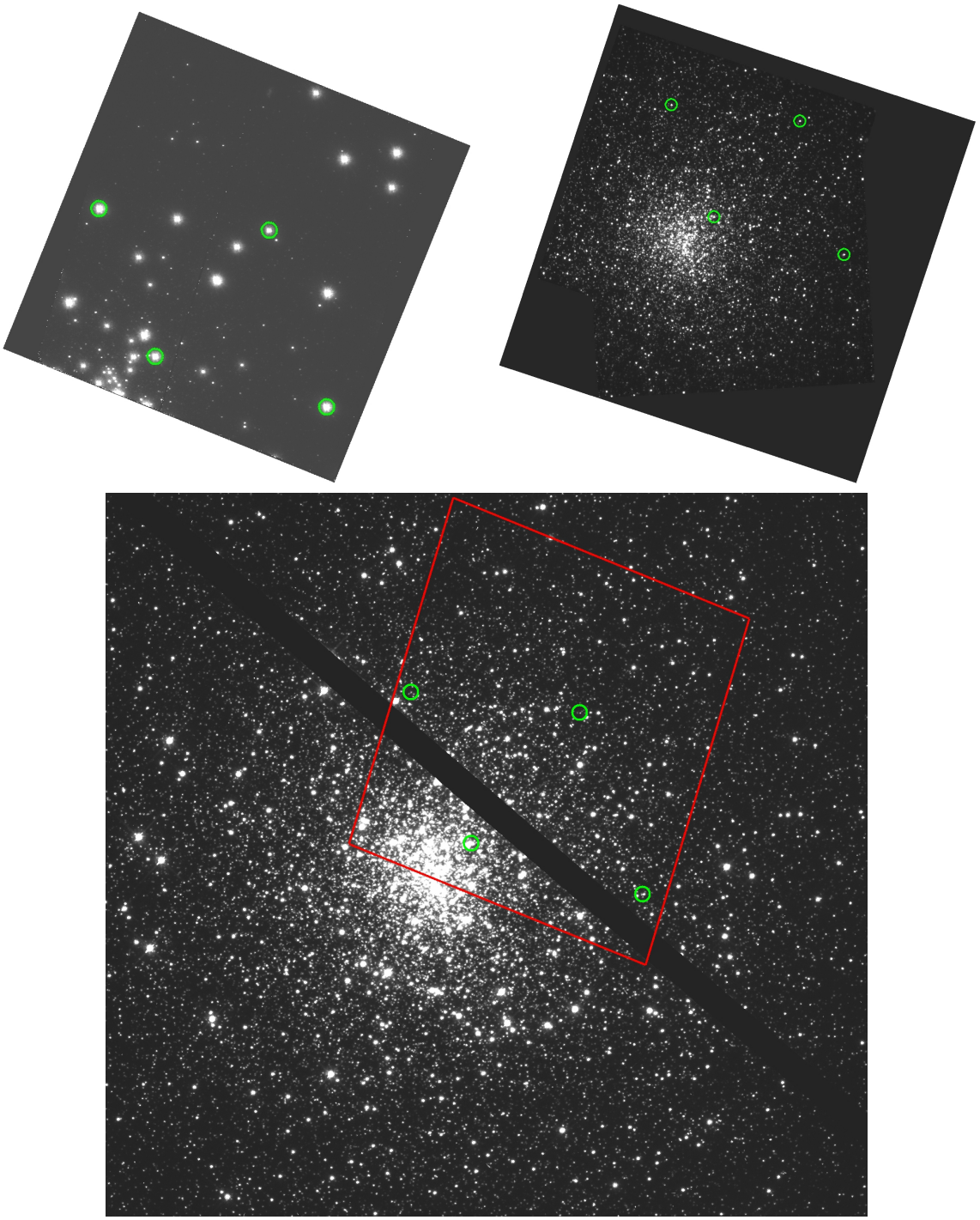

FIGURE 3.2: Images taken with three different filters with north up and east to the left. The top right image is the ACS/SBC F140LP field of view of NGC 1851. The top left image is the WFPC2 F336W field of view of NGC 1851. The bottom image is the ACS/WFC field of view of NGC 1851. The red square is the field of view of the ACS/SBC image. The sources circled in green are the same sources in each image and demonstrates how I match sources between the far ultraviolet, the ultraviolet, and, the optical.

Another consideration is the probability of mismatches, especially between the far ultraviolet and the redder optical images. In our far ultraviolet field of view, there are about 200 bright sources and an additional several hundred lower signal-to-noise sources. Within the same field of view there are several thousand sources in the reddest optical filters. The matching of sources is further complicated because bright far ultraviolet sources may be intrinsically faint in the optical. An estimate of the expected number of chance superpositions among our list of matched sources is given by $N_{false} \sim (N_{FUV} - N_{match}) \times (\pi \times R^2_{match})/A_{FOV}$. This is valid as long as $N_{match} >> N_{false}$ and so long as the spatial gradients in source density across the field of view are not too bad. For the brightest far ultraviolet sources I estimate a 0.3% chance of superposition and for all far ultraviolet sources I calculated a 1.5% chance of superposition. This implies ~ 1 of the brightest 200 far ultraviolet sources and ~ 10 of the remaining sources are likely to be false matches.

I have attempted to minimize the number of false positives by bootstrapping from the far ultraviolet to the reddest filters, i.e. by matching the far ultraviolet sources to sources in the near ultraviolet (see Figure 3.2) and progressively working redwards (i.e. FUV to NUV (F218W and F250W) to U (F300W) to B (F439W) to V (F555W and F606W) to I (F814W)). The use of adjacent wavelength regions increase the chances that the same sources are being identified in both images. These matched catalogs are discussed in Chapter 4.

3.4 Variability

The imaging dataset of NGC 1851 I used in this thesis is unique in globular cluster studies for the number of exposures and temporal resolution in the far ultraviolet. There are 273 exposures taken over 12 orbits on the Hubble Space Telescope. The 12 orbits were divided into 3 visits, each 4 orbits in duration, separated by ~ 2 days (between visit 1 and 2) and ~ 4 days (between visit 2 and 3). Each of the 4 orbit visits has a total of 91 exposures of 90 seconds duration.

The 273 exposures provide an opportunity to detect variability among the sources visible on individual images. The simplest method of detecting variables is the calculation of the standard deviation for each detected source. The mean and standard deviation for all the measured sources is shown in Figure 3.3. Sources with a standard deviation that is $\gtrsim 3\times$ the standard deviation of the mean standard deviation in a 0.2 magnitude bin were selected as candidate variables (the larger blue dots in Figure 3.3). These 21 sources can be considered variable candidates, though they need to be inspected to remove spurious detections, which may be caused by the source being near a detector edge, bad pixels or faint sources located in the wings of a bright variable source. I inspected the 21 sources in Figure 3.3, and only 15 variable candidates survived the

inspection. Sources fainter than a magnitude of ~ 22.5 have a very low signal-to-noise (i.e. S/N$\lesssim 3$) in the individual images. In fact many of the sources are not detected in many of the individual exposures. I decided (confirmed with visual inspection), that while many of these sources could be variables, that sources with a mean magnitude $\gtrsim 22.5$ are too noisy with many non-detections in the individual images.

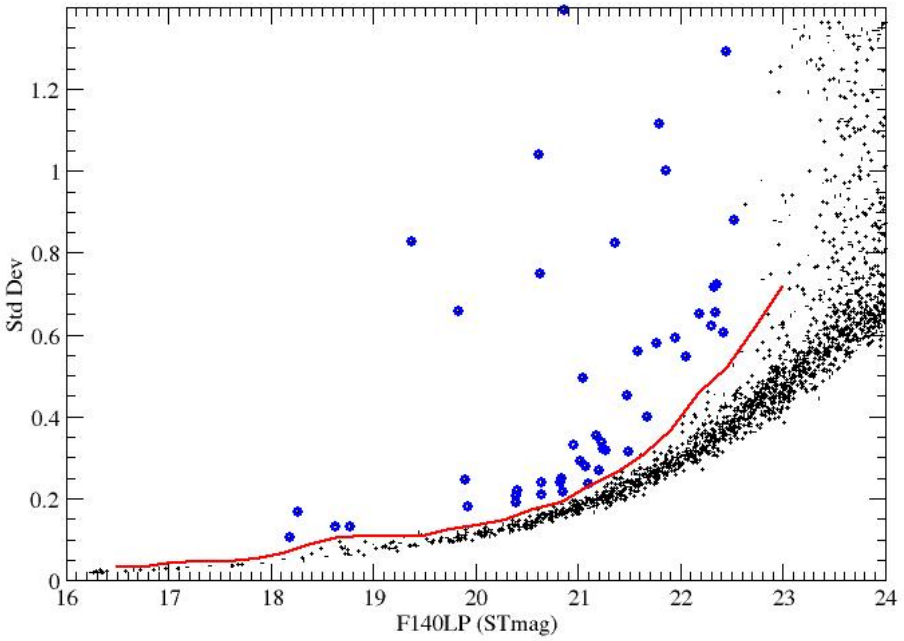

FIGURE 3.3: The standard deviation and average far ultraviolet magnitude for all the sources in our field of view. The larger blue dots are the sources which have a standard deviation $\gtrsim 3\times$ the standard deviation of the mean standard deviation of sources in a 0.2 magnitude bin. The red line represents this limit. Note that no candidates with $\gtrsim 22.5$ magnitude were selected as their signal-to-noise in the individual exposures is very low.

I noticed in our examination of the X-ray binary UCXB 4U 0513-40 (Zurek et al. 2009) that it would not have been found as a $> 3\sigma$ outlier in Figure 3.3. However, when I calculated the Lomb-Scargle periodogram (Press & Rybicki 1989; see below for details), I found a clear signal corresponding to a period of about 17 minutes (Zurek et al. 2009).

Lomb-Scargle (LS) periodogram analysis (Scargle 1982) is mathematically equivalent to fitting sine-waves to the data via least-squares (Lomb 1976). Given the standard normalization of the periodogram, the single-trial "false-alarm probability" is roughly $e^{-P_{LS}}$ where P_{LS} is the LS power. More specifically, given a dataset that consists of uncorrelated Gaussian noise with a constant standard deviation, the probability of finding a power level at least as high P_{LS} when inspecting a single frequency is given

by $e^{-P_{LS}}$. Given that a large number of frequencies are typically inspected, statistical significance is therefore usually achieved for signals reaching $P_{LS,max} \gtrsim 5 - 10$.

I used my Lomb-Scargle code to search for periodic variability among all the brightest far ultraviolet sources (~ 200) and found a total of 36 sources with LS-power $\gtrsim 10$. The 15 variable candidates found above are among these 36 sources. I visually inspected each of the 36 sources on each of the 273 exposures to ensure that its location (i.e. detector edge or bright near by source as mentioned above) is not a concern. One of these 36 sources turns out to be extremely interesting and is discussed in detail in Chapter 7 and Zurek et al (2016).

The observations, periodograms, and phased light curves are presented in Chapter 5. I performed a test for each variable candidate to determine the significance of the power in the Lomb-Scargle periodogram. The test works by shuffling the magnitudes relative to the times of each observation and determining the peak power in the corresponding Lomb-Scargle periodogram. I repeated this 10,000 times for each variable candidate recording the peak power each time. The periodograms presented in Chapter 5 include power levels corresponding to 95%, 99%, and, 99.9% significance derived from the shuffling simulations.

The standard deviation method of finding variable candidates (Figure 3.3) does not take into account any correlation between data points that may exist. By contrast, the Lomb-Scargle technique gains its power from explicitly testing for the presence of periodic signals. Thus the standard deviation method is useful for finding aperiodic variability and/or low-coherence periodic signals. The standard deviation technique requires that the amplitude of variation be relatively large to be detected (most of the candidate variables found this way are RR Lyrae, which display several magnitudes of variation). When the amplitude of variation is low, the standard deviation method is unlikely to find the source as a variable candidate (regardless of the number of data points). However, the Lomb-Scargle technique is very efficient at finding periodic variable candidates with relatively low amplitudes of variation (e.g. 4U 0513-40 – Zurek et al 2009 and FUV1 – Zurek et al. 2016 and Chapter 7).

Chapter 4

Stellar Populations in NGC 1851

Far-Ultraviolet imaging and photometry provides a means of discovering the hot sources in a globular cluster without the severe crowding caused by the much more populous and cooler main sequence and red giant populations. These cooler populations emit very little flux in the far ultraviolet, and the coolest sources are generally not detected.

To understand the far ultraviolet sources that have been detected, I decided to investigate the sources depending on where they are located in a colour-colour diagram, where one colour is the ultraviolet colour, F140LP-F336W, and the other is an optical colour, F606W-F814W. This colour-colour diagram can be seen in Figure 4.1. It has three prominent sequences forming a skewed "Y" shape. I divided the "Y" into three regions and added two additional regions to the left (optically blue) and right (optically red) (see Figure 4.1). I discuss each of these five regions below.

4.1 Region 1: Main Sequence and Evolved Cool Stars

This region of the colour-colour diagram (Figure 4.1) contains the largest population. These stars are drawn from the main sequence and the evolved cool populations, such as the red giants and red horizontal branch stars (see Figure 4.2). All of these sources have a F606W-F814W colour between about 0.2 and 1.0, and a F140LP-F336W colour greater than about 4.0.

These sources are faint in the FUV (F140LP), and many of the detected photons are not detected within the nominal filter range of 1450 Å to 1600 Å. In fact as much as 50% of the detected photons in F140LP for a solar-like star come from wavelengths longer than 1800 Å, since beyond this point there is a steep decline in the detected flux (the exponential Wien tail) (Avila et al 2017). The percentage of detected photons coming from longer wavelengths is even higher for stars cooler than solar analogs. It is likely

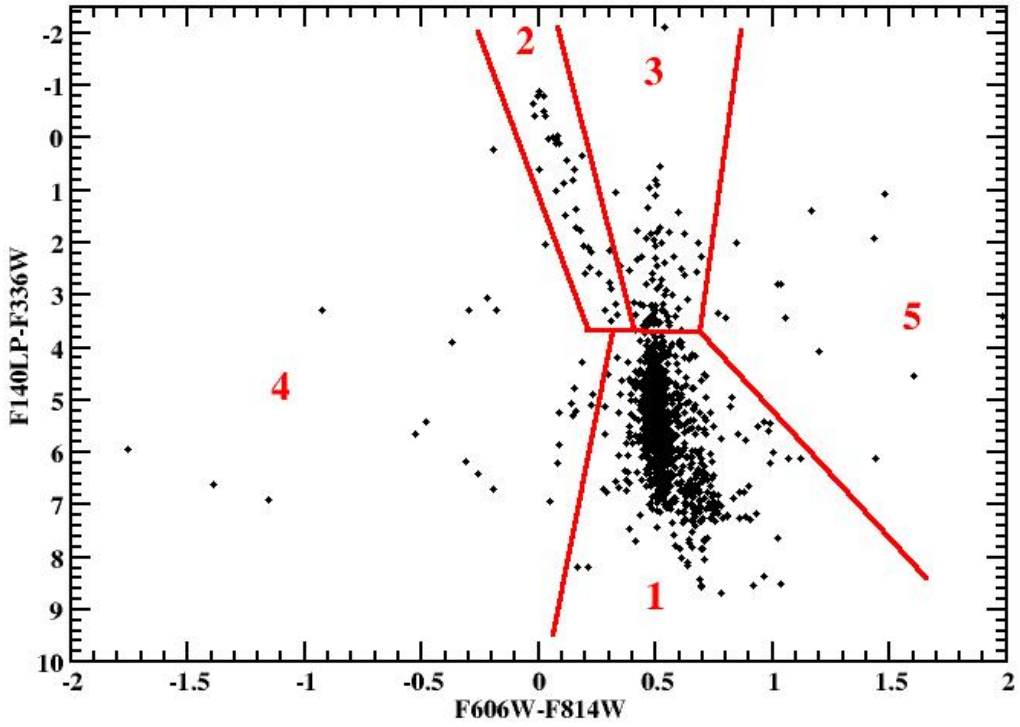

FIGURE 4.1: An ultraviolet-optical colour-colour plot for the ultraviolet detected sources. The ultraviolet colour is F140LP-F336W and the optical colour is F606W-F814W. I have divided the colour-colour plot into 5 regions and are described in individual sections in the text. The boundaries between the regions have been defined by eye trying to isolate various sequences. The boundaries are meant to indicate regions for consideration and to indicate a populations bulk property.

the case that for the coolest stars, such as stars near the red giant branch tip, most of the detected photons are coming from wavelengths longer than 1800 Å.

The signal-to-noise in the FUV for stars in region 1 in the total integration time, 24500 seconds, is very low ($\lesssim 3$). In fact, because of the convolution of the stars spectral shape and the ACS/SBC throughput curves, stars at the red giant branch tip and on main sequence have very similar fluxes in the FUV.

The red leak of the F140LP filter, i.e. its (small) sensitivity beyond $\sim$ 1800Å, as well as the low signal-to-noise in the FUV, cause problems in interpreting the FUV flux for these stars. It is possible that at higher signal-to-noise, corrections could be made with the use of synphot (Laidler et al 2008). However, the globular cluster NGC 1851 (in fact most globular clusters) are at a distance that makes such high signal-to-noise observations prohibitive (i.e. they would require too much observing time). The one exception is the class of the pulsating variables, such as the RR Lyrae, which are the

stars that have a F140LP-F336W colour less than ~ 6.0 and a F336W magnitude less than ~ 19 (see Figure 4.2). I will discuss these systems in Chapter 5.

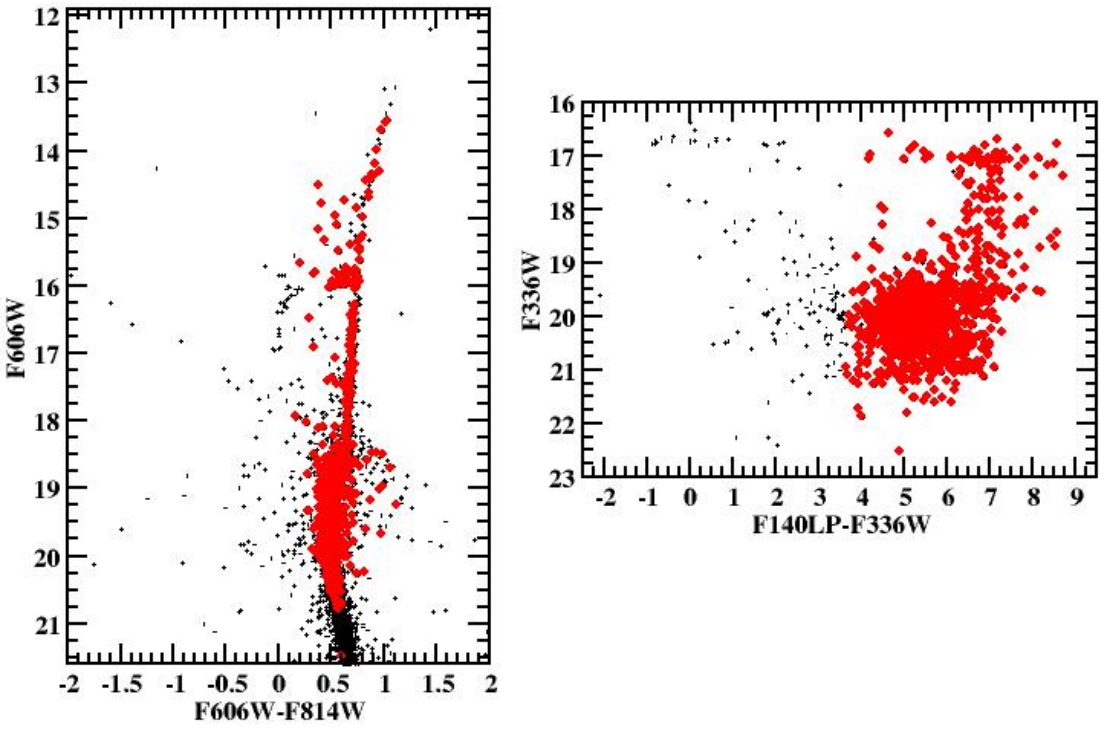

FIGURE 4.2: Left Panel: Optical colour magnitude diagram with the photometry from Milone et al (2008). The red points are the sources from region 1 in Figure 4.1. Right Panel: Ultraviolet colour magnitude diagram with the photometry from this study. The red points are the sources from region 1 in Figure 4.1.

4.2 Region 2: Hot Horizontal Branch and Blue Stragglers

The narrow region labeled as region 2 in Figure 4.1 is composed of hot horizontal branch and blue straggler stars, as indicated by the locations of the sources in Figure 4.3.

The sources with F336W magnitudes greater than 17 (see Figure 4.3) are blue stragglers. As discussed previously, blue stragglers are stars which are more massive, and thus "younger", main sequence stars than the clusters age would indicate. These stars grow in mass through mass transfer in binaries, binary mergers, or, direct collisions. Being more massive and rejuvenated, blue stragglers are located near an extension of the main sequence beyond the nominal turnoff. In Figure 4.3, it can be clearly seen that the blue stragglers fall near the extended main sequence in both CMDs. Blue stragglers

were not all formed at the same time, which explains the "scatter" seen in the CMDs (Figure 4.3). In other words, some of the blue straggler selected in this region are already slightly evolved and have begun to move off the main sequence (i.e. essentially turn off or early subgiant branch stars).

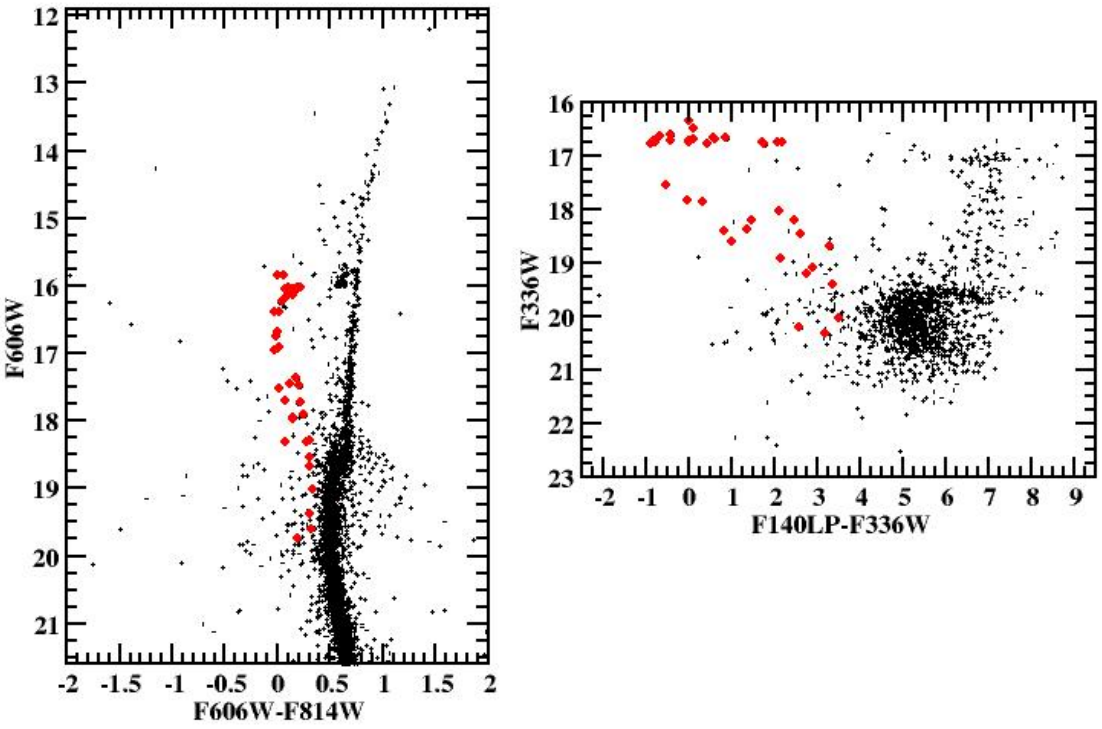

FIGURE 4.3: Left Panel: Optical colour magnitude diagram with the photometry from Milone et al (2008). The red points are the sources from region 2 in Figure 4.1. Right Panel: Ultraviolet colour magnitude diagram with the photometry from this study. The red points are the sources from region 2 in Figure 4.1.

The other sources within region 2 are hot horizontal branch stars (see Figure 4.3). It is interesting that there is only a small spread in colour, but a significant spread in magnitude in the optical for these sources (Figure 4.3). It should also be noted that there is very little range in the F336W magnitude, but a large range of ultraviolet colour (Figure 4.3) for the hot horizontal branch stars. Why do these stars, which are in the same evolutionary state, have these observed properties?

The mass loss histories for the stars on the horizontal branch dictates their locations. Stars which lose more mass during their evolution to the horizontal branch are lower in mass and hotter. The horizontal branch as a whole has temperatures from about 3000 K to 100,000 K. The horizontal branch stars located in region 2 of Figure 4.1 are hotter than about 10,000 K. As an example of why the horizontal branch stars have the

magnitudes and colours they do I have plotted the Planck function for temperatures of 10,000 K to 100,000 K (Figure 4.4).

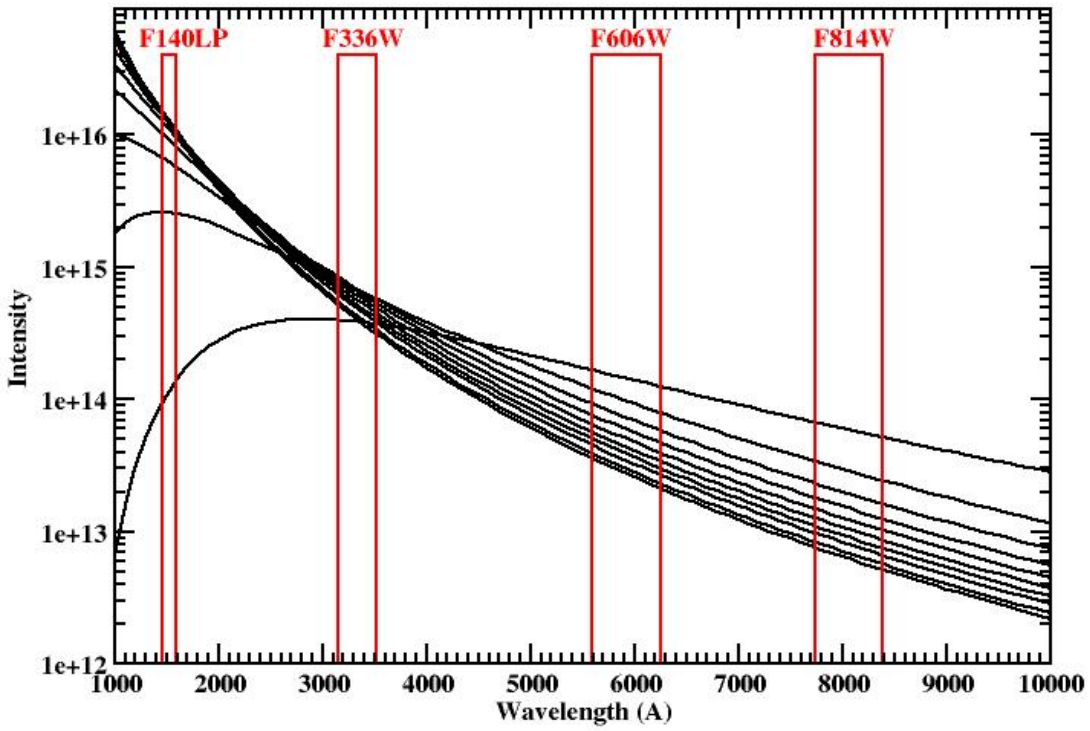

FIGURE 4.4: Intensity curves for the Planck function for temperatures 10,000 K to 100,000 K. The curves represent the range of temperatures of horizontal branch stars in NGC 1851. The four vertical areas labeled with the filters used in this study indicate the filters location and width. The slope between F606W and F814W for all the curves is very similar while between F140LP and F336W they are very different. Also note that the curves have a very similar intensity at the location of the F336W filter.

In Figure 4.4, I have plotted the locations of the filters (see Table 3.1) used in Figure 4.1. For the two filters F606W and F814W, which are in the Rayleigh-Jeans regime, the slopes of the various curves are very similar which explains the narrow colour range in the CMD from these two filters (Figure 4.3). The large range in magnitude of the horizontal branch stars in the optical CMD (Figure 4.3) is also explained by the fact that the coolest sources also have the largest radii and are thus brighter than the hotter stars.

The F336W filter is located at the location where most of the curves cross which explains the nearly identical magnitude seen for these stars in Figure 4.3. The wide range of colours in the ultraviolet (F336W-F140LP) is also easy to understand from Figure 4.4,

given the large change in the curves at the shorter wavelengths where the F140LP filter is located.

Thus, the location of the hot horizontal branch stars in Figure 4.3 is neatly explained by the slope and luminosities of the Planck function adjusted for the radius of the stars (Figure 4.4). This, however, does not explain why the cluster has stars in both the red and blue parts of the horizontal branch. If the multiple population result of Milone et al (2008) is the explanation, it would indicate that the age and abundance differences between the two populations also affects the mass lost in a star's evolution prior to the horizontal branch.

4.3 Region 3: UV excess main sequence stars

The stars in this region of Figure 4.1 are all, except for 4 stars, located on the main sequence in the optical CMD (Figure 4.5). The four exceptions appear to be two RR Lyrae and two blue straggler stars, which are identified based on their locations in the CMDs (Figure 4.5). The RR Lyrae stars are variable and therefore their appearance in this region of Figure 4.1 is uncertain, as the observations for each of the filters were taken at different times. The two apparent blue stragglers may also be variables or they also might be slightly more evolved than the blue stragglers in region 2.

A majority of the sources in region 3 are located on the main sequence in the optical CMD (Figure 4.5) though in the ultraviolet CMD they are to the blue of the main sequence by more than a magnitude in F140LP-F336W (Figure 4.5). Photometric error (in F140LP) may explain some of the reddest sources, but it cannot explain the sources with a F140LP-F336W colour greater than about 3. These sources (maybe all the sources in this region) are likely comprised of multiple components (i.e. two sources blended together).

Assuming that these sources are composed of at least two components implies that one of the components is a small, hot star, which is most likely to be a white dwarf. The implication is that these are main sequence stars with companion white dwarfs. These objects may be cataclysmic variables but, with just the photometric data, mass transfer cannot be inferred and additional information is required (such as variability or the detection of emission lines).

If these are not cataclysmic variables than what are they? They are still likely binaries, though the separations are sufficiently large that the main sequence star is not filling its Roche Lobe. However, the white dwarf must be hotter than about 14,000 K because of its detection in the ultraviolet. White dwarfs hotter than this are relatively young (few $\times 10^8$ yrs), which is a timescale comparable to to the evolution on horizontal branch. Given the numbers of horizontal branch stars within our field of view and noting that

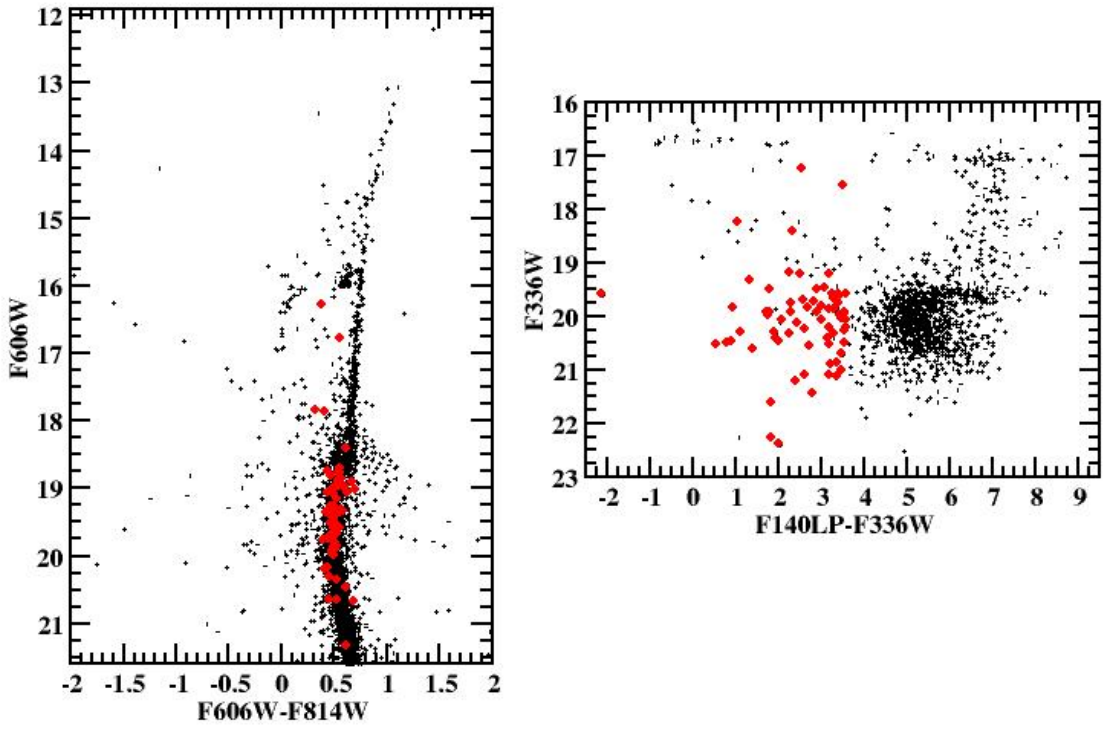

FIGURE 4.5: Left Panel: Optical colour magnitude diagram with the photometry from Milone et al (2008). The red points are the sources from region 3 in Figure 4.1. Right Panel: Ultraviolet colour magnitude diagram with the photometry from this study. The red points are the sources from region 3 in Figure 4.1.

this cooling timescale is comparable to the lifetime of stars on the horizontal branch, these ultraviolet excess main sequence stars from region 3 might be explained by normal carbon-oxygen white dwarfs in binaries with main sequence stars.

This, of course, is too strong of a statement as it would likely require most of the carbon-oxygen white dwarfs hotter than 14,000 K to be in a binary with a main sequence star. If instead of carbon-oxygen white dwarfs we also include helium white dwarfs there is no need to have all the carbon-oxygen white dwarfs in binary. Helium white dwarfs that exist today have not evolved from normal single star evolution (see Chapter 1) and are likely created in a close main sequence binary.

When one of the stars in a close main sequence binary begins its evolution off the main sequence, it also begins to transfer its outer envelope to its companion (this is one of the mechanisms for creating blue stragglers). A white dwarf is created if most of the outer envelope is removed, and the internal pressure on the core is insufficient to continue nuclear fusion. The result is a binary composed of a slightly more massive main

sequence star and a hot stellar core. The stellar core is of insufficient mass to ignite the mostly helium remnant and instead cools as a helium white dwarf. This is in contrast to, carbon-oxygen white dwarfs, that are the products of stellar evolution for single stars with a mass less than $\sim 8M_{\odot}$. Strictly speaking, single stars with, $M_{MS} \approx 0.2M_{\odot}$ will become helium white dwarfs though this will take many Gyrs.

This path for the creation of the helium white dwarf is also thought to be one of the possible mechanisms for creating blue stragglers. Should this process occur with a small mass difference between the two stars, then the star that is slightly more massive will become the helium white dwarf, but the companion star will end up with more mass, this will result in it becoming a more luminous main sequence star (i.e. brighter than the turn off), and thus becoming a blue straggler. This process should also occur for larger mass differences of the initial binary, though the result would not be a visible blue straggler, as the main sequence star that gained mass will still be below the turn off and thus indistinguishable from other main sequence stars (except that it has a hot companion).

I would expect that these types of systems would result in main sequence stars with ultraviolet excesses. As the helium white dwarf cools, it would reduce the ultraviolet excess, which would be seen as an increase in the number of sources towards the main sequence in the ultraviolet CMD. This would be in line with the appearance of Figure 4.5.

With the photometry alone, I can not determine how many of the sources in region 3 are cataclysmic variables, main sequence - carbon-oxygen white dwarfs, or, main sequence - helium white dwarfs, but the best explanation for these ultraviolet excess main sequence stars is one of these scenarios. Additional information such as the detection of emission lines, variability, or X-rays would help characterize these systems.

4.4 Region 4: Optically Blue sources

The sources in this region (Figure 4.1) have been selected as being optically blue, but they can span the entire colour range of F140LP-F336W. The sources in this region with the reddest ultraviolet colours are also the lowest signal-to-noise detections, which is why so many of them are scattered among the redder stars in region 1 (see Figure 4.6). The sources which are near the location of the horizontal branch in the optical and UV colour magnitude diagrams (Figure 4.6) are likely RR Lyrae variables that have been captured at different times in their light curves with the various filters (the observations for each filter were taken at different times).

The sources in this region may not represent a single population. Each of them really needs to be examined individually to determine its nature. This is beyond the scope of the thesis study, but, broadly, the possible explanations for these sources are as follow:

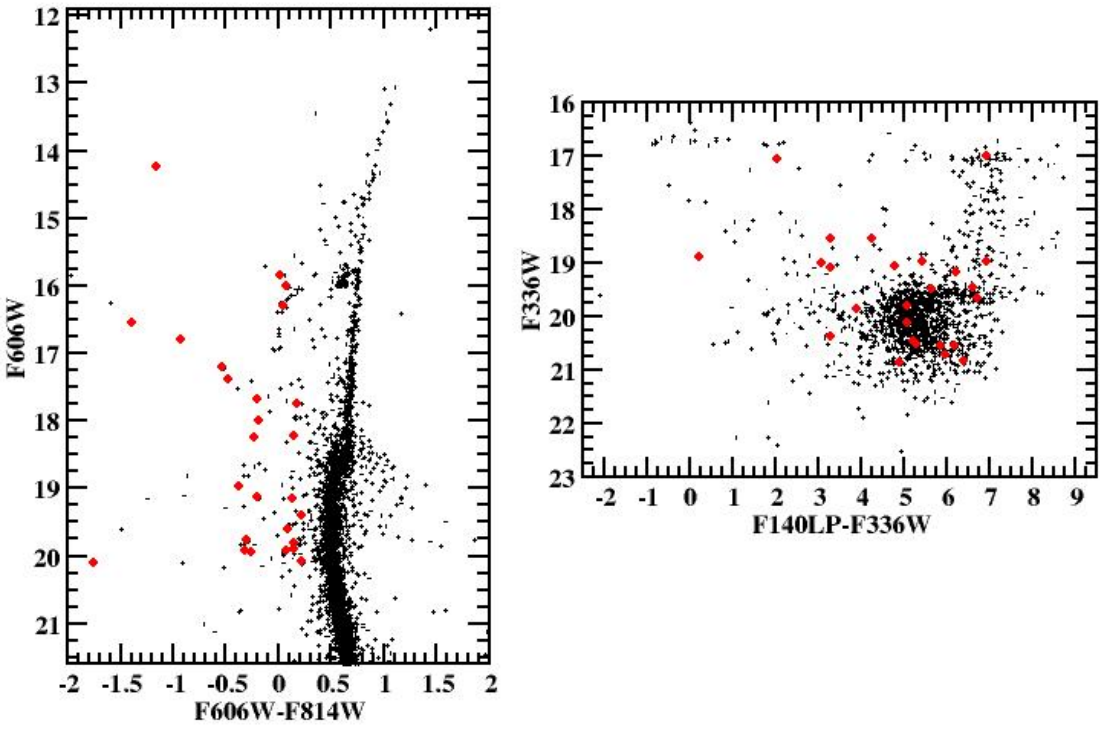

FIGURE 4.6: Left Panel: Optical colour magnitude diagram with the photometry from Milone et al (2008). The red points are the sources from region 4 in Figure 4.1. Right Panel: Ultraviolet colour magnitude diagram with the photometry from this study. The red points are the sources from region 4 in Figure 4.1.

- Cataclysmic variable - CVs in which the optical light is dominated by accretion luminosity would be blue in both of our colours. The accretion heated white dwarf may contribute significantly in the ultraviolet. The detection of variability, emission lines, or X-rays from the source(s) could provide evidence to support or refute this scenario.

- Low mass X-ray binary - This is a similar scenario to that for cataclysmic variables. However, here the central source cannot contribute significantly, even in the ultraviolet, so any ultraviolet photons will be coming from the accretion disk. Again an X-ray identification is needed to support this possibility.

- Blue Straggler - As can be seen from the CMDs in Figure 4.6, a number of sources are located within the area populated by blue stragglers. These behave photometrically like the blue stragglers from region 2, although they are slightly redder

in the ultraviolet. It is important to point out that blue stragglers may not behave entirely like "normal" single stars because of their gain in mass and possible companion. They may also be slightly evolved.

- White Dwarf - A white dwarf that has cooled below about 14,000 K will be a low signal-to-noise source in the ultraviolet observations, but may still be visible in the deep optical observations (although it would still likely be low signal-to-noise). Spectral energy distributions of these sources could be made with the addition of photometry taken at different wavelengths (i.e. 2000Åto 5000Å) and compared to white dwarf and stellar models.

- Triple systems - It is possible that some fraction of the suspected binaries in a globular cluster are actually triples. The three components allow for an extra degree in freedom in creating the colours observed. It is unknown how common such systems are in a globular cluster, but even if they are just 10% of the binaries, there would still be about 10 triple systems in our field of view.

- Chance coincidence - They could be two unrelated sources composed of an ultraviolet and optical source. In other words there are two sources in the GC that happen to lie along the same line of sight but are otherwise not associated with each other. Observationally the two sources must lie within the radius (i.e. ~ 1 ACS/WFC pixel or ~ 2 ACS/SBC pixels) used to match sources in the various filters. An example of chance coincidence can be seen in Chapter 7 where the ultraviolet source and the evolved giant star are likely unrelated.

Any or all of these possibilities may explain the sources in this region. It is likely that a combination of explanations are needed, as some sources are better explained by the blue straggler scenario versus the white dwarf scenario,for example and vice versa. In a future study, a detailed examination of these source with the addition of new Hubble Space Telescope near ultraviolet observations will be undertaken.

4.5 Region 5: Optically Red sources

The sources in this region are located redward of the main evolutionary sequence in NGC 1851 (see Figure 4.7). However, they are generally located blueward of the turn off in the ultraviolet CMD (Figure 4.7). The one notable exception to this is the source which is at the tip of the red giant branch, at magnitude ~ 12.2 in F606W. This source is only faint in Region 5 because the red giant branch curves into this region. The remaining sources are all, except for one, located around a region defined as the sub-sub-giant region (Geller et al. 2017) in the optical colour magnitude diagram (Figure 4.7). The one exception has optical colours consistent with it being a red straggler (Geller et

al. 2017). In the ultraviolet colour magnitude diagram these same sources are mostly located where the blue stragglers are found, i.e. in Regions 2 and 3.

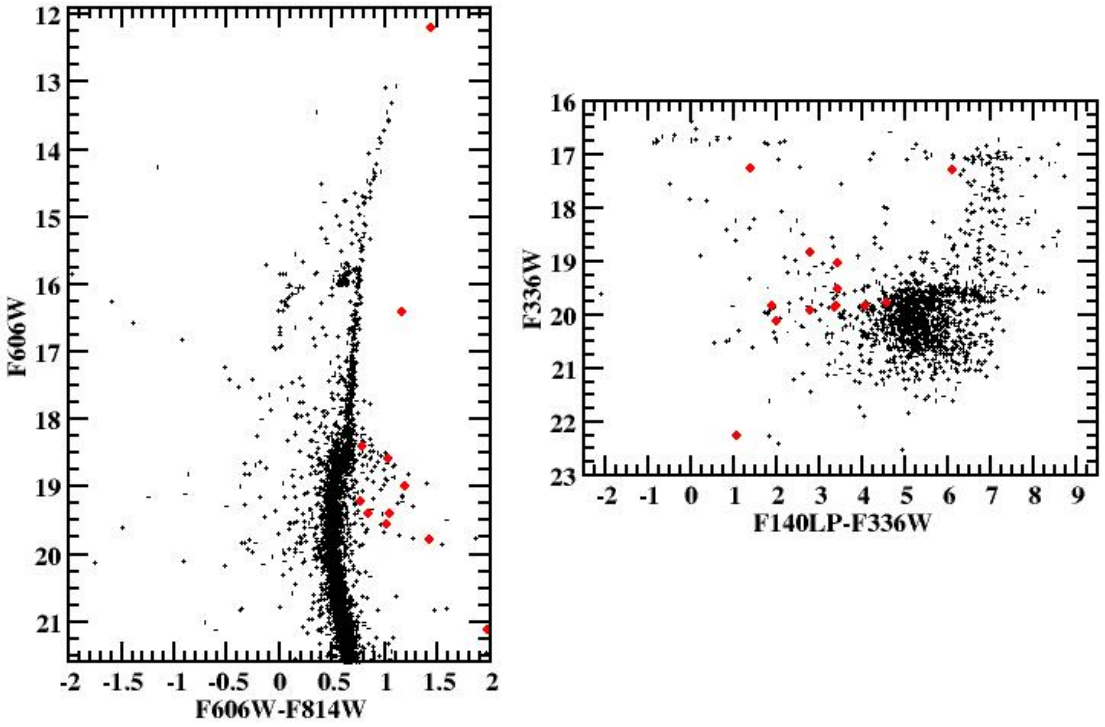

FIGURE 4.7: Left Panel: Optical colour magnitude diagram with the photometry from Milone et al (2008). The red points are the sources from region 5 in Figure 4.1. Right Panel: Ultraviolet colour magnitude diagram with the photometry from this study. The red points are the sources from region 5 in Figure 4.1.

There are only about 10 sources in Region 5. If they are found to be *bona-fide* members of the cluster, this will contribute to our understanding of possible formation channels for sub-sub-giants and red stragglers which are currently still mysterious (Geller et al 2017). The blue colour in the ultraviolet would seem to indicate that there is a hot component similar to the sources in Region 3. A clear indication of a colour excess in the ultraviolet may be an indication that the formation channel for sub-sub-giants is the same as that of blue stragglers, more specifically it may suggest that they are pre-blue stragglers.

4.6 Discussion

It is clear that a multi wavelength photometric study of NGC 1851 has identified and isolated several important populations in the cluster. The ultraviolet excess found in apparent main sequence stars (region 3; Figure 4.5) points toward these sources being multiple component systems, with the simplest explanation being that they are really binaries containing a hot white dwarf and a main sequence star. This would indicate that the optical is dominated by the main sequence star, while the ultraviolet is dominated by the contribution from the hot white dwarf (and possible accretion disk if there is mass transfer).

The blue straggler stars in Region 2 (Figure 4.1 and Figure 4.3) are consistent with being single stars which are on the main sequence but at masses greater than the turn off. The hot horizontal branch stars in Region 2 (Figure 4.1 and Figure 4.3) have the magnitudes and colours they do because of a combination of the Planck function and radius of the stars combining so that the F336W magnitude is nearly the same for all such systems. The optical filters are so far down the tail of the Planck function that the slope changes very little over the temperature range of these stars, a small range of optical colours. By contrast, the slope of the Planck function between the ultraviolet filters, F140LP and F336W, changes significantly with temperature, which explains the large colour spread in the ultraviolet (Figure 4.3).

There are a number of possible explanations for the blue optical sources (Region 4; Figure 4.6) and a star-by-star study, including new Hubble Space Telescope observations in the near ultraviolet and blue optical, will be needed. This is left for a future investigation.

The best explanation for the sources which are optically red, but with an ultraviolet excess, (Region 5; Figure 4.7) is that these belong to a relatively newly identified population known as sub-sub-giants (Geller et al. 2017). The ultraviolet excess would seem to indicate that I may have caught these systems in the act of forming blue stragglers, through the stripping of the outer stellar atmosphere. However, additional observations are needed to constrain their membership of the cluster. If they are cluster members, their existence may be relevant not just for the formation of sub-sub-giants, but formation of blue straggler systems as well.

Throughout this chapter, I have necessarily assumed that all these systems are members of NGC 1851. However, it is of course possible that some of them may be foreground or background sources. I have tried to concentrate on the bulk properties of the various populations rather than any individual source. It may be easy to explain any single source as unassociated with the cluster, but it is much harder to make that claim for ten similar sources. As I have pointed out above, the study of individual sources requires a demonstration of membership, and this is left for a future study with newly obtained

Hubble Space Telescope observations, which can be used to estimate proper motions (e.g. Cadelano et al 2017 and Bellini et al 2017).

Finally, it should be pointed out that the optical imaging goes significantly deeper on the main sequence than the ultraviolet imaging does. While I have been careful in the identifications between filters, it remains a possibility that some of the matches may be in error. Like the cluster membership, this may explain any one source having "peculiar" colours, but it is unlikely to explain entire populations. I have considered the populations as a whole, rather than concentrate on any one source, which should minimize the risk of my interpretation.

Chapter 5

Variable Stars in NGC 1851

The dense cores of globular clusters (GCs) appear to have enhanced populations of compact binaries (e.g. low mass X-ray binaries (LMXBs); Bahramian et al 2013) and the products of binary interactions (e.g. blue stragglers (Knigge et al. 2009) and Helium white dwarfs (Cool et al 1998)). Theoretical studies (Pooley & Hut 2006) suggest that cataclysmic variables (CVs) are also enhanced in GCs, though observations have yet to confirm the numbers these studies suggest. CVs and LMXBs are bright in the far-ultraviolet (as discussed in Chapter 1) and may exhibit variations associated with the binary orbit, accretion disk, or, the spin of the white dwarf (in the case of a CV). The observations I have used in this study have a cadence and duration particularly useful for finding variations of systems like CVs.

There are many different types of variable stars in globular clusters. For the purpose of this thesis, I have split these into three groups: pulsating single stars, binary stars and transients. Even these broad classes have somewhat fluid boundaries (e.g. one of the components of an accreting binary might be a pulsating star, this means that the system may have variability associated with pulsations, stellar orbits, and/or disk instabilities resulting in transitory outbursts (dwarf nova). A simple classification scheme is nevertheless useful in providing a basic theoretical framework for the observations.

5.1 Variable Single Stars: Pulsators

In the Galactic field, mechanisms other than pulsations are available to drive variability among single stars. For example, some young M-dwarfs exhibit strong flaring (the so-called flare stars), while other fast-rotating late-type stars show variations associated with star spots. However, both of these mechanisms are associated with strong magnetic activity, which is strongly correlated with youth and/or fast rotation. As a result, these mechanisms are unlikely to be at work in globular clusters.

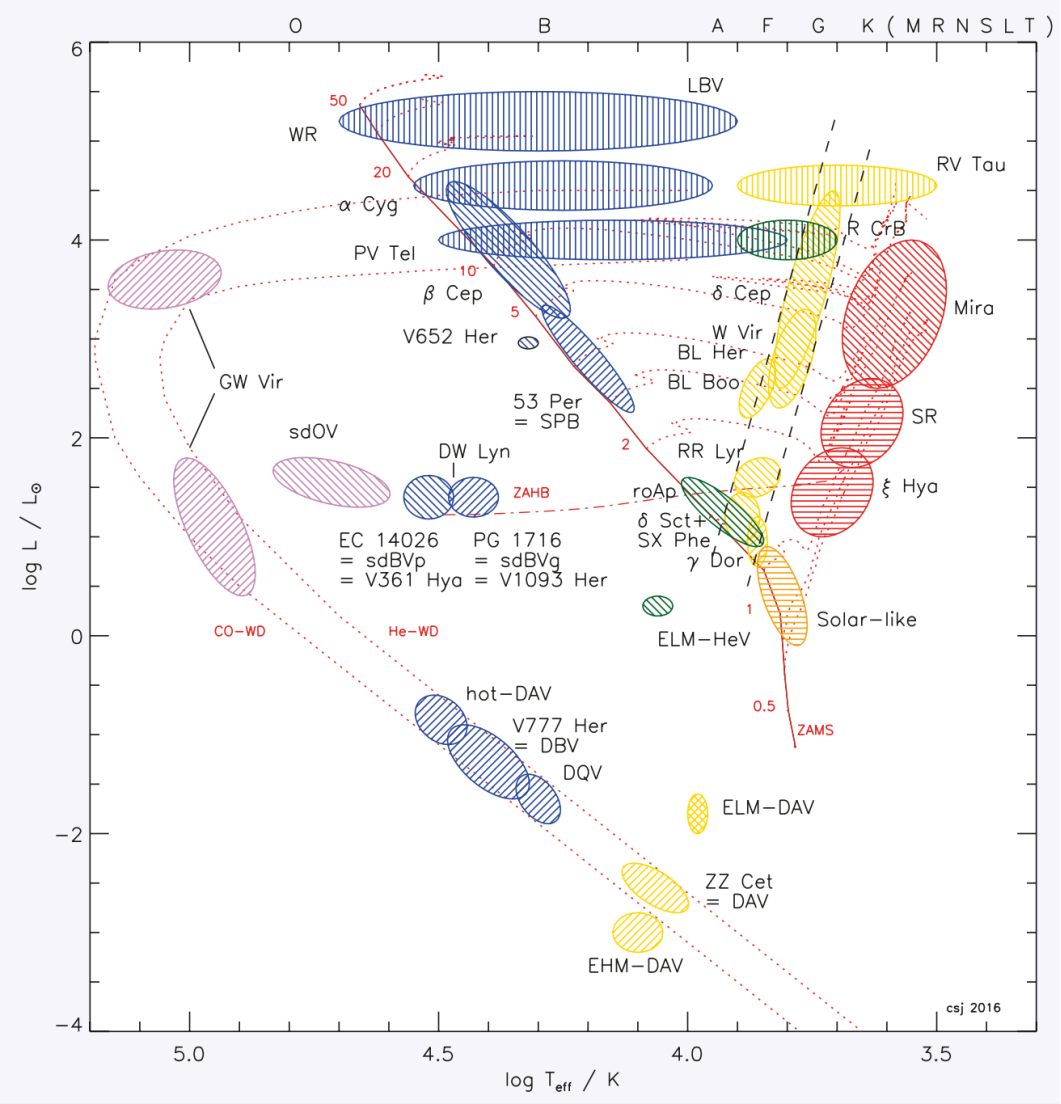

FIGURE 5.1: Pulsating variable stars across the Hertzsprung Russell Diagram (Kurtz et al 2016).

There is one possible exception to this: blue stragglers (see Chapter 1). Single blue stragglers formed from the merger of two stars might be unusually fast rotators (although there is little evidence to back this up at the moment [Lovisi et al. 2013]). This "rejuvenation" might in turn produce an increase in the magnetic activity level of these objects. However, all known blue stragglers in globular clusters are A/F stars. Strong magnetic activity is rarely seen at these spectral types, even at fast rotation rates (Balona et al. 2016).

Given the above, pulsations are the main mechanism for the observed variability among single stars in globular clusters. The most common physical mechanism for these pulsations (the so-called κ-mechanism) is related to the sensitive dependence of opacity on temperature, usually associated with hydrogen and/or helium ionization state switches.

In the case of RR Lyrae and Cepheid variables, for example (see below), the relevant ionization switch is between He II and He III. The result is an instability that causes radial "breathing", with the stellar radius and temperature periodically increasing and decreasing. This, in turn, produces the observed brightness variations which appear as a distinctive sawtooth pattern in the light curve. However, this mechanism only works for stars within a set of narrow "instability strips" across the HR diagram (Figure 5.1).

The classic instability strip contains several types of pulsators, which are distinguished by their mass and evolutionary state (Figure 5.1):

- **Cepheids** with periods of days to months and masses greater than four times that of the sun (Sandage & Tammann 2006). These are powered by the κ-mechanism and located in the classic instability strip. They are used to anchor the distance scale for supernovae Ia which are used in cosmological studies. This type of variable is not present in globular clusters as their masses are more than 4 times that of the turnoff mass.

- **Mira Variables** have periods of about 100 days or greater and are located near the tip of the red and asymptotic giant branches (Willson & Marengo 2012). The way in which the pulsations in these stars are excited is not well known, but it may be the standard κ-mechanism, in this case associated with the ionization of hydrogen if the star is on the red giant branch and helium if on the asymptotic giant branch . While these systems may exist in globular clusters, the variations they exhibit would not be detectable in the observations used here which span about 8 days.

- **Delta Scuti** variables are main sequence stars with masses between about $2.5 - 1.5 M_{\odot}$ (spectral types of A and F) which have pulsations powered by the κ-mechanism. They have periods between ~ 0.02 and ~ 0.3 days with amplitudes in the optical between 0.01 and 0.8 magnitudes (Sandage & Tammann 2006). These systems are found among the more metal rich populations of the Galaxy, such as those in the Galactic disk and in open clusters. NGC 1851 is a metal poor globular cluster ([Fe/H]~ -1.18) in the halo of the Galaxy, therefore, Delta Scuti variables are not expected to be found in the observations used in this thesis.

- **SX Phoenicis** variables are the metal poor equivalent of Delta Scuti variables. As in the Delta Scuti stars, the pulsations of SX Phoenicis variables are powered by the κ-mechanism. SX Phoenicis stars are found nearly exclusively in the Galactic halo and globular clusters. Their masses are larger than a solar mass (i.e. more massive than the turn off in a globular cluster) and are therefore part of the blue straggler populations in globular clusters and the Galactic halo. The periods of SX Phoenicis stars have periods comparable to Delta scuti stars (i.e. ~ 40 minutes to ~ 8 hours; Sandage & Tammann 2006). The time series data used in this thesis are sensitive to this variable type as this period range is well sampled.

- **ZZ Ceti** stars are pulsating white dwarf stars (also known as DAVs or DBVs) in the temperature range of about $10,000$ to $13,000$ K and have periods between about 30 seconds and 30 minutes. The pulsations are non-radial and are still driven by the κ-mechanism (Corsico et al. 2016). The period range is detectable with the observations used in this thesis though the luminosity of these variables is at or below the detection limit of the individual ultraviolet exposures.

- **RR Lyrae** stars are pulsating horizontal branch stars. The pulsations are powered by the κ-mechanism and have periods between $\sim 7 - 24$ hours. They have been found in many globular clusters (Sandage & Tammann 2006). RR Lyrae are discoverable in the observations used in this thesis because their periods are well matched to the cadence of the data set, and the amplitude of their variations is large in the far ultraviolet band (as mentioned in Chapter 1).

- Some **subdwarf O & B** stars, which are horizontal branch stars at the hot end ($> 10,000$K), have been found to be pulsating on time scales of $\sim 1 - 45$ minutes (Randall et al. 2016) and up to several hours (Ostensen et al. 2012). The observed amplitudes of these variations is small (Reed et al. 2009). The observations used in this thesis are suitable for discovering if any of the hot horizontal branch stars are varying like those discovered in the field.

Based on the above, it is expected that the FUV observations in this thesis – which cover time-scales of minutes to days – to be particularly effective for detecting and characterizing the variability of blue stragglers with star spots, pulsating blue stragglers known as SX Phoenicis stars, ZZ Ceti stars (pulsating white dwarfs), RR lyrae (pulsating horizontal branch stars), and, pulsating subdwarf O & B stars.

5.2 Binary Stars and Higher-order Multiple Systems

Binary stars are the most common multi-star system, though it is thought that some fraction of binary systems are actually in higher order systems, such as triples. Triple and higher-order multiple star systems are dynamically stable, so long as the ratio(s) of inner and outer orbits is/are sufficiently large. (For this reason, stable triple systems are also often referred to as "hierarchical triples".) In the Galactic field, such configurations can survive for arbitrarily long times. However, in globular clusters, binaries and multiple star systems with large outer orbits ($\gtrsim$ 1AU) are subject to disruption on time-scales shorter than typical GC ages (Ivanova et al. 2005). I therefore do not expect to find – and have not found – many long-period binaries or higher-order systems in GCs. For the rest of this section, I will therefore focus on variability associated with binary stars.

There are three basic types of binary systems: detached, semi-detached, and contact. A detached system is one in which the equilibrium radii of both stars in the binary fit

within their respective Roche lobes (see Chapter 1). A semi-detached system is one in which one of the stars in a binary is filling its Roche lobe. Finally, a contact binary is one in which both stars are filling their Roche lobes.

Detached systems can be composed of two stars of different masses and evolutionary states. The requirement that the stellar radii of both components must remain within their respective Roche lobes implies that the allowed orbital periods for detached binary systems depend on their masses, radii and evolutionary states. For example, detached double WDs can have orbital periods $\lesssim$ 1 hr (e.g. Nelemans et al. 2001), while a detached binary containing a $100R_{\odot}$ red giant must necessarily have an orbital period $\gtrsim$ 3 yrs. In a globular cluster, especially in the core, where the encounter rate between stars and binaries is high, it is unlikely that large separations survive. It is also likely that binaries characterized by large mass ratios do not survive either, as, in general, in an encounter between a binary and star (or another binary), the lowest mass star will be ejected from the system (and perhaps the cluster). The result of such "exchange interactions" is the creation of a binary with a smaller difference in mass between the components.

In semi-detached systems, one of the stars in the binary fills its Roche lobe. In these systems mass is transferred to the other star. Two examples of this type of system are cataclysmic variables and low-mass x-ray binaries (see Chapter 1).

Contact binaries have both stars in the system filling their respective Roche lobes, and thus the surfaces of the two stars are in contact. The W Ursa Majoris class of binaries is this type of binary. In a W Ursa Majoris binary, the two stars have nearly the same temperature because any initial difference between the two stars is equalized by the surface flows once the stars come into contact.

The numbers of contact, semi-detached and detached binaries may all be enhanced or reduced in globular clusters relative to the Galactic field, since the star-star, star-binary, and, binary-binary interactions that can create, modify or destroy them are much more common in the dense cores of globular clusters. The observations used in this thesis are ideal for the discovery of these systems. The main concern is whether a high-enough signal-to-noise ratio can be achieved to detect these types of binaries – and their variations – in the 90 second FUV exposures on which my variability analysis is based. This will depend on the temperature, brightness and variability amplitude of the candidate variable in question.

5.3 Discovered Variables

The selection of candidate variables stars in the ACS/SBC field of view has already been discussed in detail in Chapter 3. Briefly, focusing on the 200 brightest far-UV

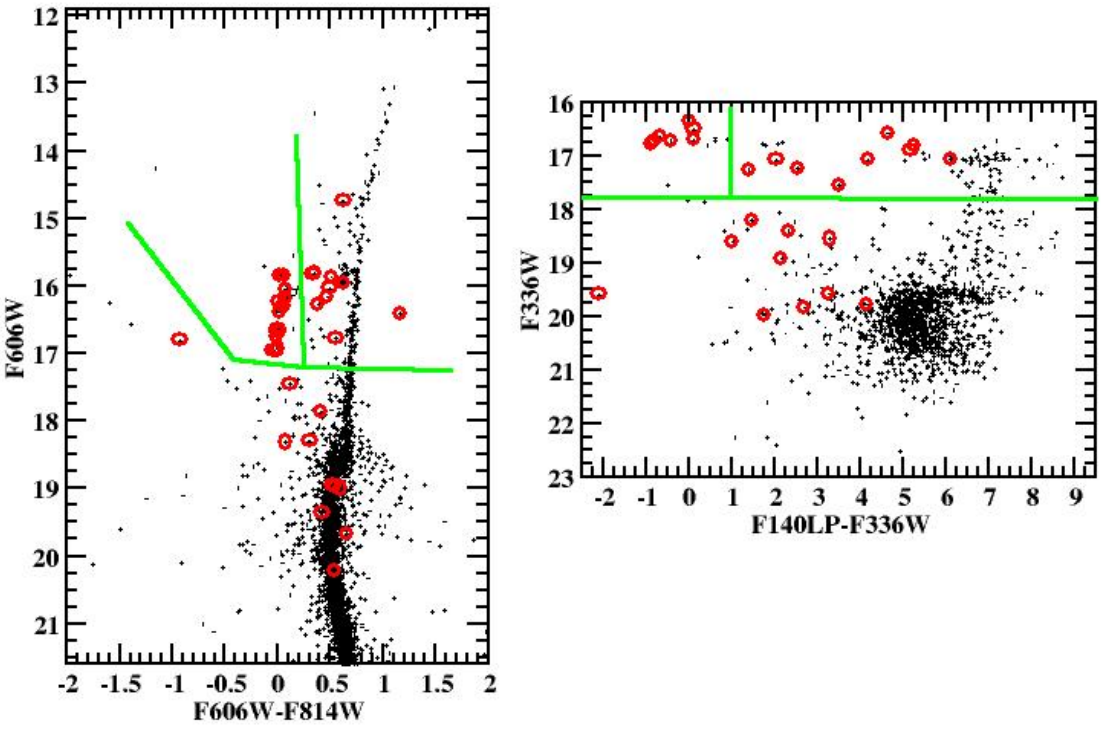

FIGURE 5.2: The optical (left: F606W vs F606W-F814W) and ultraviolet (right: F336W vs F140LP-F336W) colour magnitude diagrams (similar to Figure 4.2) with the 35 variable candidates over plotted as red circles on both diagrams. The three regions, delineated by green lines, of variables discussed in the text can be distinguished best in the ultraviolet colour magnitude diagram. The RR Lyrae located to the red of F140LP-F336W colour of ~ 1.0 and brighter than ~ 18 in F336W. The blue stragglers and white dwarf binaris are the sources fainter than ~ 18 in F336W. The blue horizontal branch variable candidates have an ultraviolet colour less than ~ 1.0 and are brighter than ~ 17.0 in F336W.

sources, I first identified candidate variable based on their location in the RMS variability vs magnitude plane (Figure 3.3). After removing false positives by visual inspection of each source, this yielded 15 likely variables. I then also constructed Lomb-Scargle periodograms for all 200 sources, since this can allow periodic signals to be detected in time series characterized by RMS variability below the normal detection threshold. I considered a star to be a periodic variable candidate if the Lomb-Scargle periodogram included a peak with power $\gtrsim 10$ (see Chapter 3). This yielded a total of 36 candidates, which included all 15 of the candidates found via the RMS analysis.

As already discussed in Chapter 3, I carried out randomization tests in order to determine the significance of peaks in the power spectra. Again, briefly, this involved shuffling the times and magnitudes in each time series against each other to produce mock data sets

to contain only white noise, but share the exact magnitude distribution of the real data set. The Lomb-Scargle periodogram was then calculated for each shuffled mock data set, and the peak power was recorded. I repeated this 10,000 times for each variable candidate. Finally, sorting the resulting 10,000 peak power values from lowest to highest I selected the 95, 99, 99.9 percentage values. These values are plotted as red horizontal lines in the power spectra for each variable candidate (e.g. Figure 5.3).

In the discussion for each of the variable candidates below, I also indicate the uncertainty on the specific period suggested by the highest peak in the power spectrum. Since this uncertainty is set by a combination of noise, light curve shape and sampling pattern, I estimated it via bootstrap simulations. Specifically, for each variable candidate, I again created 10,000 mock data sets of the same size as the real data set, but this time by drawing (time, magnitude) pairs from the real data set *with replacement*. I then again calculate Lomb-Scargle periodograms for each mock data set and recorded the period associated with the peak in the periodogram. The distribution of these periods can then be used as an estimate of the relative likelihood that any given period actually produced the observed signal (see Figure 5.6, Figure 5.10, and Figure 5.15). The result of these tests is discussed for each variable candidate.

In Figure 5.2 I have plotted where the variables are located in both the optical and ultraviolet colour magnitude diagrams. Figure 5.2 allows us to divide the variables into three classes depending on their photometric properties and likely stellar components. The three photometrically defined classes are as follows: RR Lyraes - objects red of a F140LP-F336W colour of 1 and brighter than $\sim$ 18 in F336W, Blue Stragglers and white dwarf binaries - sources fainter than $\sim$ 18 in F336W, and, blue horizontal branch stars - sources blue of a F140LP-F336W colour of 1 and brighter than $\sim$ 17 in F336W. In the subsections below, I discuss each of these variable types.

5.3.1 RR Lyraes

There are 11 variables which I have classified as RR Lyrae stars, based on their magnitudes and colours in Figure 5.2. As discussed in Chapter 1 and above, RR Lyrae are pulsating variables located in what is known as the instability strip. The actual magnitudes and colours of these stars in Figure 5.2 are somewhat uncertain as the F140LP magnitude is the mean magnitude of all 273 observations, and the magnitudes for F336W, F606W, and, F814W may be from any point within each stars light curve. In Table 5.1 I present the magnitudes used in Figure 5.2. In Figure 5.3, Figure 5.4, and, Figure 5.5 I present the observations, the power spectrum, and, phased light curve for each of the variables in Table 5.1. The period corresponding to the highest peak in the power spectrum is presented in Table 5.1. These are the periods adopted for the phase light curve plots. I discuss each of the variables and their light curves below.

Name	RA (J2000) (hh:mm:ss.s)	DEC (J2000) (dd:mm:ss.s)	Period (hours)	F140LP (STmag)	F336W (STmag)	F606W (STmag)	F814W (STmag)
FUV2	5:14:05.928	-40:02:46.039	12.3(±0.07)	22.06	16.81	14.75	14.12
FUV3	5:14:06.487	-40:02:41.839	8.2(±0.05)	23.18	17.07	15.96	15.32
FUV4	5:14:05.972	-40:02:36.603	8.9(±0.02)	21.27	17.08	15.84	15.50
FUV5	5:14:05.050	-40:02:40.249	6.7(±0.01)	19.11	17.08	15.85	15.83
FUV6	5:14:07.134	-40:02:44.748	9.5(±0.03)	19.78	17.24	16.28	15.89
FUV7	5:14:04.569	-40:02:28.962	22.0(±0.21)	21.96		15.88	15.36
FUV8	5:14:05.495	-40:02:21.291	18.6(±0.10)	22.00		16.17	15.70
FUV9	5:14:06.306	-40:02:47.953	8.9(±0.03)	21.23	16.59	15.82	15.46
FUV10	5:14:06.811	-40:02:44.586	93.6(±1.1)	22.07	16.90	16.04	15.55
FUV11	5:14:06.135	-40:02:47.290	3.1(±0.002)	21.05	17.55	16.78	16.22
FUV12	5:14:06.543	-40:02:48.939	9.6(±0.03)	18.68	16.72	16.42	15.25

TABLE 5.1: The candidate RR Lyrae variables found in this study. The periods correspond to the peak with the most power in the power spectrum (see Figure 5.3, Figure 5.4, and, Figure 5.5). The value in the brackets after the period is derived from the bootstrap trials (Chapter 5.6) as $3 \times \sigma$ of the peak. The magnitudes are on the space telescope magnitude system. The variable candidates without a F336W magnitude are in a region of the field of view in that is not covered by the F336W image. The positions are calculated using the world coordinate system associated with the combined drizzled image of all the ACS/SBC images.

FUV2, top row of Figure 5.3, appears to have a period of $\approx$ 12.3 hours with a power above the 99.9% level. The bootstrap analysis (Figure 5.6) indicates that the most significant peak is located at a frequency of 1.948 cycles per day (c/d), a period of 12.3 hours, with $\sim$ 7300 trials in the peak. FUV2 is located about 1.5 magnitudes above the horizontal branch in the optical CMD (Figure 5.2). While the magnitudes in the optical are taken at unknown points in the stars period it is $\sim$ 1 magnitude brighter than the level of the horizontal branch. If this $\sim$ 1 magnitude is from the stars variation, it is larger in amplitude than the typical optical variations for RR Lyrae (e.g. Braga et al. 2016). A possible explanation for this is that this star is an evolved horizontal branch star (i.e. asymptotic giant branch star) that is evolving through the instability strip. The scatter in the light curve is similar in magnitude to the amplitude of the variation. The signal-to-noise for this star in the individual ACS/SBC exposures is low ($\lesssim$ 10) and this is the likely reason that there is significant scatter.

FUV3, second row of Figure 5.3, appears to have a period of $\approx$ 8.2 hours with a power at the 99.9% level. The bootstrap analysis (Figure 5.6) indicates that the most significant peak is located at a frequency of 2.911 c/d, a period of $\approx$ 8.2 hours, with $\sim$ 1900 trials. In the optical, FUV3 appears where RR Lyrae are expected, while in the ultraviolet, it is the reddest of this set of variables (Figure 5.2). The amplitude of the variation seen (Figure 5.3) is only about a magnitude. It may be that the maximum was not observed in the observations, in which case the mean magnitude in F140LP would be underestimated.

FUV4, third row of Figure 5.3, has two peaks of nearly equal value well above the 99.9% level. These two peaks correspond to periods of $\approx$ 7.4 hours and $\approx$ 8.9 hours. In Figure 5.6 these two peaks have $\sim$ 4700 trials associated with them. The $\approx$ 7.4 hour

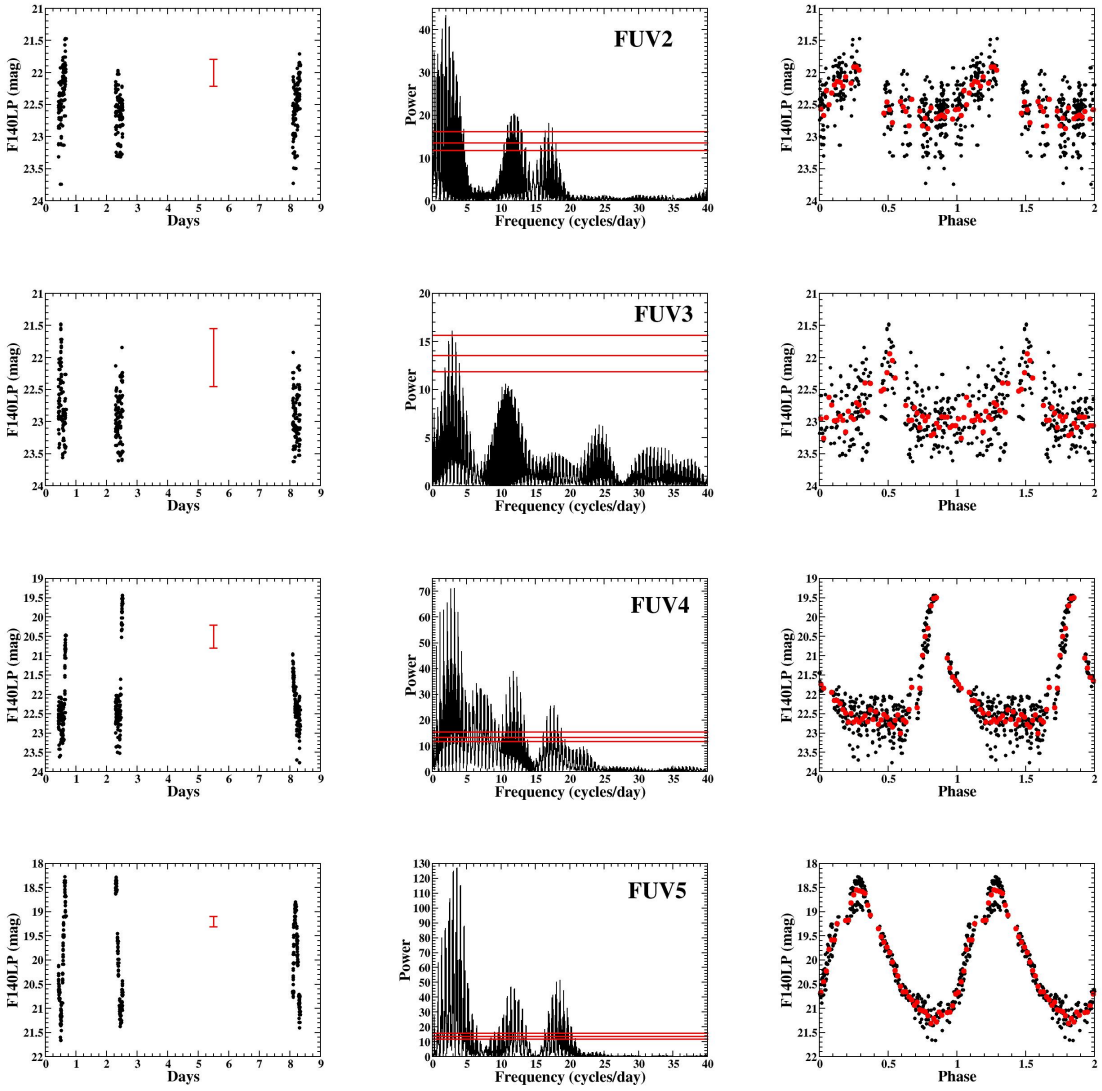

FIGURE 5.3: Each row is for a variable candidate (**FUV2**, **FUV3**, **FUV4**, and, **FUV5**) labeled in the middle plot. The left most column of figures is the photometry for the variable as a function of the time of the observation. Note the distinctive pattern of the three visits. The red bar at 5.5 days (between visits 2 and 3) has a length 2× the mean photometric error. The middle column is the power spectrum of the observations with the power on the y-axis and frequency (cycles/day) on the x-axis. The more likely frequencies have the most power. The red horizontal lines, from bottom to top, are the 95%, 99%, and 99.9% confidence levels from the shuffling of the data (as described in the text). The right most column is the observations phased on the best frequency from the middle panel. The red dots are the mean magnitude for each 0.02 of phase. Each of these variable candidates is discussed in the text.

period results in overlap of the rising data with the declining data. This is the reason I chose to phase the data on the period of $\approx$ 8.9 hours (Figure 5.3). The light curve has a sawtooth shape with an amplitude of about 3 magnitudes which is indicative of a pulsating variable.

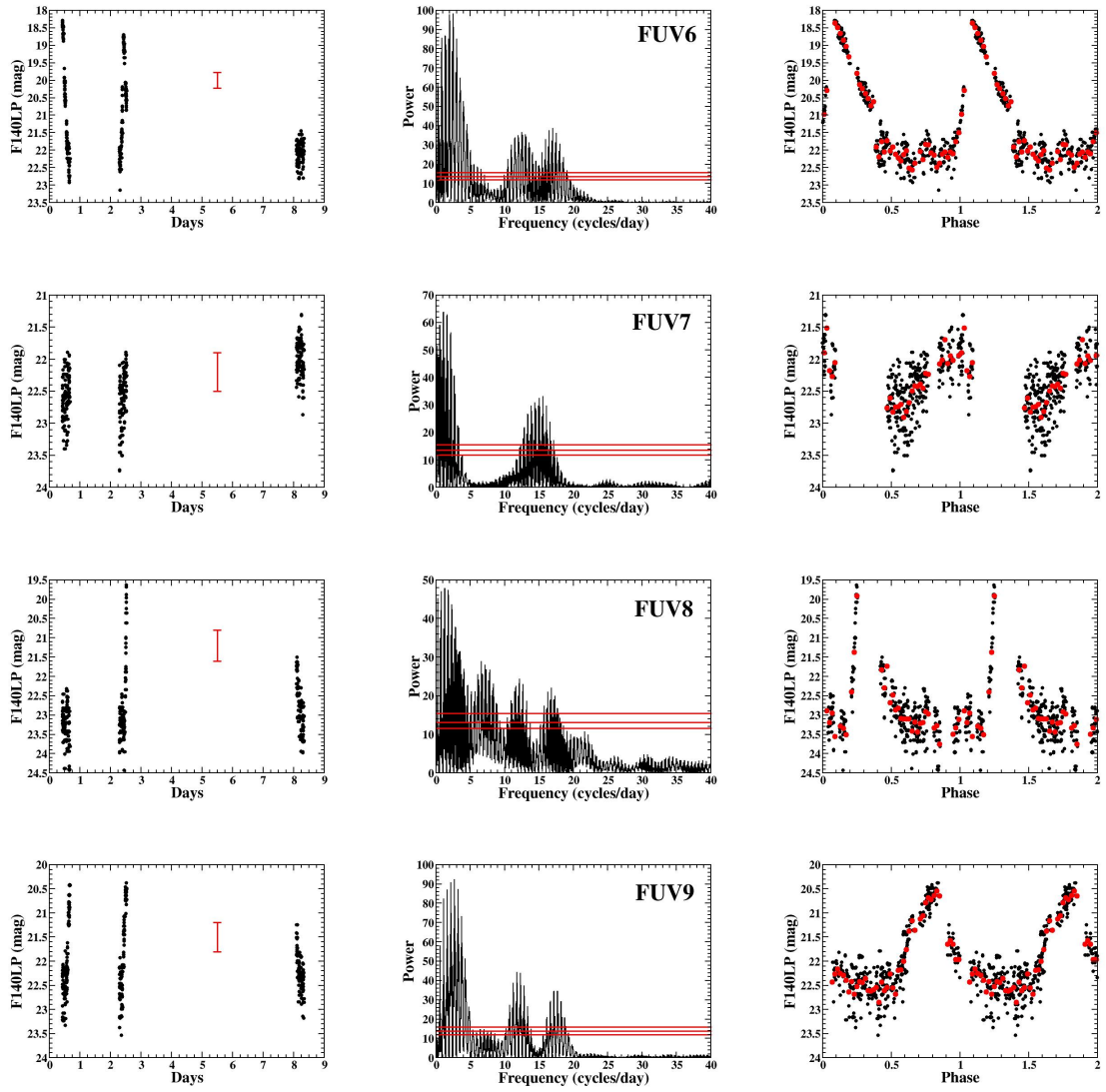

FIGURE 5.4: Each row is for a variable candidate (**FUV6**, **FUV7**, **FUV8**, and, **FUV9**) labeled on the left. The left most column of figures is the photometry for the variable as a function of the time of the observation. Note the distinctive pattern of the three visits. The red bar at 5.5 days (between visits 2 and 3) has a length 2× the mean photometric error. The middle column is the power spectrum of the observations with the power on the y-axis and frequency (cycles/day) on the x-axis. The more likely frequencies have the most power. The right most column is the observations phased on the best frequency from the middle panel. The red dots are the mean magnitude for each 0.02 of phase. Each of these variable candidates is discussed in the text.

FUV5, fourth (or bottom) row of Figure 5.3, has a number of peaks well above the 99.9% level in the power spectrum with the largest peak corresponding to a period of $\approx$ 6.7 hours. The bootstrap trials (Figure 5.6) produced a peak at 3.5777 c/d with more than $\sim$ 9250 trials. The phased light curve, Figure 5.3, has a sawtooth shape with the rise to maximum being faster than the decrease to minimum. The maximum was observed twice during the observations and there appears to be a difference between the two. This difference could be the result of multi-mode pulsations, though further

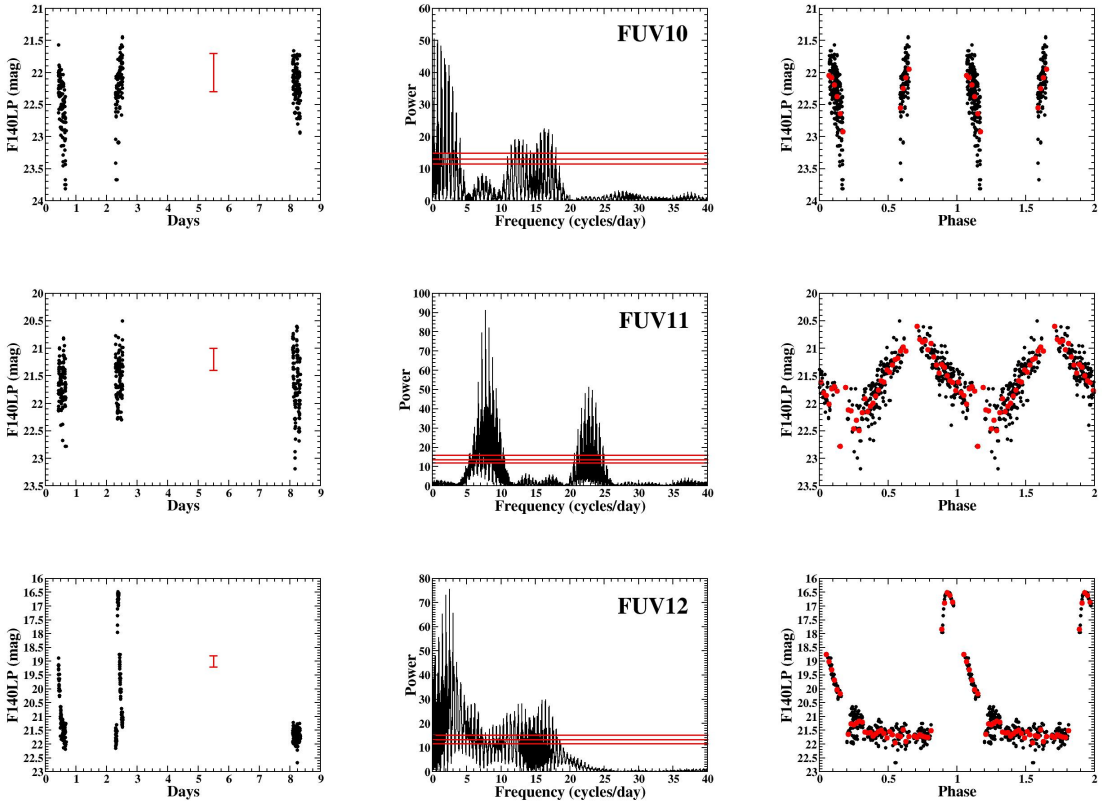

FIGURE 5.5: Each row is for a variable candidate (**FUV10**, **FUV11**, and, **FUV12**) labeled on the left. The left most column of figures is the photometry for the variable as a function of the time of the observation. Note the distinctive pattern of the three visits. The red bar at 5.5 days (between visits 2 and 3) has a length 2× the mean photometric error. The middle column is the power spectrum of the observations with the power on the y-axis and frequency (cycles/day) on the x-axis. The more likely frequencies have the most power. The right most column is the observations phased on the best frequency from the middle panel. The red dots are the mean magnitude for each 0.02 of phase. Each of these variable candidates is discussed in the text.

observations would be required.

FUV6, first (or top) row of Figure 5.4, has a number of peaks well above the 99.9% level in the power spectrum with the largest peak corresponding to a period of $\approx$ 9.5 hours. The bootstrap trials (Figure 5.6) produced two peaks with the largest peak corresponding to the period $\approx$ 9.5 hours with $\sim$ 3850 trials in the peak. The second peak corresponding to a period of $\approx$ 12 hours results in a poorly aligned phased light curve. I phased the data on the $\approx$ 9.5 hour period (Figure 5.4) which shows the distinctive sawtooth shape of a pulsating variable with an amplitude of $\sim$ 3.5 magnitudes.

FUV7, second row of Figure 5.4, has a number of peaks well above the 99.9% level in the power spectrum with the largest peak corresponding to a period of $\approx$ 22.0 hours. The bootstrap trials (Figure 5.6) produced 3 peaks. The largest peak has $\sim$ 6400 trials associated with it and a frequency of 1.0921 c/d which is a period of $\approx$ 22.0 hours. The

phased light curve does not have the distinctive sawtooth shape. This may be because the observations missed the maximum of the variations. This variable may not be an RR Lyrae and additional observations are required. There is no F336W magnitude because the F336W image does not cover about 25% of the F140LP field of view, and **FUV7** is in the missing region.

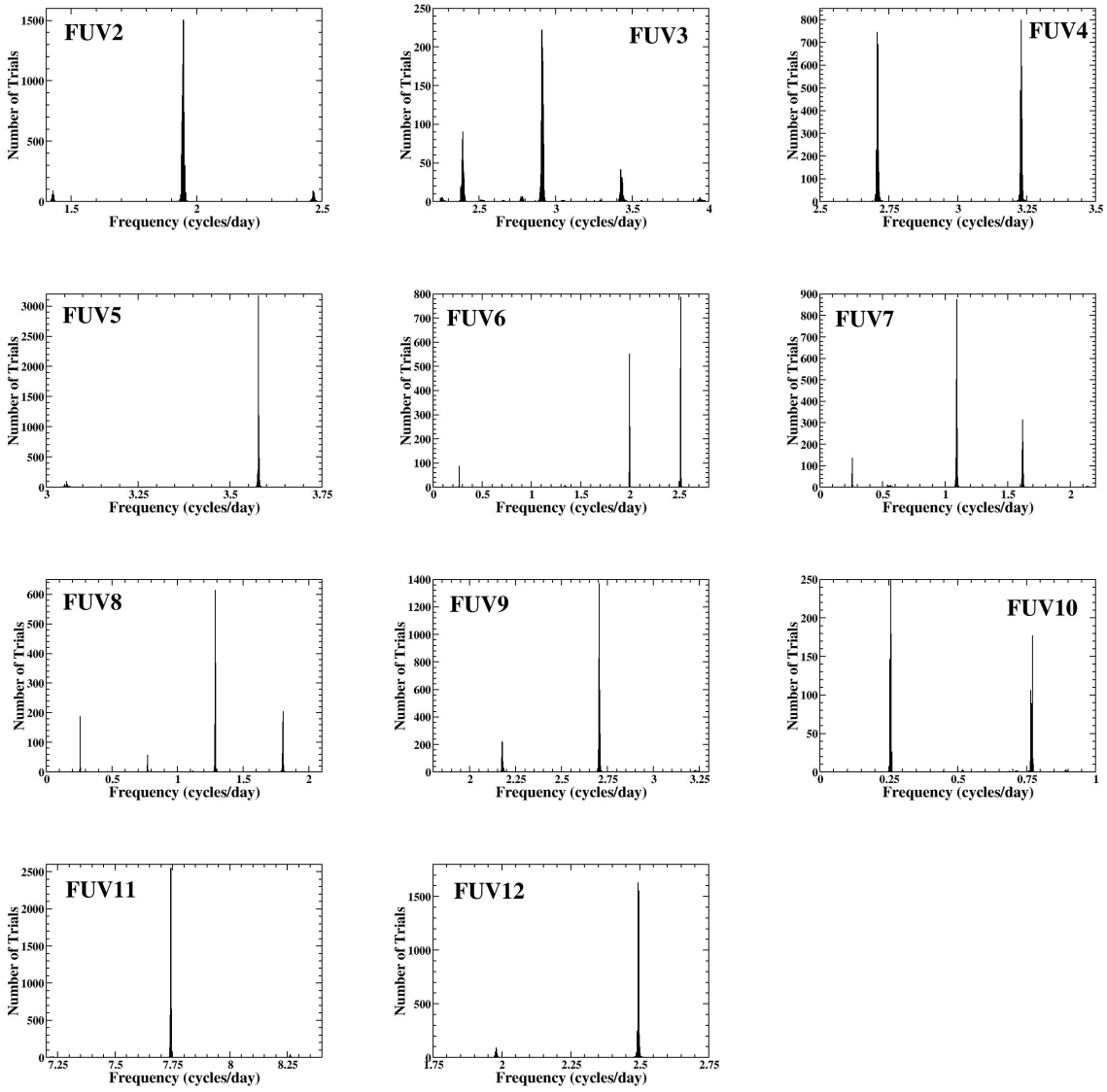

FIGURE 5.6: The results of the bootstrap analysis for each variable. The frequency associated with the peak power from each trial is plotted as a histogram. The bin width of the histogram is 0.001 in frequency. Each of the plots are labeled from the top left (FUV2) to the middle bottom (FUV12).

FUV8, third row of Figure 5.4, has a number of peaks above the 99.9% level in the power spectrum with the largest peak corresponding to a period of $\approx$ 18.6 hours. The bootstrap trials (Figure 5.6) produced a number of peaks with the largest peak having $\sim$ 3270 trials associated with it and a frequency of 1.2862 c/d. This corresponds to a period of $\approx$ 18.6 hours. The light curve phased to this period has a distinctive sawtooth

shape (Figure 5.4), suggesting that it is a pulsation variable (i.e. RR Lyrae). There is no F336W magnitude because the F336W image does not cover about 25% of the F140LP field of view, and **FUV8** is in the missing region.

FUV9, fourth (or bottom) row of Figure 5.4, has a number of peaks above the 99.9% level in the power spectrum with the largest peak corresponding to a period of $\approx$ 8.9 hours. The bootstrap trials (Figure 5.6) produced a number of peaks with the largest peak having $\sim$ 7950 trials at a frequency of 2.7047 c/d. This corresponds to a period of $\approx$ 8.9 hours. The light curve phased to this period has a distinctive sawtooth shape (Figure 5.4), suggesting it is a pulsation variable (i.e. RR Lyrae). There appears to be a pause in the phased light curve on the left side of the peak (Figure 5.4). This may be the result of multi-mode pulsations. However, additional observations are required to confirm this as the reason for the shape of the light curve.

FUV10, first (or top) row of Figure 5.5, has a number of peaks above the 99.9% level in the power spectrum with the largest peak corresponding to a period of $\approx$ 3.9 days (or $\approx$ 93.6 hours). The bootstrap trials (Figure 5.6) produced a number of peaks with the largest peak at a frequency of 0.2562 c/d (i.e. $\approx$ 3.9 days). The position of this peak in the bootstrap trials is a common result among many of the bootstrap trials for all the variable candidates. In this case the peak has more than 5250 trials in it, which is an order of magnitude more than for other variable candidates. A secondary peak with $\sim$ 950 trials (about 5$\times$ fewer trials) can be seen at a frequency of 0.7712 c/d which corresponds to a period of $\approx$ 1.3 days. I phased the observations to the period $\approx$ 3.9 days which results in the light curve in Figure 5.5. This light curve does not have the distinctive sawtooth shape of a RR Lyrae and in fact this period is longer than typical RR Lyrae, which have periods less than $\sim$ 24 hours (e.g. Braga et al. 2016). This object requires and deserves additional scrutiny to confirm its period and determine its nature.

FUV11, second (or middle) row of Figure 5.5, has a number of peaks above the 99.9% level in the power spectrum with the largest peak corresponding to a period of $\approx$ 3.1 hours. The bootstrap trials (Figure 5.6) produced a peak with $\sim$ 9280 trials and a frequency of 7.7426 c/d (i.e. $\approx$ 3.1 hours). The phased light curve (Figure 5.5) does not have the distinctive sawtooth shape seen in other RR Lyrae as the rise and decline times seem equal. The amplitude of variation is about 1.5 magnitudes and is the shortest period variable among the suspected RR Lyrae. Additional observations are needed to further characterize this system.

FUV12, third (or bottom) row of Figure 5.5, has a number of peaks above the 99.9% level in the power spectrum with the largest peak corresponding to a period of $\approx$ 9.6 hours. The bootstrap trials (Figure 5.6) produced a peak with $\sim$ 9200 trials in it with a frequency of 2.4936 c/d (i.e. $\approx$ 9.6 hours). The phased light curve has a distinctive sawtooth shape (Figure 5.5), suggesting it is a pulsation variable (i.e. RR Lyrae). The amplitude is nearly 5 magnitudes, making it the largest amplitude variable among the

suspected RR Lyrae. Interestingly, the optical colour of this variable places it redward of the red giant branch (Figure 5.2), though its position in the ultraviolet CMD is similar to the other RR Lyrae. It could be a red straggler as defined by Geller et al (2017). This object deserves additional scrutiny to confirm its status as a red straggler.

I have identified 12 variables which are in the expected location of RR Lyrae in the ultraviolet colour magnitude diagram (Figure 5.2). There are two particularly interesting variables in this sample (Table 5.1). **FUV2** and **FUV12** stand out because their optical colours and magnitudes place them in locations not normally associated with RR Lyrae. **FUV2** is more than a magnitude brighter than the next brightest variable in this sample (Table 5.1). This places it in a location associated with the asymptotic giant branch, which leads us to the possibility that this is an evolved horizontal branch star that is within the RR Lyrae instability strip. **FUV12** has a magnitude similar to the other RR Lyrae, but its optical colour places it to the red of the red giant branch (Figure 5.2). This could be a member of the "Red straggler" class of objects (Geller et al 2017) though the saw tooth shape of its variability would seem to indicate that it is an RR Lyrae. The surprising aspect here is that the optical colour of the source places it well outside the classical instability strip. The rest of the candidate RR Lyrae variables seem to behave as expected.

5.3.2 Blue stragglers and white dwarf binaries

There are 11 possible variables which have colours and magnitudes that place them among the blue stragglers and/or blueward of the main sequence in the ultraviolet colour magnitude diagram (Figure 5.2). In the optical a number of these sources are on the main sequence (Figure 5.2), indicating that there may be at least two components to the system (i.e. a main sequence star and a hot star, such as a white dwarf). In Figure 5.7, Figure 5.8, and, Figure 5.9, I present the observations, the power spectrum, and, phased light curve for each of the variables in Table 5.2. The period corresponding to the highest peak in the power spectrum is also presented in Table 5.2 and was used in constructing the phased plots in Figure 5.7, Figure 5.8, and, Figure 5.9. Depending on their location in the CMD, these systems may be pulsating variables, known as SX Phoenicis variables, or some sort of binary. I discuss each of the systems in Table 5.2 below and provide the most likely interpretation for each.

FUV13, first (or top) row of Figure 5.7, has two peaks above the 99.9% level in the power spectrum with the largest peak corresponding to a period of $\approx$ 11.1 hours. The bootstrap trials (Figure 5.10) produced a number of peaks. The largest peak has $\sim$ 940 trials at a frequency of 2.939 c/d, the next two largest peaks (Figure 5.10) are at frequencies of 2.6795 c/d ($\sim$ 825 trials) and 2.1536 c/d ($\sim$ 475 trials). I consider the period to be uncertain but have nevertheless phased the data on the period corresponding to the highest peak in the power spectrum, $\approx$ 11.1 hours. The resulting light curve (Figure 5.7)

Name	RA (J2000) (hh:mm:ss.s)	DEC (J2000) (dd:mm:ss.s)	Period (hours)	F140LP (STmag)	F336W (STmag)	F606W (STmag)	F814W (STmag)
FUV13	5:14:05.934	-40:02:44.976	11.1*	21.83	18.54	16.81	17.74
FUV14	5:14:05.850	-40:02:43.164	1.82(±0.001)	20.75	18.41	17.87	17.45
FUV15	5:14:06.279	-40:02:36.504	8.2*	21.09	18.92	18.31	18.00
FUV16	5:14:06.663	-40:02:47.109	5.0*	19.69	18.21	17.46	17.34
FUV17	5:14:06.560	-40:02:44.746	21.4(±0.15)	19.64	18.61	18.31	18.23
FUV18	5:14:07.140	-40:02:39.762	18.8(±0.61)	17.49	19.60	18.99	18.44
FUV19	5:14:04.994	-40:02:49.712	1.9(±0.003)	18.99		20.23	19.68
FUV20	5:14:06.195	-40:02:43.928	7.0(±0.017)	22.86	19.59	18.99	18.39
FUV21	5:14:06.563	-40:02:47.645	7.4(±0.019)	22.55	19.84	18.96	18.43
FUV22	5:14:06.287	-40:02:47.797	8.8(±0.07)	23.94	19.79	19.68	19.02
FUV23	5:14:05.961	-40:02:47.593	0.07*	21.76	19.98	19.36	18.94

TABLE 5.2: The candidate blue straggler and white dwarf variables found in this study. The periods correspond to the peak with the most power in the power spectrum (see Figure 5.7, Figure 5.8, and, Figure 5.9). The value in the brackets after the period is derived from the bootstrap trials (Chapter 5.10) as $3 \times \sigma$ of the peak. The * on several of the periods indicates the period is uncertain as explained in the text. The magnitudes are on the space telescope magnitude system. The variable candidates without a F336W magnitude are in a region of the field of view in that is not covered by the F336W image. The positions are calculated using the world coordinate system associated with the combined drizzled image of all the ACS/SBC images.

has an amplitude of about 0.5 magnitudes. This system is the bluest red circle in the optical colour magnitude diagram (Figure 5.2) and is among the blue stragglers in the ultraviolet colour magnitude diagram (Figure 5.2). This blue straggler would seem to be a very massive given its optical properties, but a relatively normal blue straggler from its ultraviolet properties. The peculiar properties of this variable deserve further study with additional observations.

FUV14, second row of Figure 5.7, has a number of peaks above the 99.9% level in the power spectrum with the largest peak corresponding to a period of $\approx$ 109.1 minutes. The bootstrap trials (Figure 5.10) produced a peak with $\sim$ 6900 trials at the frequency 13.197 c/d which corresponds to the $\approx$ 109.1 minute period. The phased light curve (Figure 5.7) has a maximum amplitude of about 3 magnitudes, though there appears to be multiple peaks. There is no improvement when the observations are phased on other peaks in the power spectrum. Additional time-series observations are required to confirm this behavior and determine a possible explanation.

FUV15, third row of Figure 5.7, has a number of peaks above the 99.9% level in the power spectrum with the largest peak corresponding to a period of $\approx$ 8.2 hours. The only significant peak in the bootstrap trials is at a frequency of 0.2569 c/d with $\sim$ 225 trials. I phased the observations to the $\approx$ 8.2 hour period (Figure 5.7) from the power spectrum, though, the bootstrap trials would indicate that the period is uncertain. The amplitude of variation is about 0.5 magnitudes. The colours and magnitudes of this source seem to imply a "normal" blue straggler star in both colour magnitude diagrams (Figure 5.2). However, the period of $\approx$ 8.2 hours is long for SX Phe pulsations. An alternative possibility is that this object may be a binary. Further study of this variable

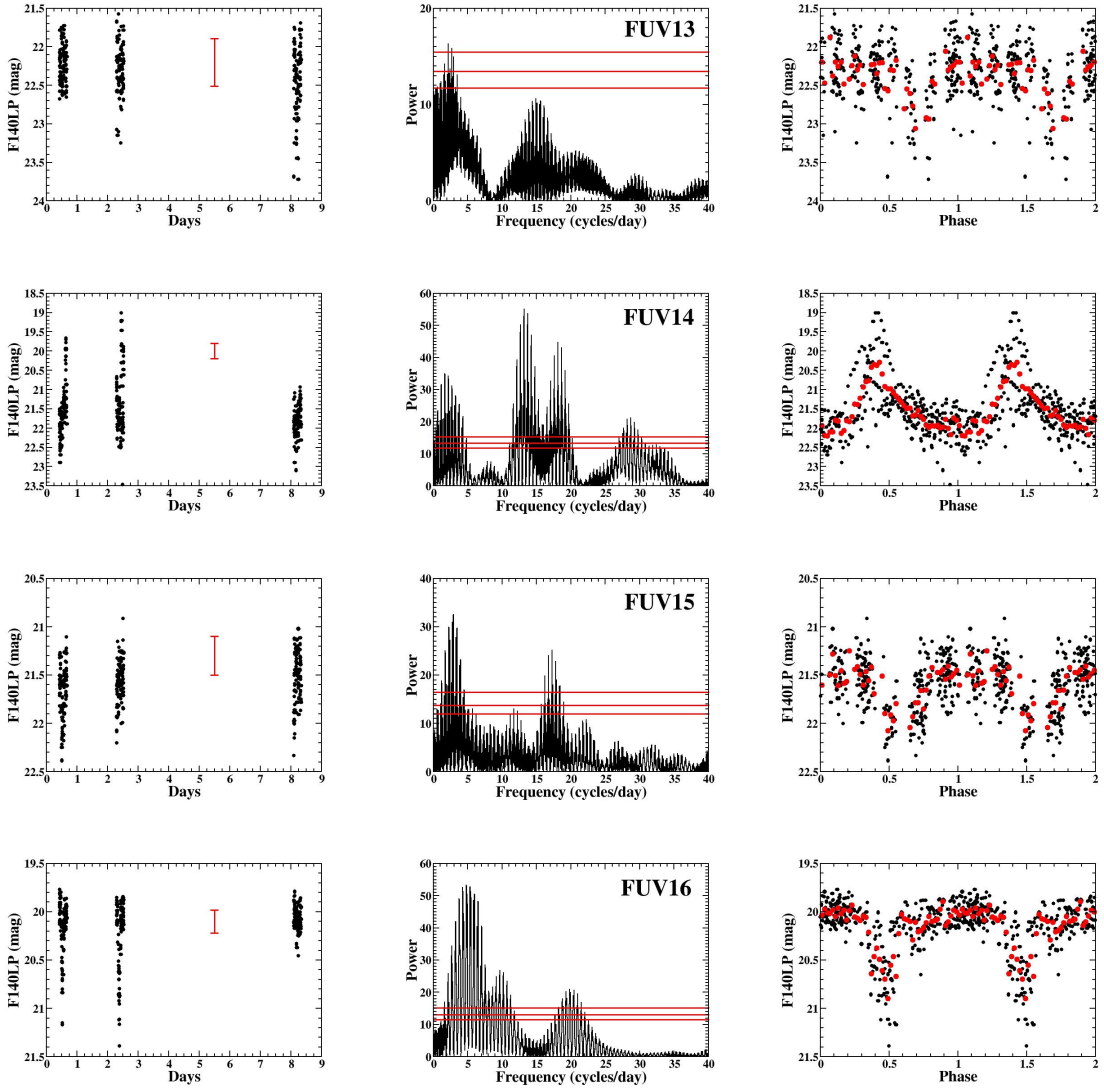

FIGURE 5.7: Each row is for a variable candidate (**FUV13**, **FUV14**, **FUV15**, and, **FUV16**) labeled on the left. The left most column of figures is the photometry for the variable as a function of the time of the observation. Note the distinctive pattern of the three visits. The red bar at 5.5 days (between visits 2 and 3) has a length 2× the mean photometric error. The middle column is the power spectrum of the observations with the power on the y-axis and frequency (cycles/day) on the x-axis. The more likely frequencies have the most power. The right most column is the observations phased on the best frequency from the middle panel. The red dots are the mean magnitude for each 0.02 of phase. Each of these variable candidates is discussed in the text.

would be useful in understanding the properties of this system and blue stragglers in general.

FUV16, fourth (or bottom) row of Figure 5.7, has a number of peaks above the 99.9% level in the power spectrum with the largest peak corresponding to a period of $\approx$ 5.0 hours. The only significant peak in the bootstrap trials is at a frequency of 0.2615 c/d with $\sim$ 200 trials. I phased the observations to the $\approx$ 5.0 hour period (Figure 5.7)

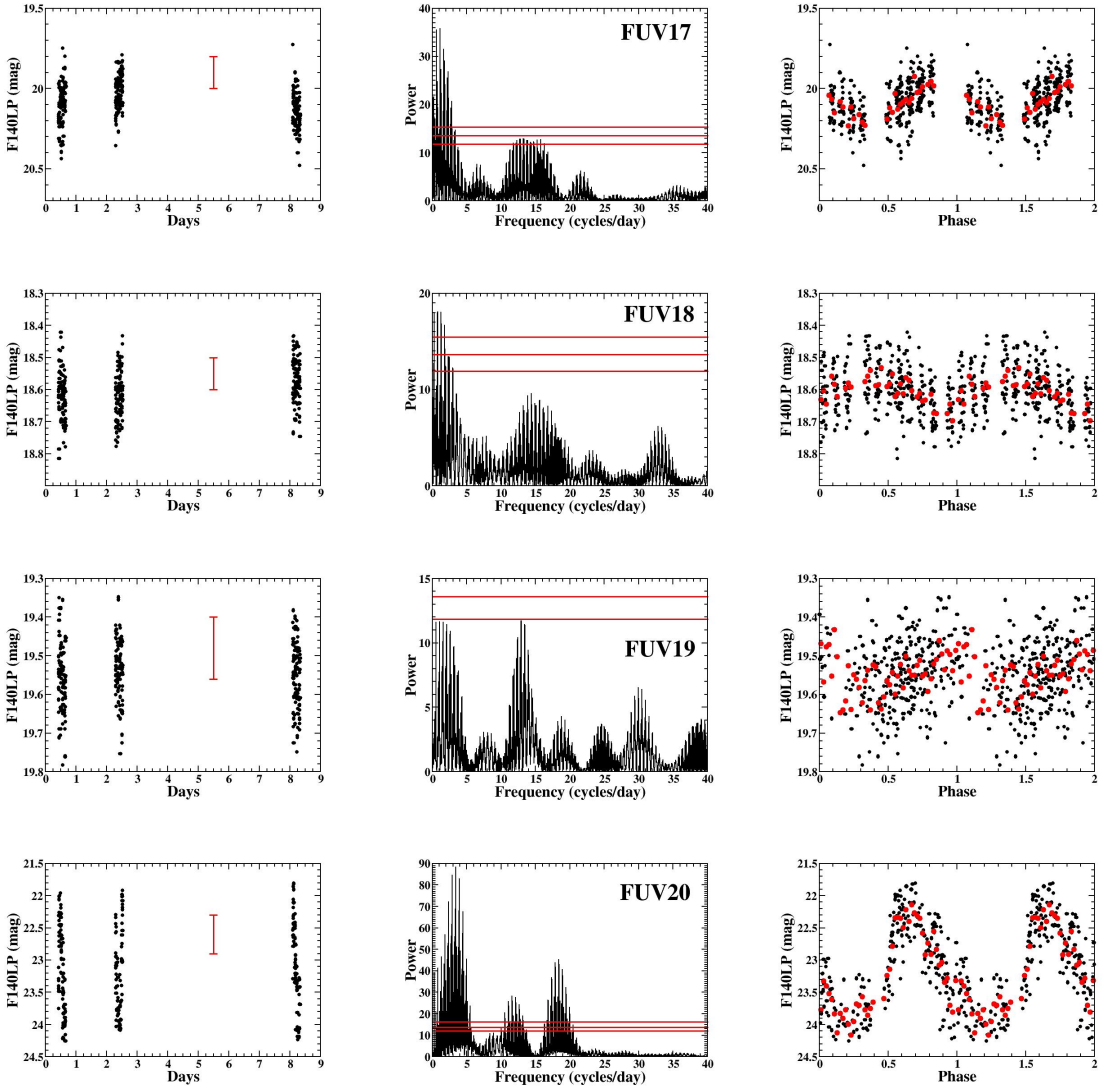

FIGURE 5.8: Each row is for a variable candidate (**FUV17**, **FUV18**, **FUV19**, and, **FUV20**) labeled on the left. The left most column of figures is the photometry for the variable as a function of the time of the observation. Note the distinctive pattern of the three visits. The red bar at 5.5 days (between visits 2 and 3) has a length 2× the mean photometric error. The middle column is the power spectrum of the observations with the power on the y-axis and frequency (cycles/day) on the x-axis. The more likely frequencies have the most power. The right most column is the observations phased on the best frequency from the middle panel. The red dots are the mean magnitude for each 0.02 of phase. Each of these variable candidates is discussed in the text.

from the power spectrum, though the bootstrap trials would indicate that the period is uncertain. The observations have a variation with an amplitude of about a magnitude (Figure 5.7). The colours and magnitudes of this source seem to imply a "normal" blue straggler star in both colour magnitude diagrams (Figure 5.2). The cause of the variation is unknown and additional study would be useful in determining the properties of this system.

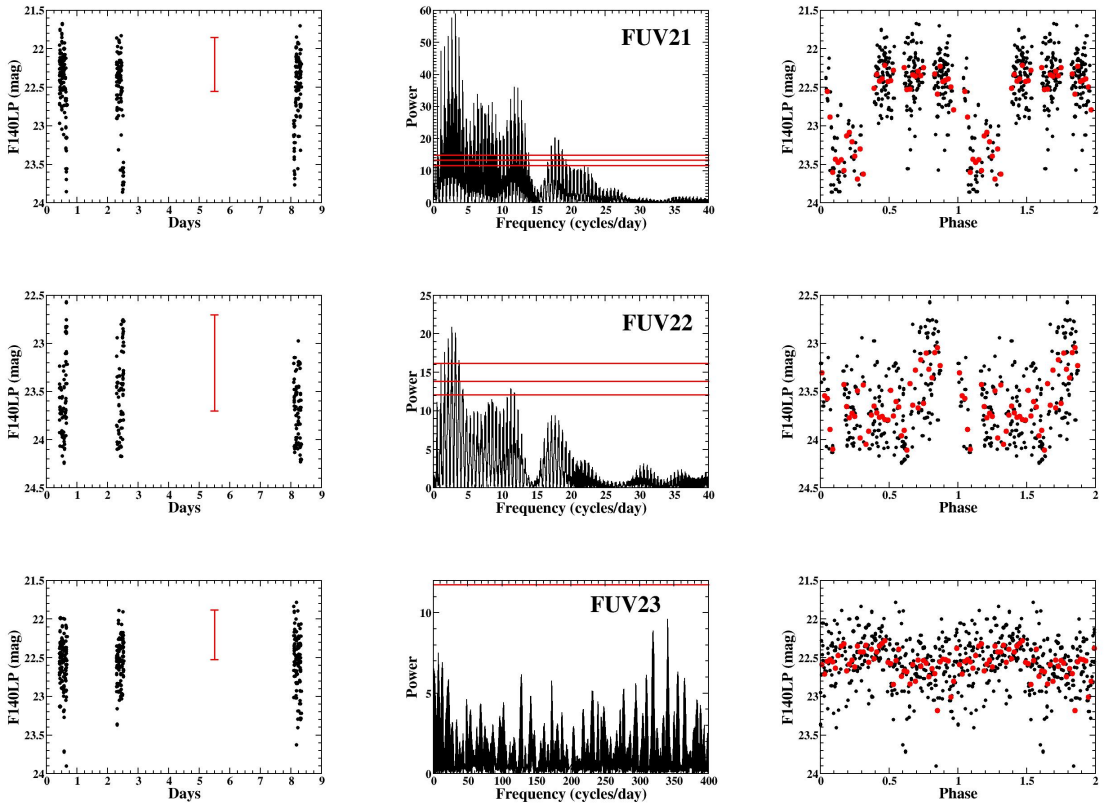

FIGURE 5.9: Each row is for a variable candidate (**FUV21**, **FUV22**, and, **FUV23**) labeled on the left. The left most column of figures is the photometry for the variable as a function of the time of the observation. Note the distinctive pattern of the three visits. The red bar at 5.5 days (between visits 2 and 3) has a length 2× the mean photometric error. The middle column is the power spectrum of the observations with the power on the y-axis and frequency (cycles/day) on the x-axis. The more likely frequencies have the most power. The right most column is the observations phased on the best frequency from the middle panel. The red dots are the mean magnitude for each 0.02 of phase. Each of these variable candidates is discussed in the text.

FUV17, first (or top) row of Figure 5.8, has a number of peaks above the 99.9% level in the power spectrum with the largest peak corresponding to a period of $\approx$ 21.4 hours. There are a number of peaks in the bootstrap trials (Figure 5.10) with the highest peak, $\sim$ 4800 trials, with a frequency of 1.1202 c/d which corresponds to a period of $\approx$ 21.4 hours. The phased light curve has an amplitude of $\sim$ 0.3 magnitudes (Figure 5.8). The colours and magnitudes of this source imply that it is a "normal" blue straggler in both colour magnitude diagrams (Figure 5.2).

FUV18, second row of Figure 5.8, has a number of peaks above the 99.9% level in the power spectrum with the largest peak corresponding to a period of $\approx$ 18.8 hours. The bootstrap trials (Figure 5.10) have a number of peaks. The largest peaks has a frequency of 1.2725 c/d and $\sim$ 1700 trials. There are two additional peaks with a comparable number of trials associated with them and they are at the frequencies of 0.7658 c/d ($\sim$ 1460 trials) and 0.257 c/d ($\sim$ 1500 trials). The number of trials associated with

these three peaks indicates that the period should be considered as uncertain.I phased observations to a period corresponding to the peak in the power spectrum, $\approx$ 18.8 hours, which shows an amplitude of $\sim$ 0.1 magnitudes (Figure 5.8). The optical colours and magnitudes place this source on the main sequence (Figure 5.2) while in the ultraviolet this source is the bluest object in the ultraviolet CMD (Figure 5.2). The implication is that there is a hot component as part of this source. This is likely a main sequence star with a hot white dwarf companion. The $\approx$ 18.8 hour period, if correct, is on the long side for cataclysmic variables, and additional data – e.g. evidence for emission lines – will be needed to confirm or reject the possibility that it is a CV.

FUV19, third row of Figure 5.8, has a number of peaks near the 95% level in the power spectrum with the largest peak corresponding to a period of $\approx$ 1.9 hours or $\approx$ 114 minutes. The two largest peaks in the bootstrap trials have only $\sim$ 200 trials associated with them. The low number of trials, $\sim$ 200 out of 10000, indicates that the period is uncertain. The peak power in the power spectrum is on the low side, but I decided to include this source for completeness. This object is the faintest red circle that is on the main sequence in the optical colour magnitude diagram (Figure 5.2). Unfortunately, no F336W magnitude is available for this source, as it is located in the $\sim$ 25% of the far ultraviolet field of view not covered by the F336W image. The F140LP magnitude and possible period would seem to imply a compact binary with a hot component. However, additional observations are needed to confirm the period and characterize this source. Note that a period of $\approx$ 114 minutes would be typical for a short-period CV.

FUV20, fourth (or bottom) row of Figure 5.8, has a number of peaks above the 99.9% level in the power spectrum with the largest peak corresponding to a period of $\approx$ 7.0 hours. The main peak in the bootstrap trials (Figure 5.10) has $\sim$ 9100 trials and a frequency of 3.407 c/d (i.e. $\approx$ 7.0 hours). The phased light curve has a distinctive sawtooth shape (Figure 5.8) with an amplitude of about 2 magnitudes. The optical colours and magnitude imply this source is on the main sequence in the optical (Figure 5.2) and in the ultraviolet it is located to the blue of the turn off. This is likely a SX Phoenicis star though the magnitudes, both optical and far-ultraviolet, are low for this class of stars at the distance of the cluster. Additional observations would be useful in confirming the brightness and further characterizing this system.

FUV21, first (or top) row of Figure 5.9, has a number of peaks above the 99.9% level in the power spectrum with the largest peak corresponding to a period of $\approx$ 7.4 hours. The most significant peak in the bootstrap trials (Figure 5.10) has $\sim$ 7200 trials at a frequency of 3.2338 c/d (i.e. $\approx$ 7.4 hours). The phased light curve (Figure 5.9) has an amplitude of $\sim$ 1.2 magnitudes. The optical colours and magnitudes of this source place it on the main sequence (Figure 5.2). The ultraviolet colour and magnitudes place it at about the brightness of the turnoff, but to the blue (Figure 5.2). These colours and magnitudes suggest that this variable is composed of a main sequence star and a hot

star. The period is consistent with that of cataclysmic variables, though emission lines in a spectrum are required to confirm this interpretation.

FUV22, second (or middle) row of Figure 5.9, has a number of peaks above the 99.9% level in the power spectrum with the largest peak corresponding to a period of $\approx$ 8.8 hours. The largest peak in the bootstrap trials (Figure 5.10) has $\sim$ 1000 trials at a frequency of 2.7160 c/d (i.e. $\approx$ 8.84 hours). The observations have been phased to the period $\approx$ 8.8 hours (Figure 5.9) and it has an amplitude of $\sim$ 0.7 magnitudes. The optical colours and magnitudes of this source place it on the main sequence (Figure 5.2). The ultraviolet colour and magnitudes place it at about the brightness of the turnoff but just to the blue of the turn off (Figure 5.2). These colours and magnitudes suggest that this variable is composed of a main sequence star and a hot star. The period is consistent with that of cataclysmic variables though emission lines in a spectrum are required to confirm this interpretation.

FUV23, third (or bottom) row of Figure 5.9, has no peaks above the 95% level in the power spectrum. The largest peak corresponds to a period of $\approx$ 4.2 minutes. The only significant peak in the bootstrap trials (Figure 5.10) corresponds to the frequency of 0.2615 with $\sim$ 280 trials. The amplitude of any variation is too low for the signal-to-noise of the data to determine any significant variation in this source. The observations have been phased on the $\approx$ 4.2 minute period though the significance of this period can not be shown. The colours and magnitudes of this source, similar to the systems above, is on the main sequence in the optical and to the blue of the turn off in the ultraviolet (Figure 5.2). The period associated with the peak of the power spectrum corresponds to a very short period; if this is real it would be the shortest period system found. However, it is more likely that if this star is a variable the period remains unknown. A higher signal to noise time series will be required to test if this candidate variable is really a (periodic) variable. A spectrum showing emission lines would also confirm this system as a semi-detached binary.

There are 11 variable candidates which can be classified as either a blue straggler or a white dwarf plus main sequence binary. Based on the magnitudes and colours of these candidates five are in the traditional blue straggler region and six are on the main sequence in the optical but to the blue of the main sequence in the ultraviolet.

There are two systems, **FUV14** and **FUV20**, which have the appearance of a pulsating variable (like the RR Lyrae), though their photometric properties and light curves make them quite interesting. **FUV14** does not seem to phase cleanly onto a single period across the different epochs/visits. The first thought is that this is a SX Phoenicis type of pulsating variable. The shifting peak and amplitude could mean that this system has multiple modes in its pulsations. Clearly, this variable requires further study to determine what is the cause of its light curve.

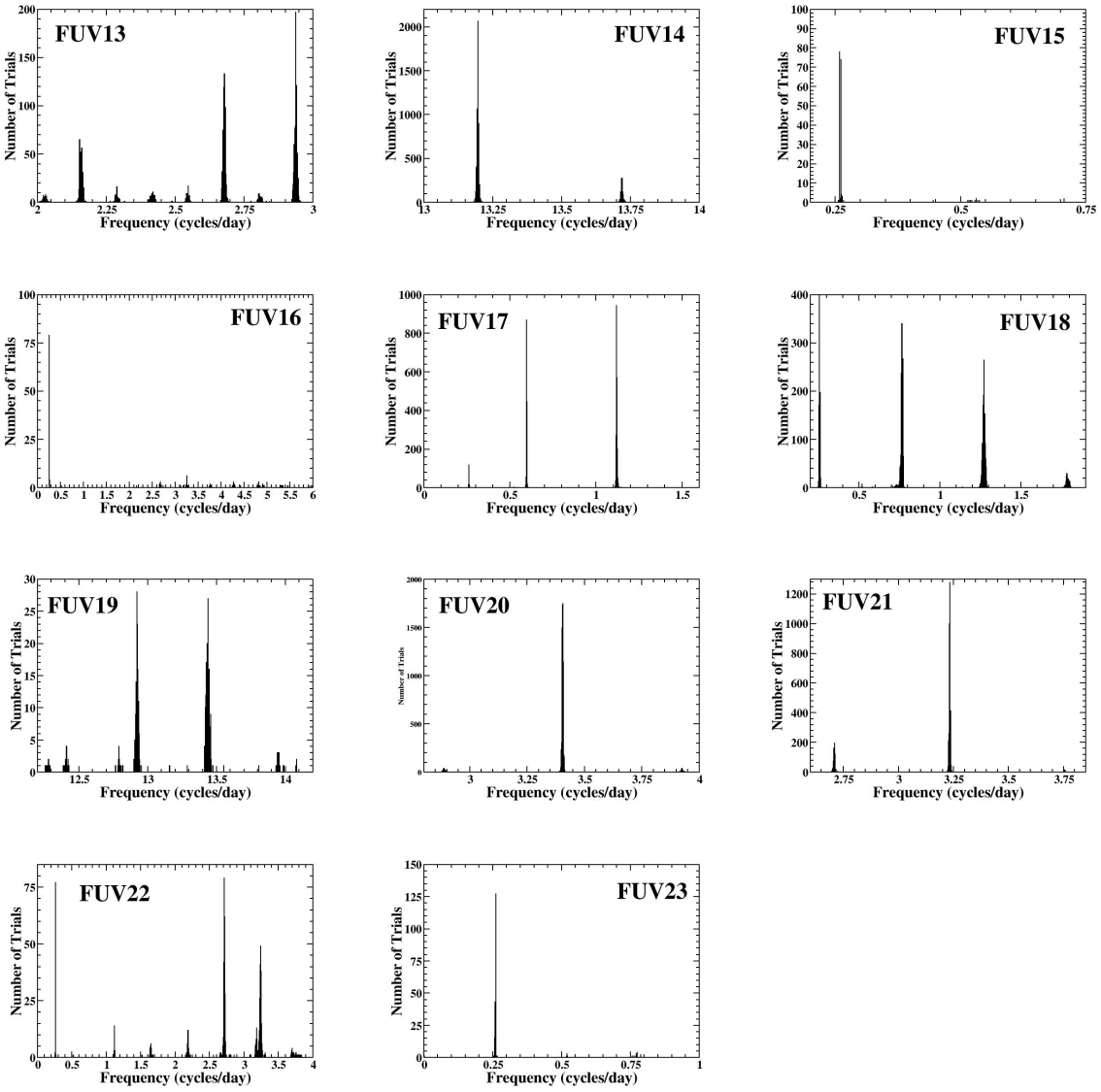

FIGURE 5.10: The results of the bootstrap analysis for each variable. The frequency associated with the peak power from each trial is plotted as a histogram. The bin width of the histogram is 0.001 in frequency. Each of the plots are labeled from the top left (FUV13) to the middle bottom (FUV23).

The other system, **FUV20**, has the distinctive saw tooth shape of a pulsating variable (like is seen among the RR Lyrae above). The photometric properties in the optical place this variable candidate on the main sequence though in the ultraviolet it is blue of the main sequence. If this variable candidate is composed of multiple components (for example a main sequence star and a white dwarf), it implies that the blue or hot component is pulsating. Its magnitude is not typical for a SX Phoenicis in that is too faint. A possibility (conjecture) is that the hot component could be a Helium white dwarf and that *it* is pulsating (analogous to ZZ Ceti variables).

The rest of the variable candidates have the appearance of being binaries with dips in

the light curves, perhaps corresponding to phases where some of the light of the hot component is eclipsed. Though this may not be the solution for all of them, it does have the advantage of explaining both the variability and the photometric properties. Future spectroscopic observations for radial velocities or emission lines will be needed to determine the nature of the stellar components and whether the binaries are detached, semi-detached, or, contact systems.

5.3.3 Blue Horizontal Branch

The blue end of the horizontal branch is composed of hot stars which have a low mass atmosphere. The hottest ($> 30,000$K) of these stars are known as subdwarf O stars, and the slightly cooler ones as subdwarf B stars. In the Galactic field, these systems are often found in binary systems ($\sim 50\%$ binary frequency; Copperwheat et al. 2011). However, very few binaries have been found among the equivalent stars in globular clusters (Moni Bidin et al. 2011). This is likely linked to the different conditions in GC relative to the field, such as the lower metallicity and/or higher stellar densities (which might destroy wide binaries producing sdBs in the field).

Recent studies of field subdwarf O & B stars have found them to be varying in a similar manner to that of ZZ Ceti stars (see above). The surveyed subdwarf O stars have been found to have periods less than $\sim$ 45 minutes (Randall et al. 2016). The surveyed subdwarf B stars have periods less than $\sim$ 12 hours (Ostensen et al. 2012). Only a few of these pulsating variables have not been found in globular clusters (Brown et al. 2013). This is likely because of the large distances to globular clusters and because all variability studies, other than this one, have been in the optical. This is not optimal, since that is not where these sources emit most of their light. In the far ultraviolet, the signal-to-noise with which the blue horizontal branch stars are detected is large (S/N$\sim$ 50), even in a single 90 second exposure.

FUV24, first (or top) row of Figure 5.11, has a number of peaks above the 99.9% level in the power spectrum with the largest peak corresponding to a period of $\approx$ 10.8 hours. The largest peak in the bootstrap trials (Figure 5.15) has $\sim$ 3300 trials at a frequency of 2.213 c/d (i.e. $\approx$ 10.8 hours). There is no clear minimum (or maximum) seen in the phased light curve (Figure 5.11) but there is $\sim$ 0.05 magnitudes of variation. Each epoch/visit has a very similar slope of decline. This source has no F336W magnitude (Table 5.3), and therefore it is not plotted on the ultraviolet colour magnitude diagram, though it is clearly on the blue horizontal branch in the optical colour magnitude diagram (Figure 5.2).

FUV25, second row of Figure 5.11, has a number of peaks above the 99.9% level in the power spectrum with the largest peak corresponding to a period of $\approx$ 1.8 days. The largest peak in the bootstrap trials (Figure 5.15) has $\sim$ 1100 trials at a frequency

Name	RA (J2000) (hh:mm:ss.s)	DEC (J2000) (dd:mm:ss.s)	Period (hours)	F140LP (STmag)	F336W (STmag)	F606W (STmag)	F814W (STmag)
FUV24	5:14:05.006	-40:02:49.932	11.8(±0.08)	15.99		16.96	17.00
FUV25	5:14:07.127	-40:02:39.615	43.2(±1.0)	15.94	16.77	16.93	16.93
FUV26	5:14:06.547	-40:02:35.416	72.0(±3.0)	16.83	16.71	16.19	16.10
FUV27	5:14:05.904	-40:02:37.690	19.7(±0.13)	15.92	16.72	16.76	16.76
FUV28	5:14:06.864	-40:02:30.745	40.8(±0.33)	16.00	16.66	16.96	16.98
FUV29	5:14:04.983	-40:02:39.105	1.75*	15.91	16.78	16.70	16.70
FUV30	5:14:05.730	-40:02:34.564	1.63(±0.002)	16.38	16.37	15.85	15.78
FUV31	5:14:06.222	-40:02:31.835	8.9(±0.06)	16.32	16.72	16.40	16.37
FUV32	5:14:04.439	-40:02:29.134	36.0(±0.65)	16.53		16.31	16.25
FUV33	5:14:04.828	-40:02:26.379	2.2*	16.02		16.25	16.23
FUV34	5:14:04.394	-40:02:25.849	20.4(±0.21)	16.07		16.65	16.64
FUV35	5:14:05.058	-40:02:20.032	20.2(±0.24)	16.58		16.31	16.24
FUV36	5:14:06.894	-40:02:47.327	2.0*	16.62	16.51	16.06	15.98

TABLE 5.3: The candidate blue horizontal branch variables found in this study. The periods correspond to the peak with the most power in the power spectrum (see Figure 5.11, Figure 5.12, and, Figure 5.13). The value in the brackets after the period is derived from the bootstrap trials (Chapter 5.10) as $3 \times \sigma$ of the peak. The * on several of the periods indicate the period is uncertain as explained in the text. The magnitudes are on the space telescope magnitude system. The variable candidates without a F336W magnitude are in a region of the field of view in that is not covered by the F336W image. The positions are calculated using the world coordinate system associated with the combined drizzled image of all the ACS/SBC images.

of 0.544 c/d (i.e. $\approx$ 1.8 days). A variation with an amplitude of $\sim$ 0.03 magnitudes is apparent in the phased light curve. No clear maximum or minimum is detected in the data (Figure 5.11). The reality of the variation of this star will require additional observations to confirm.

FUV26, third row of Figure 5.11, has a number of peaks above the 99% level in the power spectrum with the largest peak corresponding to a period of $\approx$ 3.0 days. The largest peak in the bootstrap trials (Figure 5.15) has $\sim$ 1500 trials at a frequency of 0.330 c/d (i.e. $\approx$ 3.0 days). The phased light curve has an amplitude of $\sim$ 0.04 magnitudes though no clear maximum or minimum is apparent (Figure 5.11). The reality of the variation of this star will require additional observations to confirm.

FUV27, fourth (or bottom) row of Figure 5.11, has several peaks above the 99.9% level in the power spectrum with the largest peak corresponding to a period of $\approx$ 19.7 hours. There are several peaks with a similar number of trials associated with them in the bootstrap trials (Figure 5.15), though, the largest has $\sim$ 1300 trials at a frequency of 1.2133 c/d (i.e. $\approx$ 19.7 hours). There are three additional peaks in bootstrap trials that correspond to frequencies of 1.7366 c/d ($\sim$ 1250 trials), 0.5890 c/d ($\sim$ 650 trials), and 0.2615 c/d ($\sim$ 300 trials). The number of trials associated with these peaks indicates that the period should be considered to be uncertain. I phased the observations to the period corresponding to the peak in the power spectrum. The light curve has an amplitude of $\sim$ 0.05 magnitudes (Figure 5.11). This variation and associated periodicity require additional observations to confirm.

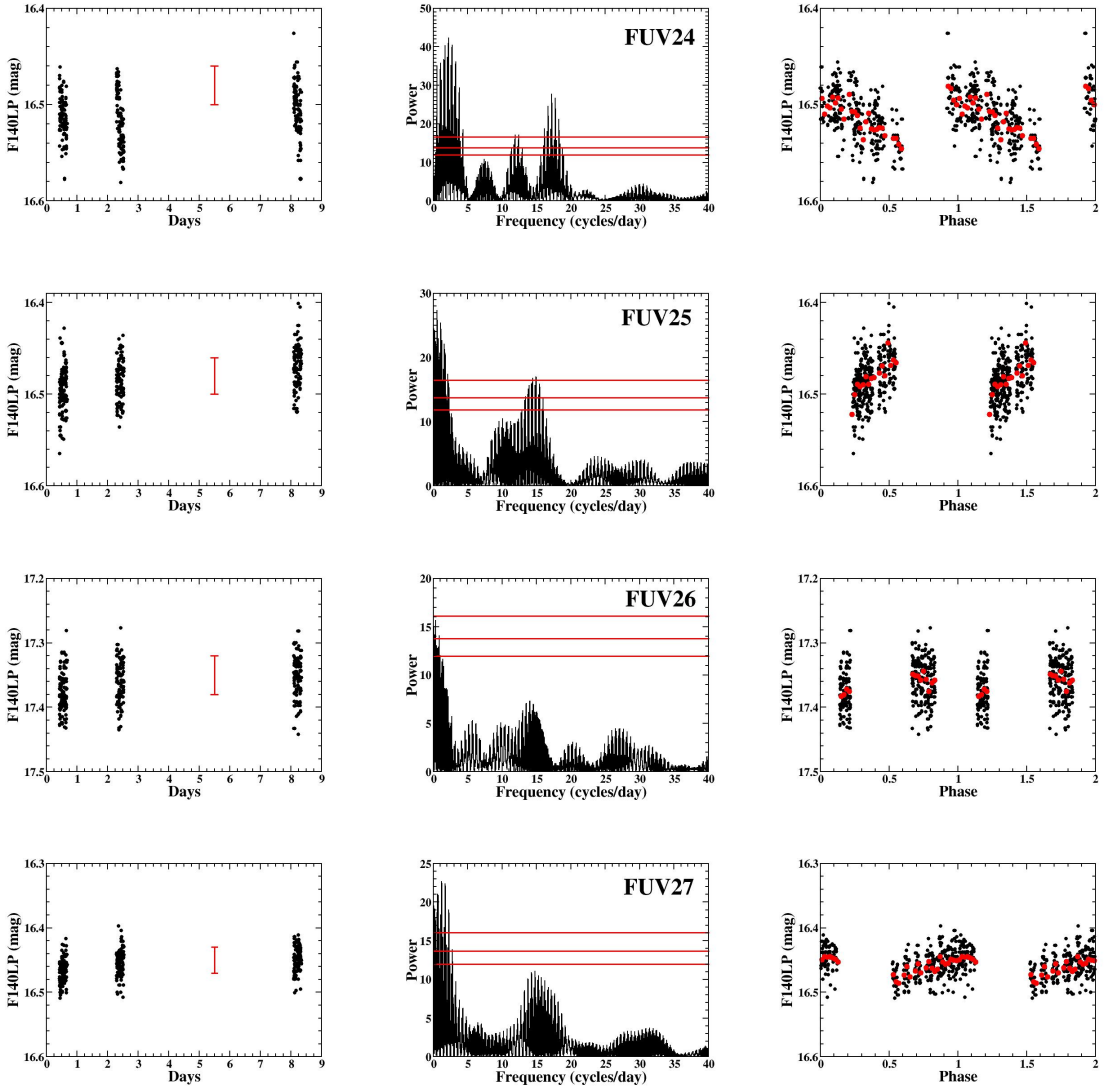

FIGURE 5.11: Each row is for a variable candidate (**FUV24**, **FUV25**, **FUV26**, and, **FUV27**) labeled on the left. The left most column of figures is the photometry for the variable as a function of the time of the observation. Note the distinctive pattern of the three visits. The red bar at 5.5 days (between visits 2 and 3) has a length 2× the mean photometric error. The middle column is the power spectrum of the observations with the power on the y-axis and frequency (cycles/day) on the x-axis. The more likely frequencies have the most power. The right most column is the observations phased on the best frequency from the middle panel. The red dots are the mean magnitude for each 0.02 of phase. Each of these variable candidates is discussed in the text.

FUV28, first (or top) row of Figure 5.12, has several peaks above the 99.9% level in the power spectrum with the largest peak corresponding to a period of $\approx$ 1.7 days. The most significant peak with $\sim$ 3000 trials in the bootstrap tests (Figure 5.15) has a frequency of 0.5939 c/d (i.e. $\approx$ 1.7 days). The observations have been phased on the period corresponding to the peak in the power spectrum and has an amplitude of $\sim$ 0.04 magnitudes (Figure 5.12). A maximum or minimum can not be securely identified and thus additional observations are required to confirm the variation and period.

FUV29, second row of Figure 5.12, has two peaks above the 99% level in the power spectrum with the larger of the two corresponding to a period of $\approx$ 105 minutes. The only significant peak in the bootstrap trials (Figure 5.15) has $\sim$ 400 trials at a frequency of 0.2615 c/d. This frequency is a very common peak among all the variable candidates bootstrap trials and given the number of trials in this peak it would indicate that the period is uncertain. The observations have been phased on the period corresponding to the peak in the power spectrum and has an amplitude of $\sim$ 0.04 magnitudes (Figure 5.12). The observations may have several induced periods or aliases from the time between the start times for each exposure ($\approx$ 110 seconds), the time between the start of each orbit ($\approx$ 96 minutes) and the duration of the observing window within each orbit ($\sim$ 54 minutes). The period of $\approx$ 105 minutes does not correspond to any of these possible aliases. Additional analysis and observations are required to confirm or rule out this period.

FUV30, third row of Figure 5.12, has several peaks above the 99.9% level in the power spectrum with the largest peak corresponding to a period of $\approx$ 98 minutes. There are two significant peaks in the bootstrap trials (Figure 5.15) with the larger of the two having $\sim$ 2000 trials with a frequency of 14.7167 c/d (i.e. $\approx$ 98 minutes). The observations have been phased on this period (Figure 5.12) and has an amplitude of $\sim$ 0.05 magnitudes. The orbital period of the Hubble Space Telescope, 96 minutes, is possibly being aliased here. Additional analysis and observations are required to confirm or rule out this period.

FUV31, fourth (or bottom) row of Figure 5.12, has several peaks above the 99.9% level in the power spectrum with the largest peak corresponding to a period of $\approx$ 8.9 hours. There are a few peaks in the bootstrap trials (Figure 5.15) with the most significant having $\sim$ 1300 trials in the peak bin and a frequency of 3.2288 c/d ($\sim$ 7.4 hours). The second highest peak at $\sim$ 900 trials corresponds to the peak frequency in the power spectrum. I phased the observations to the period ($\sim$ 8.9 hours) associated with the peak of the power spectrum (Figure 5.12). The phased light curve seems to show a complete light curve with an amplitude of $\sim$ 0.03 magnitudes. Additional analysis and observations are required to confirm this period.

FUV32, first (or top) row of Figure 5.13, has several peaks above the 99.9% level in the power spectrum with the largest peak corresponding to a period of $\approx$ 36.0 hours. There are a couple of peaks in the bootstrap trials (Figure 5.15) and the highest peak has $\sim$ 3200 trials and a frequency of 0.6671 c/d ($\approx$ 36.0 hours). The observations have been phased to the $\approx$ 36.0 hour period (Figure 5.13). The light curve is incomplete but still has an amplitude of $\sim$ 0.05 magnitudes. Note that this source is in the region not covered by the F336W image and is not in the ultraviolet colour magnitude diagram (Figure 5.2). The reality of the variation of this star will require additional observations to confirm.

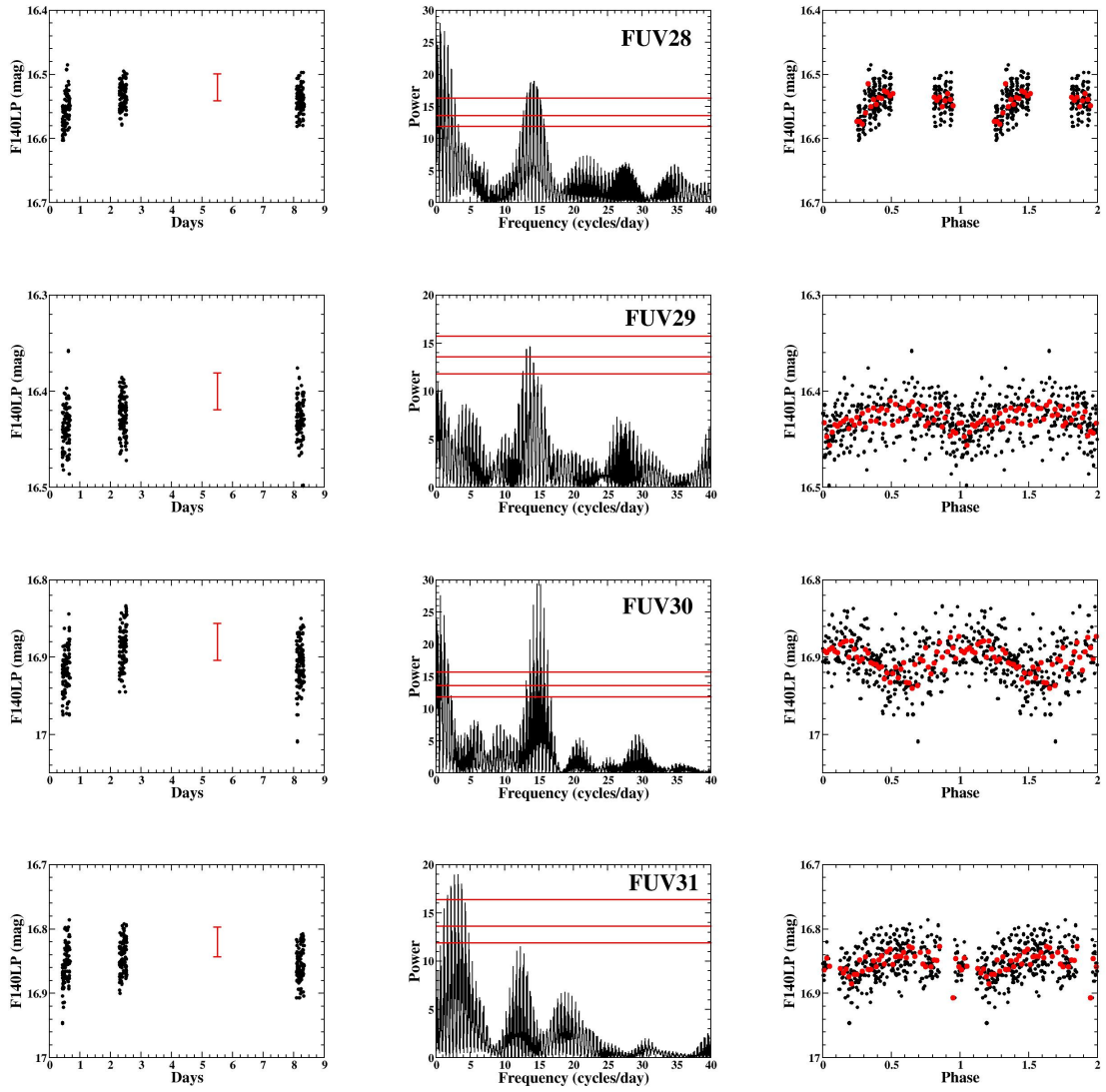

FIGURE 5.12: Each row is for a variable candidate (**FUV28**, **FUV29**, **FUV30**, and, **FUV31**) labeled on the left. The left most column of figures is the photometry for the variable as a function of the time of the observation. Note the distinctive pattern of the three visits. The red bar at 5.5 days (between visits 2 and 3) has a length 2× the mean photometric error. The middle column is the power spectrum of the observations with the power on the y-axis and frequency (cycles/day) on the x-axis. The more likely frequencies have the most power. The right most column is the observations phased on the best frequency from the middle panel. The red dots are the mean magnitude for each 0.02 of phase. Each of these variable candidates is discussed in the text.

FUV33, second row of Figure 5.13, does not have any peaks above the 95% level in the power spectrum. The largest peak in the power spectrum has a period of $\approx$ 2.2 hours. The strongest peak in the bootstrap trials (Figure 5.15) is at a frequency of 0.2615 c/d with $\sim$ 250 trials. This frequency is a very common peak among all the variable candidates bootstrap trials and given the number of trials in this peak it would indicate that the period is uncertain. The observations have been phased on the period corresponding to the peak in the power spectrum and has an amplitude of $\sim$ 0.02

magnitudes (Figure 5.13). I have included this object for completeness, though, it is quite apparent that the variations are at the limit of what can be detected in my dataset. Note that this source is in the region not covered by the F336W image and is not in the ultraviolet colour magnitude diagram (Figure 5.2). Additional analysis and observations are required to confirm or rule out this period.

FUV34, third row of Figure 5.13, has several peaks above the 99.9% level in the power spectrum. The largest peak in the power spectrum has a period of $\approx$ 20.4 hours. There are a couple peaks in the bootstrap trials (Figure 5.15) and the highest peak has $\sim$ 4700 trials and a frequency of 1.1793 c/d ($\approx$ 20.4 hours). The observations have been phased to the $\approx$ 20.4 hour period (Figure 5.13). The light curve is incomplete but still has an amplitude of $\sim$ 0.06 magnitudes. Note that this source is in the region not covered by the F336W image and is not in the ultraviolet colour magnitude diagram (Figure 5.2). The reality of the variation of this star will require additional observations to confirm.

FUV35, fourth row of Figure 5.13, has several peaks above the 99.9% level in the power spectrum. The largest peak in the power spectrum has a period of $\approx$ 20.2 hours. There are a couple peaks in the bootstrap trials (Figure 5.15) and the highest peak has $\sim$ 1550 trials and a frequency of 1.1906 c/d ($\approx$ 20.2 hours). The observations have been phased to the $\approx$ 20.2 hour period (Figure 5.13). The light curve is incomplete but still has an amplitude of $\sim$ 0.07 magnitudes. Note that this source is in the region not covered by the F336W image and is not in the ultraviolet colour magnitude diagram (Figure 5.2). The reality of the variation of this star will require additional observations to confirm.

FUV36, fifth (or bottom) row of Figure 5.13, does not have any peaks above the 95% level in the power spectrum. The largest peak in the power spectrum has a period of $\approx$ 2.0 hours. The strongest peak in the bootstrap trials (Figure 5.15) is at a frequency of 0.2615 c/d with $\sim$ 230 trials. This frequency is a very common peak among all the variable candidates bootstrap trials and given the number of trials in this peak it would indicate that the period is uncertain. The observations have been phased on the period corresponding to the peak in the power spectrum ($\approx$ 2.0 hours) and has an amplitude of $\sim$ 0.03 magnitudes (Figure 5.13). I have included this object for completeness, though, it is quite apparent that the variations are at the limit of what can be detected in my dataset. Note that this source is in the region not covered by the F336W image and is not in the ultraviolet colour magnitude diagram (Figure 5.2). Additional analysis and observations are required to confirm or rule out this period.

The detection of variability on the blue horizontal branch is a very exciting result. Very few variable blue horizontal branch stars have been found in globular clusters (Brown et al. 2013; Moni Bidin et al. 2011) prior to these results. Among the Galactic field population variability is common (Copperwheat et al. 2011; Ostensen et al. 2012). In other words, if the variability of blue horizontal branch stars in this study can be confirmed, it will be a significant result.

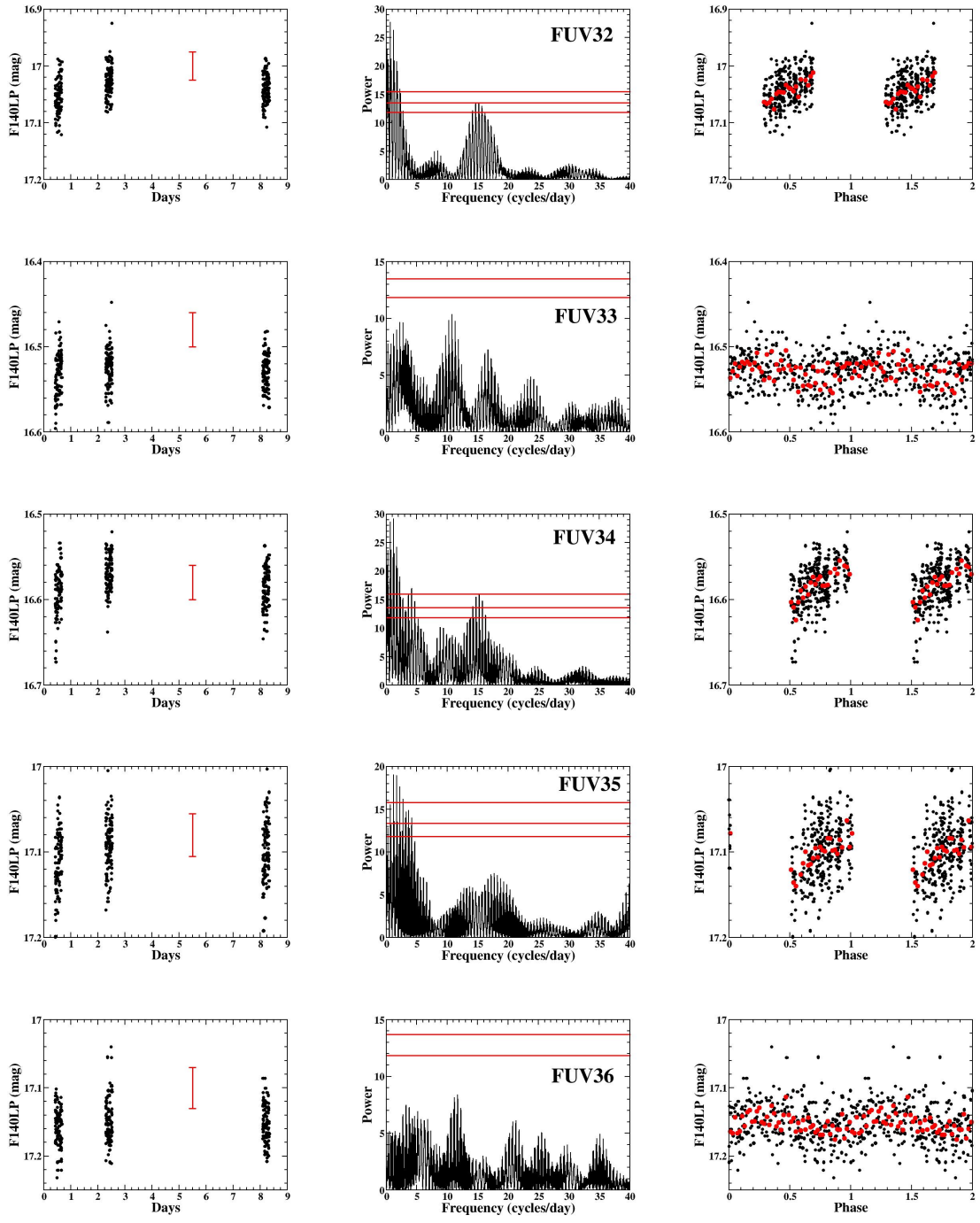

FIGURE 5.13: Each row is for a variable candidate (**FUV32**, **FUV33**, **FUV34**, **FUV35**, and, **FUV36**) labeled on the left. The left most column of figures is the photometry for the variable as a function of the time of the observation. Note the distinctive pattern of the three visits. The red bar at 5.5 days (between visits 2 and 3) has a length 2× the mean photometric error. The middle column is the power spectrum of the observations with the power on the y-axis and frequency (cycles/day) on the x-axis. The more likely frequencies have the most power. The right most column is the observations phased on the best frequency from the middle panel. The red dots are the mean magnitude for each 0.02 of phase. Each of these variable candidates is discussed in the text.

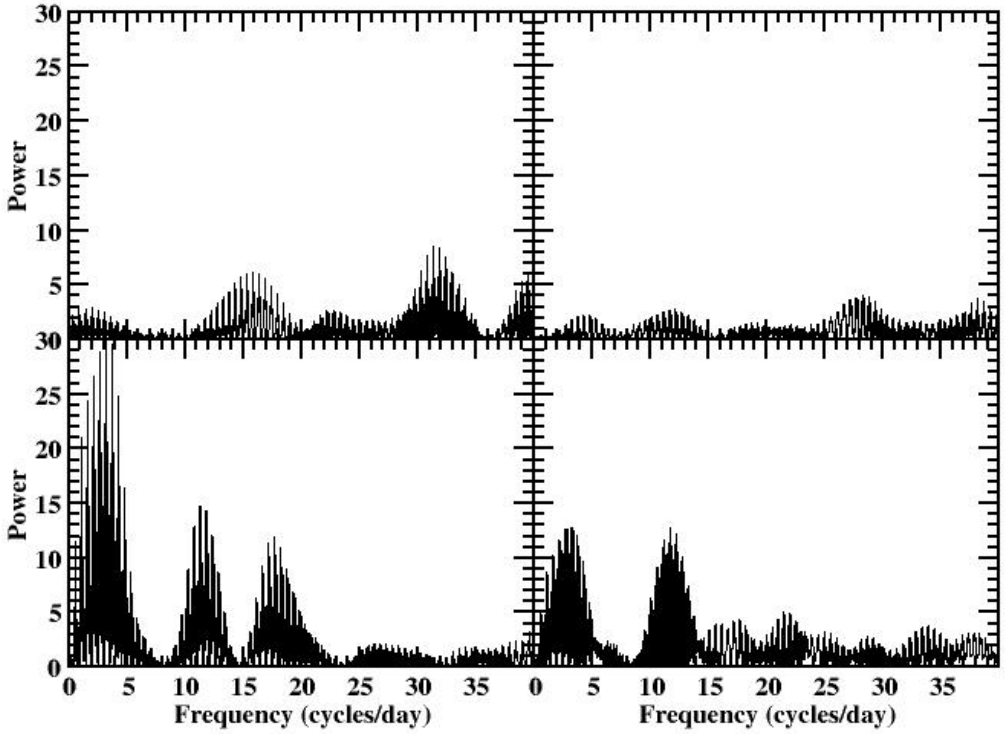

FIGURE 5.14: Top left: The power spectrum of a star of constant magnitude with added white noise. The white noise has a mean amplitude of ~ 0.02 magnitudes which is similar to that of the photometric errors of the BHB stars. Top right: Same as the top left except the mean amplitude of the white noise has been increase to ~ 0.05 magnitudes. Bottom left: The same as the top left with a sinusoidal signal with a period of 8 hours an amplitude (minimum to maximum) of 0.02 magnitudes. Bottom right: Same as the bottom left except with the mean amplitude of the white noise increased to ~ 0.05 magnitudes.

statistical significance is therefore usually achieved for signals reaching $P_{LS,max} \gtrsim 5-10$.

In Figure 5.14, I show the Lomb-Scargle periodogram for a star of constant magnitude with added white noise. The white noise has an amplitude of ~ 0.02 magnitudes (top left) and ~ 0.05 magnitudes (top right). The mean photometric error for the blue horizontal branch stars is ~ 0.02 magnitudes. There is no statistically significant power (i.e. $P_{LS,max} \gtrsim 5-10$ as discussed in Chapter 3) in either of the periodograms. I added a sinusoidal signal with an amplitude of ~ 0.02 magnitudes to the white noise star on the top left. Statistically significant power is seen at the input period of 8 hours. I added the same sinusoidal signal to the white noise star on the top right. The Periodogram shows two nearly equal peaks. One of the peaks (left most peak) is at the input frequency and the other is an alias. This simple test suggests that the variability I have found among the blue horizontal branch stars may be significant.

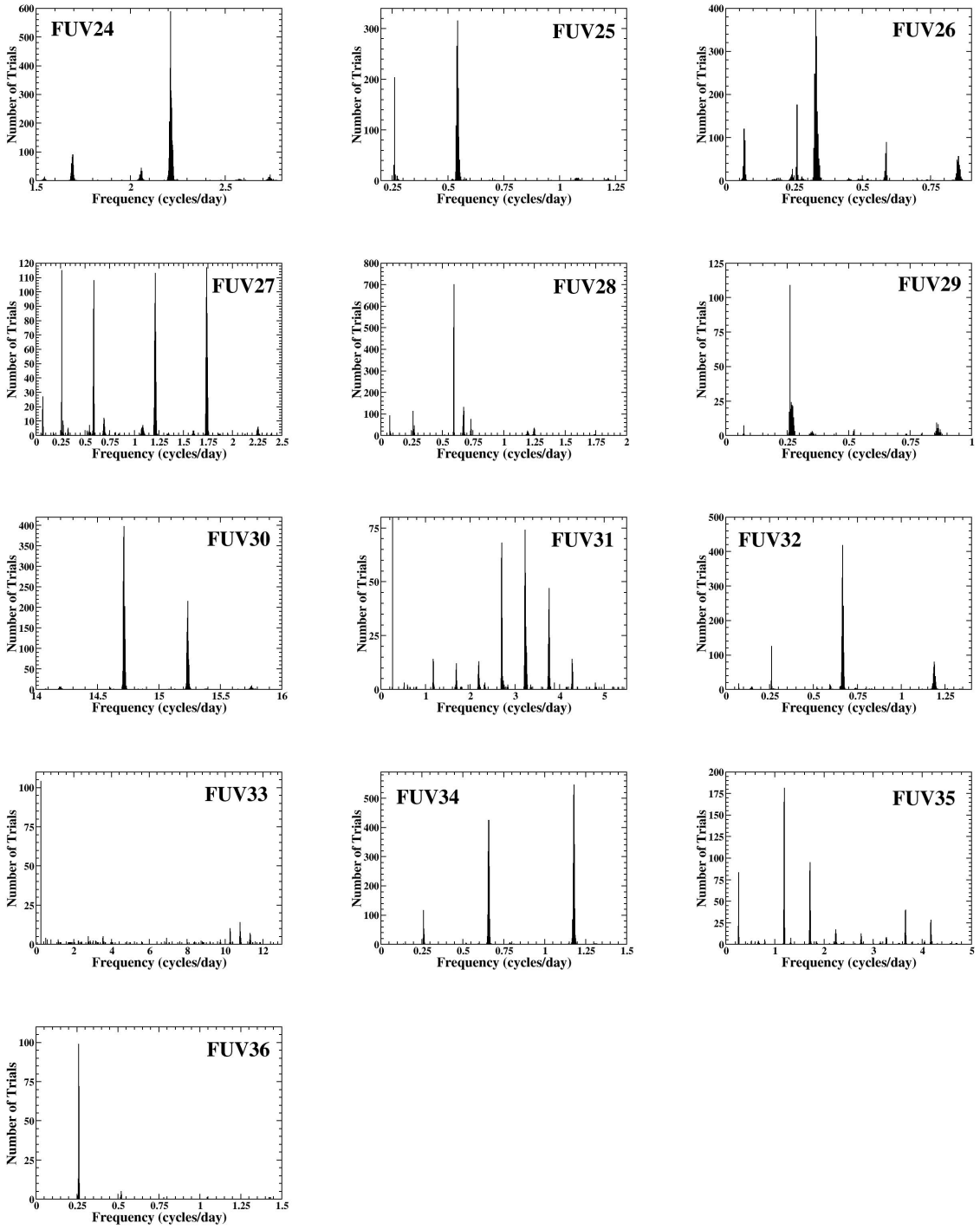

FIGURE 5.15: The results of the bootstrap analysis for each variable. The frequency associated with the peak power from each trial is plotted as a histogram. The bin width of the histogram is 0.001 in frequency. Each of the plots are labeled from the top left (FUV24) to the bottom left (FUV36).

The amplitude (maximum to minimum) of the variation in the 13 variable candidates presented here is less than ~ 0.07 magnitudes in F140LP, though the mean photometric error is ~ 0.02 magnitudes. If the observed amplitude is related to pulsations it is

possible that in the optical may have a reduced amplitude (like it is for RR Lyrae). In a number of cases it is unclear if I have detected the maximum or minimum so the amplitude I quote for each of the variable candidates should be considered a minimum in these cases. It is also possible that these variable candidates are binaries. The addition of radial velocities and/or additional time series at different wavelengths and cadence may provide valuable support for the variation detected here.

5.4 Discussion

I have found 35 candidate variables distributed across three different parts of the cluster CMD: the horizontal branch (both red [RR Lyrae] and blue), the blue straggler region, and the white dwarf sequence (in the ultraviolet CMD; Figure 5.2).

There are 12 likely RR Lyrae among the 35 candidate variables. In general, they exhibit the typical RR Lyrae saw tooth shape in their phased light curves (Figure 5.3, Figure 5.4, and, Figure 5.5), and, except for two sources, they are in the expected location for RR Lyraes in both the optical and ultraviolet colour magnitude diagrams (Figure 5.2). The two exceptions, **FUV2** and **FUV12**, do exhibit the distinctive saw-tooth phase light curves (Figure 5.3 and Figure 5.5 respectively), but **FUV2** is about a magnitude brighter than the locus of the red horizontal branch, and **FUV12** lies redward of the red giant branch in the optical colour magnitude diagram (Figure 5.2).

There are 11 candidate variables among the blue stragglers or where white dwarf + main sequence binaries are expected to lie (Figure 5.2). These 11 candidate variables can be further divided into five likely blue stragglers and six likely white dwarf + main sequence binaries.

The five blue stragglers have periods between $\sim$ 109 minutes and $\sim$ 21.4 hours. The light curve for the shortest period system (109 minutes) looks very similar in shape to those of the RR Lyrae. However, the phased light curve is not smooth, especially at maximum. It may be a SX Phoenicis variable with multiple modes of pulsation. The other four blue stragglers have light curves which could be explained by the blue straggler having a companion in a binary.

The six white dwarf + main sequence binary candidates have the optical colours and magnitudes which places them on the main sequence, while their ultraviolet colours place them to the blue of the main sequence. This is the region of the ultraviolet colour magnitude diagram (Figure 5.2) where I expect to find white dwarf + main sequence binaries to be. One of the strangest light curves is that of **FUV20**, which has a shape similar to that of the RR Lyrae stars, yet it is about 6 magnitudes fainter than other RR Lyraes in this globular cluster. A possible explanation is that this system is a background RR Lyrae. If in the background, it would have to have a distance of about

100,000 parsecs or more (i.e. the furthest extent of the Milky Way halo or beyond). If this source is in the globular cluster and not in the background, another explanation, such as pulsating Helium white dwarf, is needed to explain this system.

Perhaps the most exiting discovery is the detection of 13 blue horizontal branch stars which are varying on timescales from $\sim$ 98 minutes to $\sim$ 3 days. The observed variations have amplitudes of $\lesssim$ 0.07 magnitudes (about a factor of 3 larger than the mean photometric error) in F140LP, which may explain why they haven't been seen previously in the optical. A large fraction of the field populations of this class of stars (known as subdwarf B stars) have been found to be binaries (Copperwheat et al. 2011), and the discovery of binaries among the subdwarf B stars in NGC 1851 would be a significant finding.

The results here would benefit from additional observations, such as spectroscopy or analysis of additional Hubble Space Telescope imaging observations (data in other filters and/or time series with longer durations and/or better cadence). Spectroscopy could reveal the existence of emission lines if the stars are in a semi-detached binary. Also, if radial velocity variations could be detected, this would confirm the binary nature of these systems.

Chapter 6

A Survey for Far-Ultraviolet Transients in the Globular Cluster NGC 6681

Stellar transients are sources that exhibit a sudden increase in luminosity that – depending on the type of transient – can last hours, days or years. In this chapter, I present a search for far-ultraviolet transients in the globular cluster NGC6681. In this waveband and environment, the mechanisms that might produce transients include supernovae, novae and dwarf novae (in order of decreasing luminosity, but increasing probability). X-ray binaries might also produce far-UV transients, since they can be subject to the same disk instability that causes dwarf nova eruptions in accreting white dwarf systems.

There are two basic classes of supernovae. *Core-collapse supernovae* are associated with the deaths of massive stars, while the so-called *Type Ia supernovae* are thought to be produced when the mass of a white dwarf is pushed beyond the Chandrasekhar limit of $1.4M_{\odot}$.

Core-collapse supernovae are only expected in environments where stars with masses $\gtrsim 8M_{\odot}$ are found, since lower mass stars end their lives as white dwarfs. Such massive stars are not found in present-day globular clusters. The typical main-sequence turn-off mass in globular clusters is $\sim 0.9M_{\odot}$, and even the most massive blue stragglers are unlikely to exceed this by more than a factor of $\simeq 2$. Thus core-collapse supernovae are not expected to be produced in globular clusters today.

What about the Type Ia supernovae associated with the collapse of white dwarfs? Dynamical simulations of stellar clusters suggest that the creation of systems such as double degenerates (i.e. two white dwarfs) may be enhanced by dynamical interactions between

stars and binaries in the cluster (Shara & Hurley 2002). Such double-degenerate systems might produce Type Ia supernovae if the combined system mass exceeds the Chandrasekhar limit and if they are able to merge within the lifetime of the cluster. Double degenerate systems themselves may be discoverable via traditional observing techniques (see, for example, the system FUV1 discussed in Chapter 7). However, catching a supernova eruption produced by such systems is extremely unlikely: there are simply too few of them, and they take too long to merge.

Another way of looking at this is that the total Type Ia supernova rate for a Milky-Way-like galaxy is on the order of 1 per 10^4 years (Ruiter et al. 2009). Thus even if all Type Ias were associated with merging (or perhaps accreting) white dwarfs in globular clusters, the chance of catching one is fairly remote. In reality, most Type Ia supernovae are *not* likely to be associated with globular clusters – for example, neither of the last two in the Milky Way (Tycho's and Kepler's supernovae) appear to have been associated with a globular cluster. Similarly, a significant fraction of Type Ia supernovae in external galaxies are known to trace star formation and thus cannot be associated with globular clusters (Galbany et al. 2014). Thus catching a supernova eruption in any one globular cluster is unlikely.

Another type of transient are novae, which are eruptions associated with a thermonuclear runaway on the surface of an accreting white dwarf (e.g. a cataclysmic binary). Once the layer of accreted material exceeds a critical pressure, thermonuclear reactions are triggered. Since the base of this layer is electron degenerate, it cannot initially expand in response to the increase in temperature caused by the nuclear reactions. By the time expansion begins, the runaway is well underway.

Most of the material accreted between nova eruptions is thought to be ejected during the eruptions. During these outbursts, novae are observed to increase in brightness by as much as 20 magnitudes (corresponding to a factor of 10^8 in flux).

To date, two novae have been seen to erupt in the Galactic globular cluster system. T Sco in M80 erupted in 1860 (Sawyer 1938), and another nova outburst was observed in M14 in 1938 (Sawyer Hogg & Wehlau 1964). In addition, two other novae have been caught in eruption in globular clusters in other galaxies, one in M87 (Shara et al 2004), the other in M31 (Kato et al 2013). All of these discoveries were serendipitous. Given the rarity of nova eruptions, a dedicated survey for them in one or more globular clusters would be an inefficient use of competitive telescope time.

Finally, dwarf nova outbursts are also associated with accreting white dwarfs. Dwarf novae are a sub-class of disk-accreting cataclysmic variables that are subject to a disk instability (Mineshige & Osaki 1983). If the mass-transfer rate from the secondary star in a cataclysmic variable lies within the range in which this instability is active, the accretion disk undergoes limit cycles between a low-accretion rate "quiescent" state and the high-accretion rate "outburst" state.

The recurrence time of dwarf nova eruptions can be anywhere from weeks to decades, the outbursts last from days to months, and during outburst the brightness of the system can increase by $\sim 3-6$ magnitudes in the optical. Generally speaking, lower (higher) mass-transfer rates are associated with longer (shorter) recurrence times, longer (shorter) outburst durations, higher (lower) outburst amplitudes and shorter (longer) orbital periods.

Many cataclysmic variables in the field have been discovered as a result of exhibiting dwarf nova eruptions. This, in turn, has likely biased the known field population by under-selecting non- or infrequently-erupting systems. Dwarf novae are certainly thought to dominate the intrinsic population of cataclysmic variables (e.g. Knigge et al 2011). However, evolutionary models suggest that the vast majority of them should be infrequently erupting, low mass-transfer rate, short-period and intrinsically faint systems. This bias can therefore be quite severe (Pretorius & Knigge 2008).

Similarly, early searches for cataclysmic variables in globular clusters focused mostly on dwarf novae. Given the number of eruptions seen in a given cluster in a given time series, it is in principle possible to estimate the total number of cataclysmic variables from such searches.

These early searches all found a much lower number of dwarf novae than predicted by dynamical simulations (Shara et al. 1996). An early suggestion was that perhaps cataclysmic variables in globular clusters are preferentially magnetic systems, in which the magnetic field of the white dwarf truncates the accretion disk or prevents its formation entirely. With only a partial (or perhaps no) disk, such systems are much less likely to exhibit dwarf nova eruptions.

However, a serious problem with the interpretation of these early searches is that they assumed that dwarf novae are typically in eruption $\sim 15\%$ of the time. This is approximately correct for proto-typical dwarf novae like U Gem, for example. However, these proto-types were discovered early on precisely because they are bright and erupt frequently. As noted above, the intrinsic population of cataclysmic variables is likely dominated by systems that are intrinsically faint and erupt extremely infrequently. A much better proto-type for this likely dominant population is WZ Sge, which erupts for roughly ~ 1 month every ~ 30 years. It therefore spends only $\sim 0.3\%$ of its time in eruption (i.e. it has a $\sim 0.3\%$ "duty cycle").

Most dwarf nova searches carried out to date in globular clusters were not very sensitive to such systems, primarily because they did not sample a sufficient number of epochs. For example, the study of 47 Tuc by Shara et al. (1996) relied on only 12 epochs.

The ability of a survey to discovering recurrent transients is solely a function of the transient duty cycle and the number of independent epochs the survey provides. (By

independent epochs, I mean epochs randomly drawn from across the outburst cycle. This typically means epochs spaced further apart than the outburst duration.)

Consider a single transient with duty cycle d in a survey with N independent epochs. The probability of *not* seeing it in outburst in the first epoch is simple $(1-d)$. Similarly, the probability of not seeing it in outburst in *any* epoch is $(1-d)^N$. The probability of seeing the transient in outburst *at least once* in these N epochs is therefore the complement of this, i.e. $P_{detect} = 1-(1-d)^N$. For example, for $d \approx 0.003$ and $N = 8$ (third curve from the right in Figure 6.1) the detection efficiency is only $P \approx 2.4\%$. Surveys with small numbers of epochs are therefore not able to place stringent limits on the number of systems that may be hiding in globular clusters.

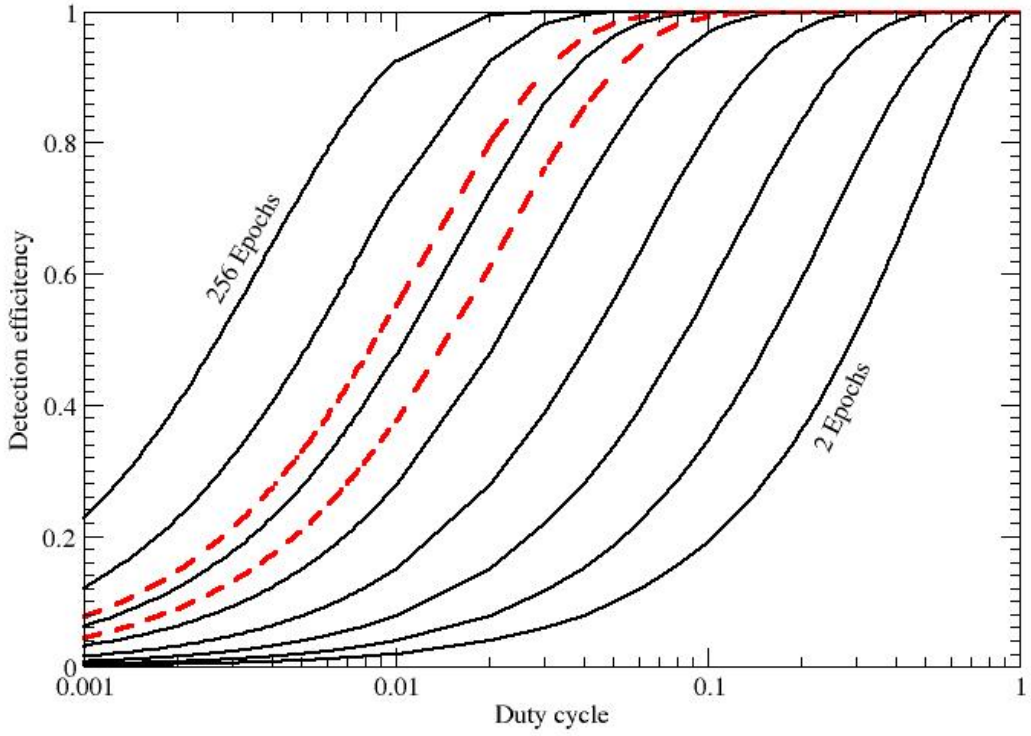

FIGURE 6.1: The dwarf nova detection efficiency as a function of the duty cycle of the source. The black solid lines are calculated (see text) for the number of epochs the observer is using and start with 2 epochs on the right and increase by factors of two to 256 epochs which is the left most curve. The red dashed curves are calculations for the number of independent observations used. The left most curve is calculated for all the observations (80 epochs). The red curve on the right is for all observations with at least 30 days (a month) between each epoch (47 epochs).

The only way to improve on this is by increasing the number of observed epochs over a longer duration. I have obtained such a dataset from the Hubble Space Telescope archive. The globular cluster, NGC 6681 (M70), is used by the ultraviolet cameras on

Hubble Space Telescope as a calibration source to calculate the geometric distortions for each of the detectors and filters. Images have been taken of the cluster core ever since the Space Telescope Imaging Spectrograph was put on the telescope in 1997 and continues to the present. Calibration images have been taken with the Space Telescope Imaging Spectrograph (far-ultraviolet and near-ultraviolet), Advanced Camera for Surveys - Solar Blind Channel (far-ultraviolet), and, Advanced Camera for Surveys - High Resolution Channel (near-ultraviolet). Roughly speaking, far-ultraviolet and near-ultraviolet images have therefore been obtained for this cluster every $\simeq 6$ months over the last $\simeq 20$ years. This provides a uniquely valuable data set for a sensitive dwarf nova search in this cluster. In the remainder of this chapter, I discuss the observations I used, my methods for detecting transients, my results, and what these results imply.

6.1 Searching for Transients

In principle, the search for transients is quite a simple and straight forward process. I am basically looking for objects with substantially different magnitudes between epochs of observations. This could mean a source which is undetected in most epochs, but is present in one or more epochs.

However, there is (at least) one type of object that might complicate the search for "true" transients in the far-ultraviolet (by which I primarily mean dwarf novae in the present context). These objects are RR Lyrae variables. As seen in the previous chapter, RR Lyraes increase in brightness by several magnitudes over relatively short periods of time that are comparable to the recurrence times of frequently erupting dwarf novae. In observations composed of many brief observations, RR Lyrae might be caught in a bright state in one or more epochs, yet remain undetected (or very faint) at other times. This behaviour could mimic that of dwarf novae (e.g. Thomson et al. 2012). However, it is relatively straightforward to distinguish RR Lyrae from dwarf novae based on their characteristics at other wavelengths and their respective positions in colour magnitude diagrams. In any case, NGC 6681 does not harbour any RR Lyrae stars, as it only features *blue* horizontal branch stars well away from the RR Lyrae region of the instability strip.

Our data set is composed of observations taken with two camera/detector combinations. One of these data sets is presented in Table 6.1. This provides the dates on which far-ultraviolet observations with the Space Telescope Imaging Spectrograph were obtained in three different filters. Note that there is a gap of about 6 years between 2004 and 2010 during which no observations were taken with the Space Telescope Imaging Spectrograph. This is because the power supplies of the instrument failed in 2004 and were not repaired until the last servicing mission in 2010.

The other camera/detector data set was taken with the Advanced Camera for Surveys and its Solar Blind Channel. It is summarized in Table 6.2. Again, the table shows when far-ultraviolet observations were taken with the various filters available with this camera/detector. Note that there is no gap between 2004 and 2010, as the Solar Blind Channel continued to operate throughout this period.

Figure 6.2 shows the field of view covered by a single ACS/SBC observation. This is slightly larger than the field of view covered by the Space Telescope Imaging Spectrograph. Given that the images from different epochs are not perfectly aligned, the field covered by *all* epochs is, of course, significantly smaller. However, as shown in Figure 6.2, the core radius of NGC 6681 (and also 3x, and even 10x the core radius) falls comfortably within this field of view. The area covered by all of our epochs should therefore include the majority of all of the cataclysmic variables in this cluster, so long as these are centrally concentrated.

The bright sources in Figure 6.1 are the blue horizontal branch stars. These sources are the reason why this cluster was chosen for measuring and calibrating geometric distortions. The images for each epoch/filter combination were combined (e.g. Figure 6.2) using the astrodrizzle software (Gonzaga et al. 2012).

I began with the simplest possible search for transients. After aligning all epochs to a common reference frame, I simply blinked the images for each epoch against each other and searched for sources blinking on and off visually. My experience using this technique to discover transients (e.g. Novae in the Virgo galaxy M87) suggests that this technique is highly efficient at discovering transients (even the faintest ones). I discovered no candidate transients in NGC 6681 using this method.

I created a catalog of positions for all the ultraviolet sources from a summed image of all the far-ultraviolet images. I over plotted the positions in the resulting catalog onto each individual epoch image to ensure that all sources have been found. Once I confirmed the catalogs completeness I used it as input to conduct aperture photometry for each individual epoch and filter. The photometry for each source in each of the filters was used to determine a magnitude difference between epochs. A transient will present itself as a large change between epochs (i.e. > 1.0 magnitude). I discovered no candidates using this method.

6.2 Examination of the Result

Our examination of all 85 epochs of far-ultraviolet images revealed no dwarf novae within the field of view. In order to highlight the meaning of this non-detection, I return to Figure 6.1. As already discussed above, this shows the detection efficiency of transient surveys with different numbers of epochs to transients with a wide range of duty cycles.

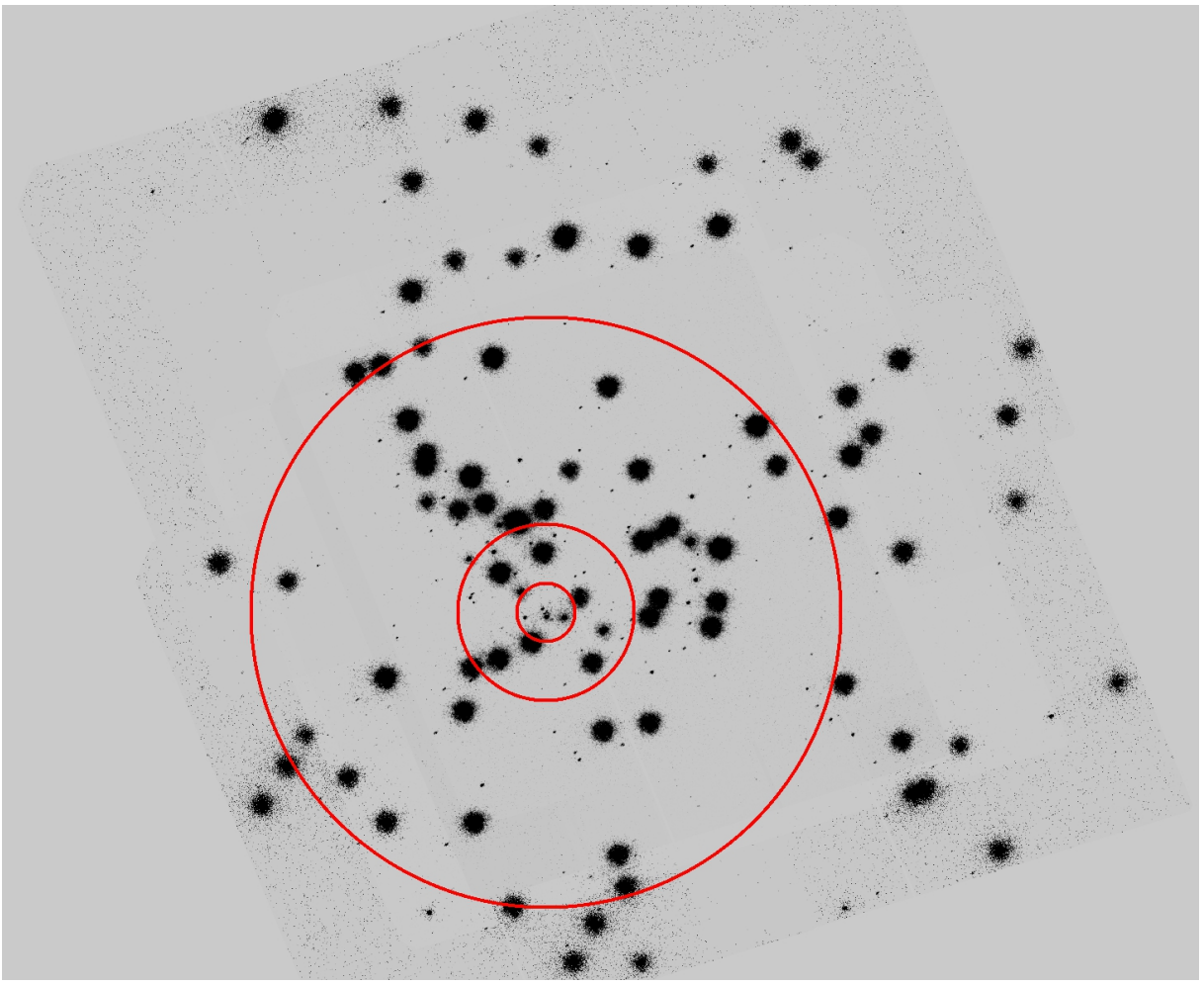

FIGURE 6.2: A far-ultraviolet image (F150LP) with north to the top and east to the left was taken with the Advanced Camera for Surveys/ Solar Blind Channel. This represents the largest field of view for any epoch and all other epochs/filters are contained within this field of view. The three red circles are centered on the center of the globular cluster with the smallest circle equal to the core radius of 1.8″. The middle circle is three times the core radius or 5.4″, The largest circle represents 10 times the core radius or 18″.

For example, if the expected duty cycle for dwarf novae is 10% (i.e. 0.1), I expect to detect $\simeq$ 18% of these systems with just two epochs and $\simeq$ 33% with 4 epochs. With $\gtrsim$50 epochs, I would effectively detect all of them.

Real dwarf novae exhibit a large spread in duty cycles, ranging from $\gtrsim$ 15 to $\lesssim$ 1% (Coppejans et al (2016); also see the examples of U Gem and WZ Sge above). As shown in Table 6.1 and Table 6.2, our total survey is comprised of 80 epochs. Assuming all of these epochs to be independent, I obtain the constraint shown by the left-most red line in Figure 6.1. In this case, our survey would be essentially 100% complete for dwarf novae with duty cycles of $\gtrsim$5%, and still 60% complete for systems with duty cycles of 1%.

A more pessimistic scenario would be to consider only epochs spaced by more than $\simeq$ 1 month as independent (right red dashed curve). This would be appropriate if WZ Sge

Date of Observation (yyyy-mm-dd)	25MAMA	F25QTZ	F25SRF2
1997-05-26		✓	✓
1997-07-06	✓		
1997-09-29	✓	✓	✓
1997-11-06	✓		✓
1998-03-29	✓	✓	
1998-09-17	✓	✓	✓
1999-03-24	✓	✓	
1999-09-17	✓	✓	✓
2000-03-27	✓	✓	✓
2000-09-18	✓	✓	✓
2001-03-28	✓	✓	✓
2001-09-27	✓	✓	✓
2002-02-26	✓	✓	✓
2003-03-27	✓	✓	✓
2004-03-04	✓	✓	✓
2010-05-07	✓	✓	✓
2011-04-16	✓	✓	✓
2012-03-14	✓	✓	✓
2013-04-13	✓	✓	✓
2014-04-10	✓	✓	✓
2015-04-10	✓	✓	
2016-03-27	✓	✓	✓

TABLE 6.1: Far-ultraviolet observations taken with the Space Telescope Imaging Spectrograph. The check marks indicate that observations were taken in that filter on that date. The gap between 2004-03-04 and 2010-05-07 is due to the failure of the power supply on the instrument. This was repaired in the final servicing mission to the Hubble Space Telescope.

is typical of most dwarf novae in globular clusters, as might be expected theoretically. In this case, N = 47, and our detection efficiency is still $\gtrsim 99\%$ for duty cycles $\gtrsim 10\%$ and $\approx 38\%$ for duty cycles of 1%. Even if typical duty cycles are as low as 0.3% (as in WZ Sge), our detection efficiency is a respectable 13%. That is, our survey is expected to detect 13 out of 100 such systems (plus, of course, most or all of the more frequently erupting ones).

Our non-detection of *any* dwarf nova eruptions thus places an upper limit on the number of dwarf novae in NGC 6681. Following Pretorius et al. (2007), I note that detecting zero outbursts in one specific survey allows me to place a 2-σ upper limit of 3 on the mean number that might have been detected in similar surveys. Allowing for our detection efficiency of 13%, I can therefore place a 2-σ upper limit of 22 on the number of WZ Sge-like dwarf novae in our field of view. Upper limits on the numbers of more frequently erupting dwarf novae are, of course, even smaller.

6.3 Discussion

It is interesting to compare my non-detection of erupting DNe in NGC 6681 to the only other well studied globular cluster, NGC 104 (47 Tucanae). In the original study by Shara et al (1996) found one erupting dwarf novae using 12 epochs of near-ultraviolet

imaging data. In a more complete study Shara et al (2017) have found a total of 4 erupting variables in ~ 43 epochs (blue line in Figure 6.1). Our study, in comparison, has found zero erupting variables in a maximum of 80 epochs.

If the formation of CVs in GCs is dominated by dynamical processes (see e.g. Pooley & Hut 2006), the number of CVs is epxected to scale with the stellar encounter rate, as indeed it does for X-ray binaries (Bahramian et al 2013). Given that the stellar encounter rates of NGC 104 and NGC 6681 are comparable (Bahramian et al 2013), as is the number of widely separated epochs available for both clusters, I would then expect to have found 4 DNe in NGC 6681. My detection of zero such systems is therefore a marginally significant hint that the properties of the CV populations may be different in the two clusters and/or that CV production in GCs is not dominated by stellar dynamics.

If, on the other hand, the number of CVs scales with the total mass of a cluster – as may be expected if most present-day CVs evolved from primordial binaries (e.g. Davies 1997)– I would need to scale the Shara et al. (2017) result by the ratio of masses between NGC 104 and NGC 6681. NGC 104 is about 8 times more massive than NGC 6681, thus I would expect to find ~ 0.5 DNe in NGC 6681, given the detection of 4 such systems in NGC 104 by Shara et al (2017). This scenario is therefore consistent with my non-detection.

It is also important to compare my results to theoretical predictions. For example, Ivanova et al (2006) predict ~ 1 detectable CV per $1000 M_{\odot}$ in the cluster core. If this prediction is coreect, I would expect to have found at least one DNe, so long as the characteristic duty cycle for eruptions is $d > 0.0045$. Thus it is possible to reconcile my non-detection with theoretical predictions, provided that CVs in NGC 6681 (and, by extension, in other GCs) have duty cycles that are comparable to or lower than WZ Sge-like CVs. This is plausible from the point of view of binary evolution, since most CVs in GCs should have had time to evolve to such a low-$\dot{M}$ state.

An alternative way to reconcile the absence of erupting DNe in my survey with the theoretically expected CV population is to assume that CVs in GCs are preferentially magnetic. For example, intermediate polars have a truncated disk, and the instabilities which cause the sudden emptying of the disk and subsequent dwarf nova outburst are less frequent if they happen at all in these systems. The polars have no disk and thus do not have dwarf nova outbursts. Of course, this begs the question as to why magnetic CVs should be overabundant in GCs. One possible answer is that strong magnetic fields are more commonly associated with massive WDs (Vennes 1999). Given that massive WDs are more likely to undergo dynamical encounters, and hence may be more efficient at forming CVs, this might explain why magnetic CVs are more efficiently formed in GCs than in the Galactic field (Ivanova et al. 2006).

Date of Observation (yyyy-mm-dd)	F115LP	F122M	F125LP	F140LP	F150LP	F165LP
2002-05-27	✓		✓	✓	✓	✓
2002-05-30		✓	✓		✓	
2002-06-02			✓			
2002-06-04	✓		✓	✓	✓	✓
2002-06-09	✓		✓	✓	✓	✓
2002-06-30	✓		✓	✓	✓	✓
2002-07-12	✓		✓	✓	✓	✓
2002-07-26	✓		✓	✓	✓	✓
2002-08-06	✓		✓	✓	✓	✓
2002-08-11	✓		✓	✓	✓	✓
2002-08-20	✓		✓	✓	✓	✓
2002-08-30	✓		✓	✓	✓	✓
2002-09-06	✓		✓	✓	✓	✓
2002-09-11	✓		✓	✓	✓	✓
2002-09-27	✓		✓	✓	✓	✓
2002-10-15	✓		✓	✓	✓	✓
2002-11-10	✓		✓	✓	✓	✓
2003-02-19	✓		✓	✓	✓	✓
2003-03-15	✓		✓	✓	✓	✓
2003-04-17	✓		✓	✓	✓	✓
2003-05-14	✓		✓	✓	✓	✓
2003-06-12	✓		✓	✓	✓	✓
2003-07-18	✓		✓	✓	✓	✓
2003-08-15	✓		✓	✓	✓	✓
2003-09-15	✓		✓	✓	✓	✓
2003-10-14	✓		✓	✓	✓	✓
2004-03-22	✓		✓	✓	✓	✓
2004-06-20	✓		✓	✓	✓	✓
2004-09-07	✓		✓	✓	✓	✓
2005-04-05	✓		✓	✓	✓	✓
2006-03-01	✓		✓	✓	✓	✓
2006-03-16	✓		✓	✓	✓	✓
2006-08-02	✓		✓	✓	✓	✓
2007-03-01	✓		✓	✓	✓	✓
2007-03-18	✓		✓	✓	✓	✓
2007-04-04		✓				
2007-04-22	✓		✓	✓	✓	✓
2008-03-06	✓		✓	✓	✓	✓
2008-07-19	✓		✓	✓	✓	✓
2009-05-02	✓		✓	✓	✓	✓
2009-05-30	✓		✓	✓	✓	✓
2009-06-05	✓		✓	✓	✓	✓
2009-06-11	✓	✓	✓	✓	✓	✓
2010-03-05	✓		✓	✓	✓	✓
2010-03-07		✓				
2010-06-29		✓				
2010-07-02	✓		✓	✓	✓	✓
2011-04-13	✓	✓	✓	✓	✓	✓
2012-03-13	✓			✓	✓	
2012-03-18		✓				
2013-04-21	✓		✓	✓	✓	✓
2013-05-16		✓				
2014-03-26		✓				
2014-04-03	✓		✓	✓	✓	✓
2015-03-27	✓		✓	✓	✓	✓
2015-04-15		✓				
2016-03-09	✓		✓	✓	✓	✓

TABLE 6.2: Far-ultraviolet observations taken with the Advanced Camera for Surveys/ Solar Blind Channel. The check marks indicate that observations were taken on that date in that filter. There is no gap in between 2004 and 2010 as this camera never stopped working.

Chapter 7

A variable with an 18 minute period: an AM CVn candidate

This chapter is the results from the paper Zurek et al (2016). A number of authors contributed to results presented here. Ata Saradejini supplied the photometric catalog for the ACS/WFC observations which were published in Milone et al (2008). The detection threshold from the X-ray observations was supplied by David Pooley. The two component fits and plots for the SED (Figure 7.7 and Figure 7.10) were supplied by Christian Knigge.

7.1 Introduction

Globular clusters (GCs) are well known for containing interacting binaries, such as low-mass X-ray binaries (LMXBs; Clark 1975; see Pooley 2010 for a recent review) and cataclysmic variables (CVs; Margon et al 1981; see Knigge 2011 for a recent review), as well as the remnants of binary interactions and collisions, such as Helium white dwarfs (HeWDs; Cool et al 1998), blue stragglers (BSs; Sandage 1953; Gilliland et al 1998) and millisecond pulsars (MSPs; Lyne et al 1987). As a result of the dynamical interactions taking place in dense star clusters, the populations of LMXBs and MSPs in GCs are significantly enhanced relative to the Galactic field (Clarke 1975; Camilo & Rasio 2005). Some theoretical simulations suggest that the numbers of CVs and HeWDs should also be enhanced in GCs (Di Stefano & Rappaport 1994; Davies 1997), though this effect is tempered by gravitational hardening (Shara & Hurley 2006). Conclusive observational evidence of an enhancement or deficit of CVs and HeWDs has yet to be found, but the importance of dynamics in regulating the size of the CV populations in GCs has already been established (Pooley & Hut 2006).

The expected enhancement of compact interacting binaries is ultimately due to the high encounter rates in GCs (Pooley et al 2003; Heinke et al 2003; Bahramian et al 2013). The encounter rate is a function of the stellar density and velocity dispersion, and, since the stellar density in a GC is high compared to the field, interactions occur much more frequently. NGC 1851 has an encounter rate that is one of the ten largest among the Galactic GCs (Bahramian et al 2013). The large number of star-star, star-binary and binary-binary encounters results in the tightening of binaries, exchanges of stars into and out of binaries, and stellar collisions (Leigh & Geller 2012; Geller & Leigh 2015). It is expected that these interactions lead to the formation of interacting compact binaries containing accreting black holes, neutron stars and white dwarfs.

Multiple examples of all three types of accreting compact binaries have already been discovered in GCs (Strader et al 2012; Chomiuk et al 2013; Maccarone et al 2007; Heinke et al 2003). However, all accreting WDs found to date in GCs are located in binary systems with main sequence or sub-giant donor stars (Knigge 2012). Theoretically, accreting WDs fed by red giants ("symbiotic stars") or by low-mass WD donors (AM CVn stars) are also predicted, but no such systems have been discovered to date. Here, we report the discovery of the first strong candidate AM CVn star in a GC. This source, N1851-FUV1, is almost certainly an accreting WD binary system, so the main challenge is to determine the nature of its binary companion. We therefore begin by summarizing the main possibilities.

Interacting binaries composed of a WD and a Roche-lobe-filling main-sequence star are known as CVs (Warner 1995; Knigge et al. 2011). The orbital periods of these systems typically range from $\simeq 75$ minutes to about a day. The WDs in CVs can have varying magnetic field strengths. The magnetically weakest ("non-magnetic") CVs have accretion disks which extend all the way to the surface of the WD. Conversely, the magnetically strongest CVs, known as polars, have no accretion disks at all. In polars, the gas from the Roche-lobe-filling companion instead flows along the magnetic field lines to impact on the magnetic poles of the WD. Finally, CVs hosting WDs with intermediate magnetic fields, known as intermediate polars (IPs), contain truncated accretion disks whose inner edge lies well outside the WD radius (Patterson 1994). Material reaching the truncation radius then flows along the magnetic field lines and again lands on the WD's magnetic poles. The impact region is hotter than the surrounding WD surface, and the magnetic poles are often not aligned with the rotational axis. As a result, the impact regions rotate in and out of view for many lines of sight, causing periodic variation in observed light curves that are associated with the WD spin (Patterson 1994).

The class of interacting binaries known as AM CVs stars are similar to CVs in that they contain a Roche-lobe-filling secondary that supplies material to an accretion disk around a WD primary. However, while the secondaries in CVs are typically main-sequence stars, those in AM CVns are degenerate or semi-degenerate objects, such as Helium WDs (HeWDs). Thus the evolutionary paths of AM CVn binaries are very

different from that of the general CV population (Solheim 2010). AM CVn stars are extremely compact binaries, with orbital periods less than $\simeq 65$ minutes (Solheim 2010). They are also relatively rare ($\simeq 40$ are known to date; Levitan et al. 2015), and, without dynamical enhancement, only about one AM CVn would be expected to exist in each GC (Nelemans et al 2001). In addition, AM CVns are generally faint at optical wavelengths, and the detection of the orbital period can be difficult.

Symbiotic binaries are also generally accreting WD binary systems (although a rare subset may have neutron star or black hole primaries). However, the donor star in symbiotics is on either the red giant branch (RGB) or the asymptotic giant branch (AGB) (Kenyon 1990; Mikolajewska 2003). In the field, symbiotic binaries have periods of hundreds to thousands of days (Mikolajewska 2003). In a GC, tight binaries are expected to become tighter and wide binaries are expected to become wider through interactions with other stars (Heggie's Law: Heggie 1975). Very wide binaries will eventually become detached through these interactions, so systems with periods greater than about 500 days should be extremely rare (Heggie 1975). Near misses or fly-by encounters may also result in highly eccentric orbits (Heggie & Rasio 1996). An orbital period shorter than about 100 days would then lead to mass exchange through Roche-lobe overflow or a common envelope phase. Thus, in a GC, symbiotic binaries would likely be limited to orbital periods in the range of $\simeq 100 - 500$ days and may have highly eccentric orbits. Due to their long periods and the dominant contribution of the donor star at longer wavelengths, symbiotic stars will usually be missed by optical variability surveys. In fact, such systems can generally only be discovered by searches sensitive to emission lines (Kenyon 1990; Mikolajewska 2003), blue/UV excess and/or fast variability associated with accretion-induced flickering or the spin period of an accreting magnetic WD.

Here, we present observations of a short-period variable star (N1851-FUV1) with a significant blue excess in the core of the GC NGC 1851. Based on its X-ray, photometric and spectroscopic properties, we suggest that it is most likely an AM CVn star or perhaps an unusual X-ray weak IP. In Section 2 we present a summary of the data sets used and our analysis of the photometry, variability, spectra and X-ray observations. We discuss the possible interpretations and fits to the SED in Section 3 and present our conclusions in Section 4.

7.2 Data and Analysis

We obtained FUV timeseries observations of the core of NGC 1851 using ACS/SBC on HST (GO program 10184). We supplemented these observations with archival WFPC2, ACS/WFC and STIS/FUV-MAMA images. These datasets are listed in Table 1 and described in Sections 2.1 and 2.2.

TABLE 7.1: Hubble Space Telescope imaging observations

Proposal #	Date of Observations	Instrument	Filter	Number of Exposures	Total Exposure time (sec)
GO-6095	1995-10-05	WFPC2	F218W	2	1600
GO-6095	1995-10-05	WFPC2	F439W	4	360
GO-6095	1995-10-05	WFPC2	F555W	2	46
GO-5696	1996-04-10	WFPC2	F336W	4	3600
GO-5696	1996-04-10	WFPC2	F439W	3	1200
GO-7363	1999-03-24	STIS/FUV-MAMA	F25QTZ	8	11000
GO-10775	2006-05-01	ACS/WFC	F814W	1	20
GO-10775	2006-05-01	ACS/WFC	F606W	1	20
GO-10184	2006-08-15	ACS/SBC	F140LP	273	24390
GO-11975	2009-05-02	WFPC2	F170W	3	2100
GO-11975	2009-05-02	WFPC2	F255W	3	3700
GO-11975	2009-05-02	WFPC2	F336W	4	2440
GO-11975	2009-05-02	WFPC2	F555W	4	141

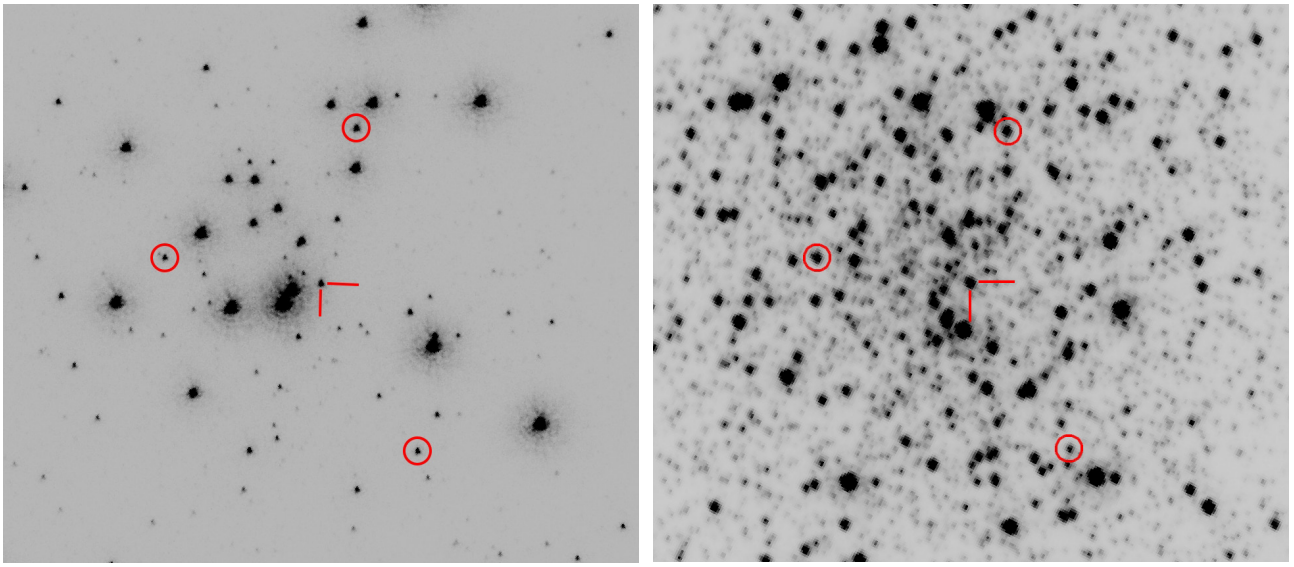

FIGURE 7.1: The central 11″ of NGC 1851 (North up and East left) with the FUV image on the left and the optical (F555W) image on the right. The position of the variable object is identified by the red tick marks. We have circled 3 stars in common between the two images to assist in identifying stars in common as the stellar density is very high in this core collapsed cluster. The field of view is 11″ in both North-South and East-West.

Our initial analysis suggested a symbiotic binary or an IP as the most likely scenarios for N1851-FUV1. In order to test these ideas, we obtained additional optical spectroscopy with HST and deep X-ray imaging with *Chandra*. The spectroscopy was obtained with the STIS/CCD/G430L instrument/detector/grating combination (GO program 13394) and is discussed in Section 7.2.3. The archival ((ObsID 8966) and new (ObsID 15735) X-ray observations are described in Section 7.2.4.

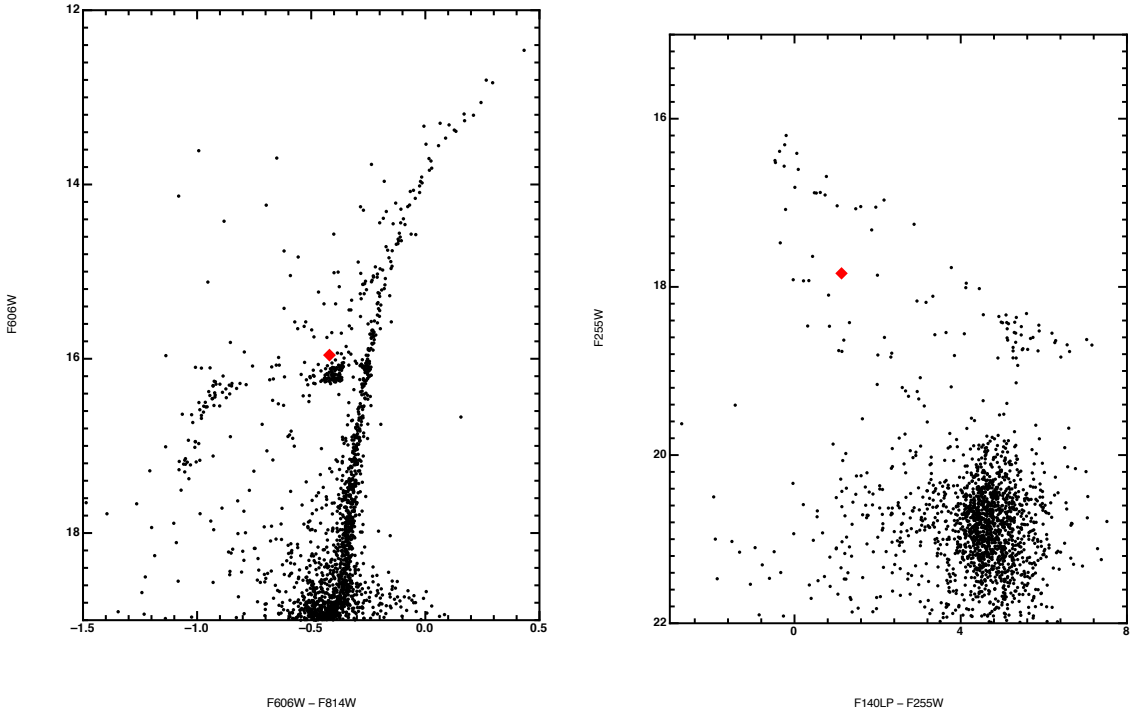

FIGURE 7.2: The F606W/F814W CMD (Left Panel) from the photometric catalog of Milone et al. The location of the variable source is marked with a red diamond. It is located just above the red horizontal branch clump.The F255W/F140LP CMD (Right Panel) from our photometric reductions. The location of the variable source is marked with a red diamond. It is in the same locus as the bright blue straggler stars below the blue end of the horizontal branch.

7.2.1 Optical and Ultraviolet Imaging

The WFPC2 PC images of the core of NGC 1851 contain about 50 stars per arcsec^2 (Figure 7.1, right panel). We therefore carried out point spread function (PSF) fitting photometry using ALLSTAR (Stetson 94) in order to minimize errors due to crowding. The ultraviolet images taken with the ACS/SBC and STIS/FUV-MAMA (Figure 7.1, left panel) require only aperture photometry, as the crowding in the ultraviolet is considerably reduced. The ACS/WFC photometry was taken from Milone et al (2008), who carried out PSF-fitting photometry as fully described in Anderson et al (2008).

In order to match sources across cameras, detectors and filters, we started by considering a small set of bright sources common among the filters and cameras. These bright sources are nearly exclusively hot horizontal branch stars, and we used their positions as fiducial points to calculate preliminary spatial transformations. These preliminary transformations were then used to extend the matching to all detected sources and to refine the transformations. We consider a source in one filter/camera to be matched with a detection in another filter/camera if the separation is at most one optical pixel or two far-UV pixels. Both optical detectors used have pixel sizes of $\simeq 0.05''$, while both far-UV detectors have pixel sizes of $\simeq 0.025''$.

TABLE 7.2: N1851-FUV1 magnitudes

Filter	Pivot Wavelength (Å)	Year	N1851-FUV1 (ST mags)
F814W	8058.8	2006	16.378
F606W	5921.6	2006	15.958
F555W	5442.9	1995	16.089
F555W	5442.9	2009	16.067
F439W	4312.1	1995	15.963
F439W	4312.1	1996	16.061
F336W	3359.5	1996	16.847
F336W	3359.5	2009	16.873
F255W	2600.4	2009	17.839
F218W	2204.4	1995	18.135
F170W	1831.2	2009	18.079
F25QTZ	1595.7	1999	18.971
F140LP	1528.0	2006	18.886

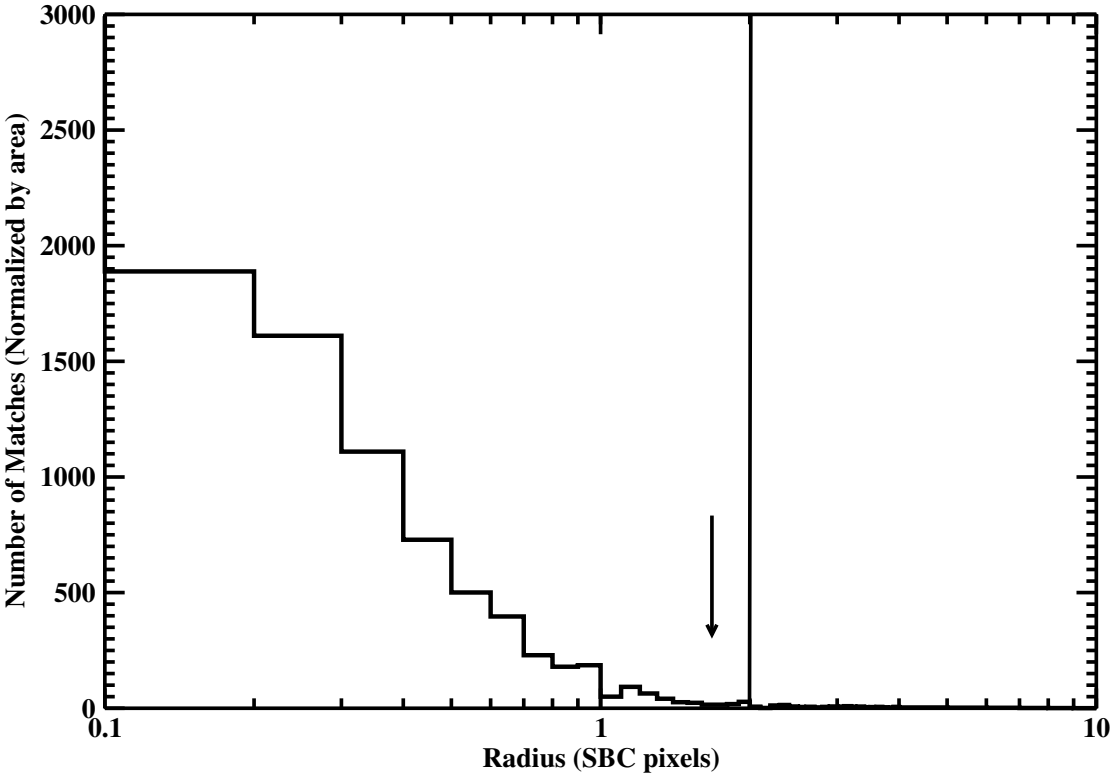

FIGURE 7.3: The distribution of matches between the far-ultraviolet and the optical as a function of separation. We indicate our radius (solid vertical line) of acceptance at 2 ACS/SBC pixels. We indicate with the arrow the separation between the FUV and optical components of N1851-FUV1.

Our photometric measurements for N1851-FUV1 are listed in Table 2 and shown in the context of the relevant cluster colour-magnitude diagrams (CMDs) in Figure 7.2. In the left panel, we show the optical V vs V-I CMD (V=F606W & I=F814W) constructed from the photometric catalog of Milone et al. (2008), where V = m(F606W) and I = m(F814W). In the right panel, we show our matched ultraviolet NUV vs FUV-NUV CMD, where FUV = m(F140LP) and NUV = m(F255W). In both CMDs, the location of N1851-FUV1 is indicated with a large red diamond symbol. The key point to note

is that N1851-FUV1 appears blue in the ultraviolet CMD, but red in the optical CMD, indicating that it must be composed of both a hot and a cool component.

The crowding in the core of NGC 1851 is quite severe, so it is important to consider the possibility that the unusual location of N1851-FUV1 in the UV and optical CMDs is due to a chance superposition of unrelated hot and cool objects in the cluster. We therefore estimated the probability of such a chance superposition happening via a simple Monte Carlo simulation based on the actual number and locations of the relevant sources in our far-UV field of view. Specifically, we took the positions of all far-UV sources brighter than the main sequence (200 sources), as well as the positions of all sources that are at least as bright and red as the red horizontal branch in the optical CMD (205 sources). We then created a mock data set by randomly shifting the positions of the UV and red sources independently of each other, by amounts much greater than our matching radius, but much smaller than the field of view. Finally, we recorded the number of matches within this mock data set, adopting the same matching radius as for the real data. We repeated this simulation hundreds of times to estimate the probability of finding at least one chance match in our data. The resulting probability is $p \simeq 8\%$.

We also looked into how often a randomly placed source matches with any object in the optical catalog of sources (not restricting ourselves to red giants). Globally the value is $\sim 7\%$ and within about 10 arcseconds of the cluster center the value is $\sim 10\%$.

These probabilities are not negligible and may even be somewhat higher near the cluster center where N1851-FUV1 is located. Thus the possibility that the anomalous colours of N1851-FUV1 could be due to a chance superposition must be seriously considered. The probability that *one specific* UV-bright object – e.g. selected on the basis of exhibiting an 18-min periodic signal – should suffer a chance superposition with a red giant is, of course, much smaller, at $p \simeq 0.3\%$. However, this estimate relies even more on *a posteriori* statistics and should therefore be enjoyed responsibly.

It is worth emphasizing that our estimated chance coincidence probabilities are officially p-values: they represent the probability of finding as good a match as observed under the null hypothesis that there is no physical association(and $1 - p$ is not the probability that there is an association). In order to explore this issue further, we have therefore examined the possibility that N1851-FUV1's optical counterpart is a chance superposition by examining the distribution of separations between all FUV sources and optical counterparts in our matched photometry (Figure 7.3). The vertical line in this figure is our maximum allowed separation for matches (in ACS/SBC pixels - see above). The arrow indicates the separation between N1851-FUV1 and its optical counterpart, which lies quite far in the tail of the distribution. We also inspected the ACS/SBC and WFC3/UVIS images in the vicinity of N1851-FUV1 visually. By eye, there appears to be

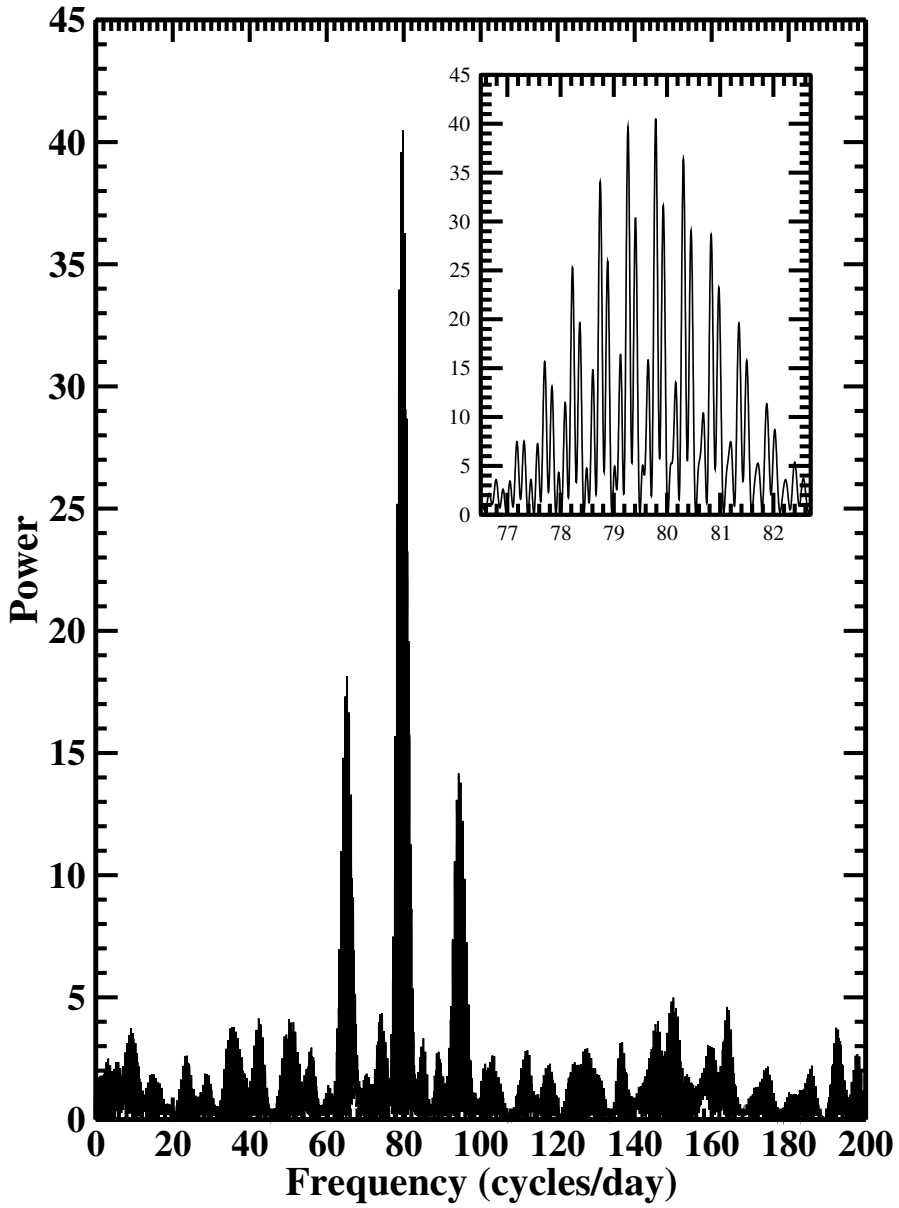

FIGURE 7.4: The power spectrum of the FUV variable source. The central and strongest peak corresponds to 79.79 cycles/day which is 18.05 minutes. The smaller peaks on either side are the aliases of the stronger central peak. The inset shows a magnification of the strongest peak. The multiple peaks are due to aliasing. The 3 visits were separated by 2 days between visits 1 and 2 and 6 days between visits 2 and 3.

a shift of about 0.3 WFC3/UVIS pixels between the center of flux in the ACS/SBC image and the WFC3/UVIS images. Thus, overall, there is at least circumstantial evidence to indicate that N1851-FUV1 is, in fact, a chance superposition.

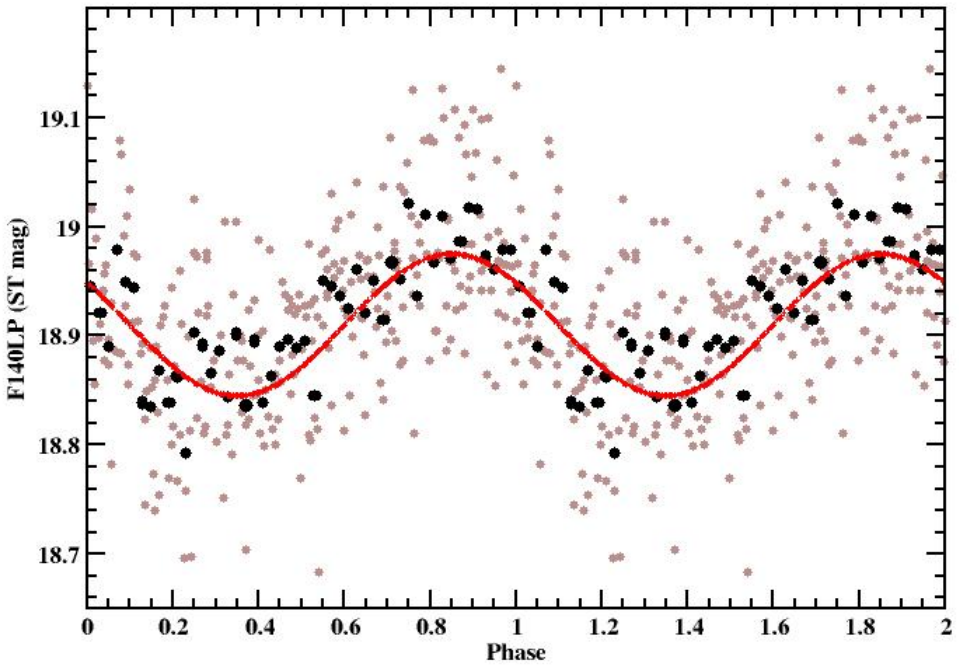

FIGURE 7.5: The phased light curve of the FUV variable source. The data between the phase of 0 and 1 is duplicated between phases 1 and 2. The data has been phased around the 18.05 minute period. All 273 individual measurements are plotted as the faint dots. The black solid dots are the average values in phase bins of 0.02. A sine wave with an amplitude of ~ 0.06 mag has been fit to the data to guide the eye.

7.2.2 Time-Resolved Far-Ultraviolet Photometry

The ACS/SBC data are well suited to a search for short timescale variations among the far-UV sources. A full discussion of all far-UV variable sources will be presented in a future paper (Zurek et al., in prep). There were 273 90-second exposures taken over 3 visits of 4 HST orbits (a total of 12 orbits), spanning about 8 days from the first visit to the third. The second visit was taken 2 days after the first visit, with the third taking place another 6 days later.

The fractional RMS variability for N1851-FUV1 is small ($< 5\%$), and the star was not initially classified as a variable on this basis. However, we also carried out a search for periodic variability for all the bright sources, by calculating the Lomb-Scargle power spectrum for their light curves. The power spectrum for N1851-FUV1 is shown in Figure 7.4 and reveals a clear signal at $f = 79.79$ d^{-1}. This corresponds to a period of $P = 18.05$ min. The far-UV light curve phased on this period is shown in Figure 7.5; for comparison, we also show a simple sinusoid with 0.06 mag amplitude. The precision

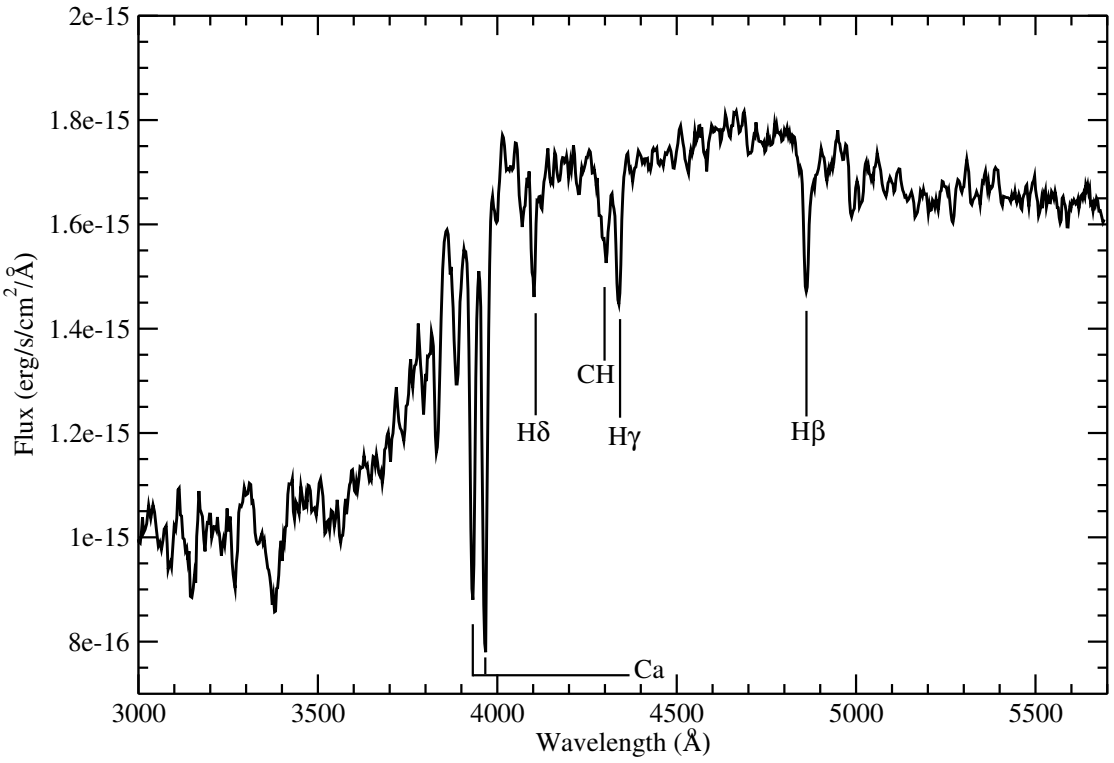

FIGURE 7.6: The HST/STIS/G430L spectra of N1851-FUV1. We have indicated the Hβ, Hγ, and Hδ which are all in absorption. There is clearly no optical emission lines visible. The absorption feature CH also known as the g-band is a clear indication of the temperature as this feature is only seen in stars of spectral types G and K.

of our period estimate is limited to about 0.1 minutes because of aliasing (see inset of Figure 7.4).

We checked all other bright far-UV sources, but found none with the same period. This argues against an instrumental origin of the signal. The ultra-compact X-ray binary (4U 0513-40) has a 17-minute period (Zurek et al. 2010), but is located $\sim$ 6.6 arcseconds from this source (about 150 times the full-width-half-maximum of the PSF).

7.2.3 Optical Spectroscopy

In order to test whether the hot and cool components contributing to the colours of N1851-FUV1 are physically related, we obtained an optical spectrum of N1851-FUV1 with the STIS/CCD/G430L instrument/detector/grating combination on HST. If the system is a close binary consisting of a hot WD and a cool giant, the giant's wind will be irradiated by the ionizing flux of the WD. This should produce extremely strong emission lines (such as [OIII] and the Balmer recombination lines; Kenyon 1990), as is seen, for example, in essentially all symbiotic binaries (Munari & Zwitter 2002). The classification of a symbiotic binary depends on the detection of emission lines (Kenyon 1990; Mikolajewska 2003) and the most common emission lines would be within the

spectral region covered in Figure 7.6. In such a symbiotic scenario, the $\simeq$ 18 min signal would have to be associated with the spin period of an accreting magnetic WD.

However, the spectrum, shown in Figure 7.6, clearly lacks any emission lines. If emission lines existed as in typical symbiotic binaries (Munari & Zwitter 2002) we would have easily detected them. Instead, the spectrum is consistent with the expected SED of a single, cool star with $T_{\rm eff} \simeq 5200$ K. We do note that a few symbiotic binaries have been seen to enter a quiescent period where the emission lines are absent or very weak (Munari & Zwitter 2002), indicating a change in the system. We therefore conclude that the absence of emission lines in our data does not entirely preclude a symbiotic nature for the system, but certainly means that we cannot classify it as such.

7.2.4 X-ray

The Chandra X-ray Observatory (CXO) observed NGC 1851 on three occasions. First, on 2008 Apr 04 for an exposure time of 18.8 ks (ObsID 8966); second, on 2015 Feb 04, for an exposure time of 19.8 ks (ObsID 15735); and third, on 2015 Feb 07, for an exposure time of 27.7 ks. The total combined exposure time was just over 66 ks.

All data were taken in timed exposure mode with the aimpoint on the ACIS S3 chip and telemetered in "Very Faint" mode. We reprocessed all of the data with the Chandra Interactive Analysis of Observations (CIAO) software version 4.5 (Fruscione et al 2006) using the latest calibration files (CALDB 4.5.5.1). Periods of background flaring were searched for, but none were found.

N1851-FUV1 is located $\simeq 10''$ from the bright X-ray source 4U 0513−40 and $\simeq 1.5''$ from one of the brighter of the low-luminosity X-ray sources in the globular cluster. We therefore applied the subpixel event repositioning (SER) algorithm of Li et al (2004) and considered only split-pixel events, i.e. events whose charge clouds that were spread over multiple pixels. Such events can be located more precisely than single-pixel events. This improves the already sharp angular resolution of Chandra at the cost of $\simeq 25\%$ of the total counts.

We estimated the number of X-ray photons that may be associated with N1851-FUV1 by counting all events in the energy range 0.5 keV - 6.0 keV within a $0.5''$ radius aperture centered on its expected location. For this purpose, the X-ray images were registered onto the optical/UV frames by a simple boresight correction determined from 3 bright X-ray sources with optical/UV counterparts. We then estimated the expected number of background events in this aperture by placing identical apertures at roughly the same distance from 4U 0513−40, while also avoiding other real X-ray sources. We find no evidence for a statistically significant excess associated with N1851-FUV1 in any of the three individual images, nor in the combined data. Specifically, our best estimate for the excess number of counts in the combined data is 6.8 ± 4.6.

The absence of X-ray emission is primarily a constraint on the IP scenario for N1851-FUV1. We therefore assume a 15 keV bremsstrahlung model (e.g. Patterson 1994) to convert our measured count rate into an upper limit on the X-ray luminosity of the system. Adopting a cluster distance of $d = 12.1$ kpc and a foreground neutral hydrogen column $N_H = 4 \times 10^{20}$ cm^{-2}, we obtain 3-σ upper limits on the unabsorbed X-ray luminosity of $L_{X,0.5-6} < 5 \times 10^{31}$ erg s^{-1} (between 0.5 keV and 6 keV) or, equivalently, $L_{X,2-10} < 5 \times 10^{31}$ erg s^{-1} (between 2 keV and 10 keV). The corresponding limit on the bolometric X-ray luminosity is $L_{X,bol} < 10^{32}$ erg s^{-1}.

7.3 Discussion

Our analysis of all of the available observations of N1851-FUV1 has led to the following set of constraints on the system:

- N1851-FUV1 is a bright far-UV source in the cluster core that exhibits periodic variability with P = 18.05 min and an amplitude of $\simeq 6\%$;
- its position matches that of a star on the red or asymptotic giant branch in the cluster, but there is a non-negligible possibility that this match is the result of a chance superposition of two unrelated objects;
- its optical spectrum contains no detectable emission lines;
- its X-ray luminosity is $L_{x,2-10} < 5 \times 10^{31}$ erg/s (3σ).

There are only a few classes of UV-bright stars that are capable of producing such a fast periodic signal: ZZ Ceti stars (i.e. pulsating WDs), pulsating subdwarf B stars (sdBs), symbiotic binaries, IPs and AM CVn (accreting double WD) binaries. The symbiotic scenario is the only one in which the blue far-UV and the red optical sources are physically related. However, it is unlikely given the absence of emission lines in the optical spectrum, which are a defining feature of symbiotic systems (Munari & Zwitter 2002). ZZ Ceti stars and sdBs are also ruled out for N1851-FUV1: even a WD near the upper edge of the instability strip (at $T_{WD} \simeq 12,500$ K) would be more than 2 mag fainter than observed and a pulsating sdB would be ~ 3 magnitudes brighter in F140LP as it would be among the hottest horizontal branch stars (Heber 2009). This leaves only the IP and AM CVn scenarios, which we now discuss in turn. Note that in both of these scenarios, the astrometric match of the UV source to the red giant would probably have to be a chance superposition. If the two objects were physically associated, we would again expect to see optical emission lines due to the photoionization of the giant's envelope (as in the case of symbiotic binaries).

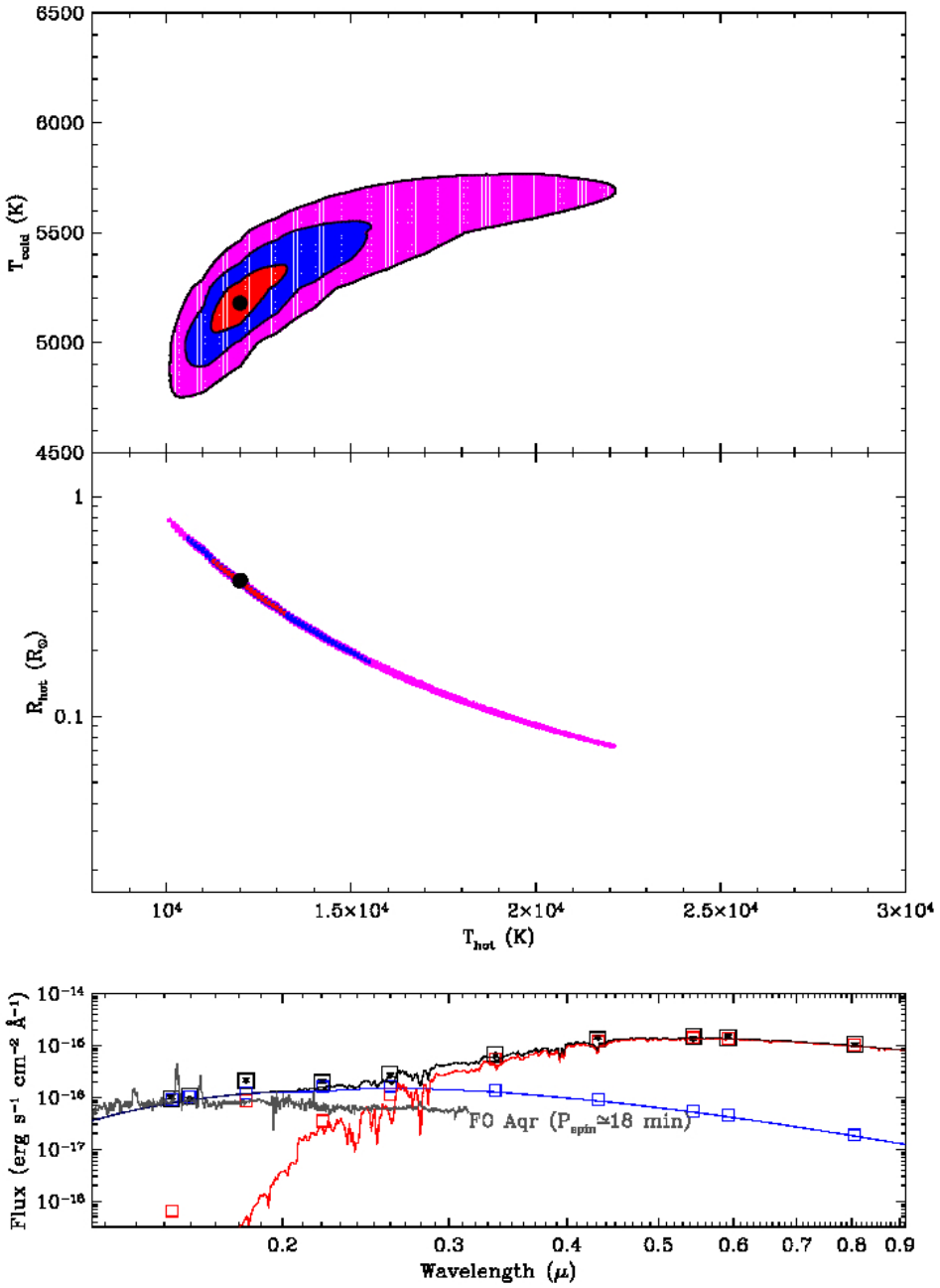

FIGURE 7.7: A two-component model fit to the SED of N1851-FUV1 representing an IP scenario. The cool component is modelled as a stellar model atmosphere, while the hot component is modelled as a blackbody (both components are modelled using SYNPHOT). The top panel shows the best fit (black dot) and 1, 2 and 3 σ contours in the parameter plane defined by the temperature of the cool component and the accretion rate. The middle panel shows the constraints on inclination and accretion rate. In the bottom panel, the predicted spectrum and photometry for the best-fit cool component are shown in red, the predicted spectrum and photometry for the best-fit hot component are shown in red, and the combined best-fit spectrum and photometry are shown in black (solid curves and open squares). The observed photometry for N1851-FUV1 is shown by the black dots (which are mostly located near the center of the black squares). We also show an example blue/ultraviolet spectrum of the IP (FO Aqr), which has a spin period similar to the period of N1851-FUV1.

7.3.1 N1851-FUV1 as an Intermediate Polar

As explained in Section 1, intermediate polars are accreting WD binary systems composed of a Roche-lobe-filling main sequence star and a magnetic WD. In IPs, the accretion onto the WD takes place via an accretion disk that is truncated by the magnetic field of the white dwarf. The gas from the inner edge of the accretion disk is then channelled along field lines onto the magnetic poles of the WD, producing X-ray and UV emission at and near the impact point. Since the rotational and spin axes of the WD are generally not aligned, this emission is modulated on the WD spin period. Both the period and amplitude of the N1851-FUV1's far-UV variability can be explained quite naturally in an IP scenario.

Figure 7.7 shows a fit to the SED of N1851-FUV1, in which the cool component is represented by a model atmosphere with the cluster [Fe/H] (Castelli & Kurucz 2003), and the hot component is modelled as a blackbody. The residuals around this fit are $\simeq 0.09$ mag, and the best fit parameters for the hot component are $T_{hot} \simeq 12,000$ K, $R_{hot} \simeq 0.4\ R_{\odot}$. These are reasonable numbers for the inner accretion flow in an IP. The corresponding parameters for the cool component are $T_{cool} \simeq 5,200$ K, $R_{cool} \simeq 9.5\ R_{\odot}$. Again, these are sensible values for a red giant in NGC 1851. We also show in Figure 7.7 the UV spectrum of FO Aqr, a well-known field IP with a spin period of $P_{spin} \simeq 18$ min, scaled to the distance and reddening of the cluster. This spectrum lies reasonably close to the UV photometry of N1851-FUV1. We conclude that an IP scenario can plausibly explain the UV spectrum and variability of N1851-FUV1.

However, our non-detection of the system in X-rays is a significant challenge to an IP model. As discussed in Section 2.4, adopting a bremsstrahlung X-ray spectrum typical of IPs, this non-detection implies an upper limit of $L_{X,2-10} < 5 \times 10^{31}$ erg s^{-1}. Such a low level of X-ray luminosity is unusual for IPs. This is illustrated in Figure 7.8, which compares the period and X-ray luminosity of N1851-FUV to the spin periods and X-ray luminosities of known field IPs. X-ray fluxes for field IPs were taken from Yuasa et al. (2010), where available, and from Patterson (1994) otherwise. Distances and spin periods were taken from Patterson (1994), where available, and from Pretorius & Mukai (2014 and personal communication) otherwise.

Only three field IPs have X-ray luminosities that may be as low as that of N1851-FUV1, and all of these have extremely short spin periods, $P_{spin} < 100$ seconds. As discussed by Patterson (1994), the X-ray weakness of the fastest rotators may be due to the smaller potential difference between the inner disk edge and the WD surface, as well to a different accretion shock geometry in these systems. Such arguments cannot explain the X-ray weakness of N1851-FUV1, however, given its implied spin period of $P_{spin} \simeq 1080$ seconds.

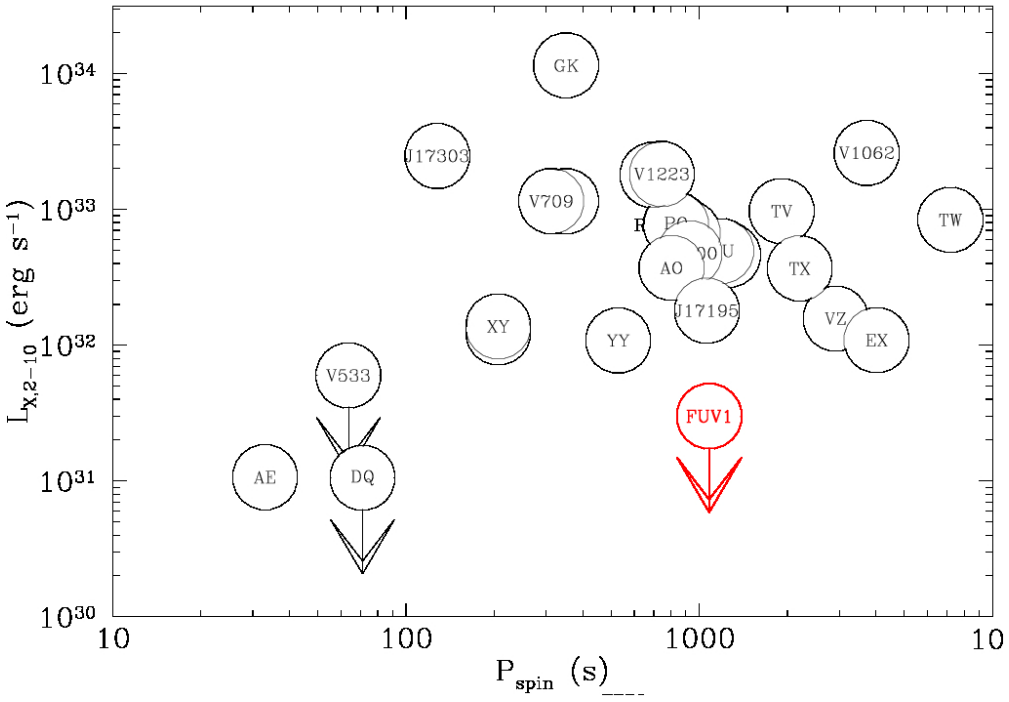

FIGURE 7.8: X-ray luminosity vs white dwarf spin period for the known intermediate polars (Yausa et al 2010; Patterson 1994; Pretorius & Mukai 2014). The X-ray luminosity limit and observed period for N1851-FUV1 are shown in red. It is clearly much less luminous than sources with a comparable period. Sources with a comparable X-ray flux to N1851-FUV1 all have spin periods more than an order of magnitude smaller. The labels in the symbols identify the objects shown (e.g. AE = AE Aqr).

7.3.2 N1851-FUV1 as a double degenerate AM CVn star

AM CVn stars have orbital periods in the range 5 min - 65 min. The period of N1851-FUV1, at $\simeq$ 18 min, lies well within this range. Moreover, in an AM CVn scenario, the lack of an X-ray detection is actually expected, since most of these systems are X-ray weak. This is illustrated in Figure 7.9, which compares the upper limit on $L_{X,bol}$ for N1851-FUV1 with the bolometric X-ray luminosities for a sample of AM CVn stars compiled by Ramsay et al. (2006). All but one of the systems in this sample lie below the upper limit on N1851-FUV1.

The variability amplitude seen in N1851-FUV1 is $\approx$ 0.06 magnitudes. This is about $\sim$ 10 times larger than that of the orbital signal seen in optical light curves of HP Lib, an AM CVn star with a similar orbital period of $P_{orb} \simeq$ 18 min (Patterson et al 2002; Roelofs et al 2007). However, HP Lib also displays "superhumps", which are thought to be associated with an eccentricity of the accretion disk. The superhump period, P_{sh} is only a few percent longer than P_{orb}, but the amplitude of this signal in HP Lib is much larger, at least 0.03 mag. (Patterson et al 2002). Similarly, AM CVn itself has an orbital period of $P_{orb} \simeq$ 17.5 min and displays optical variability amplitudes of $\simeq$ 0.005

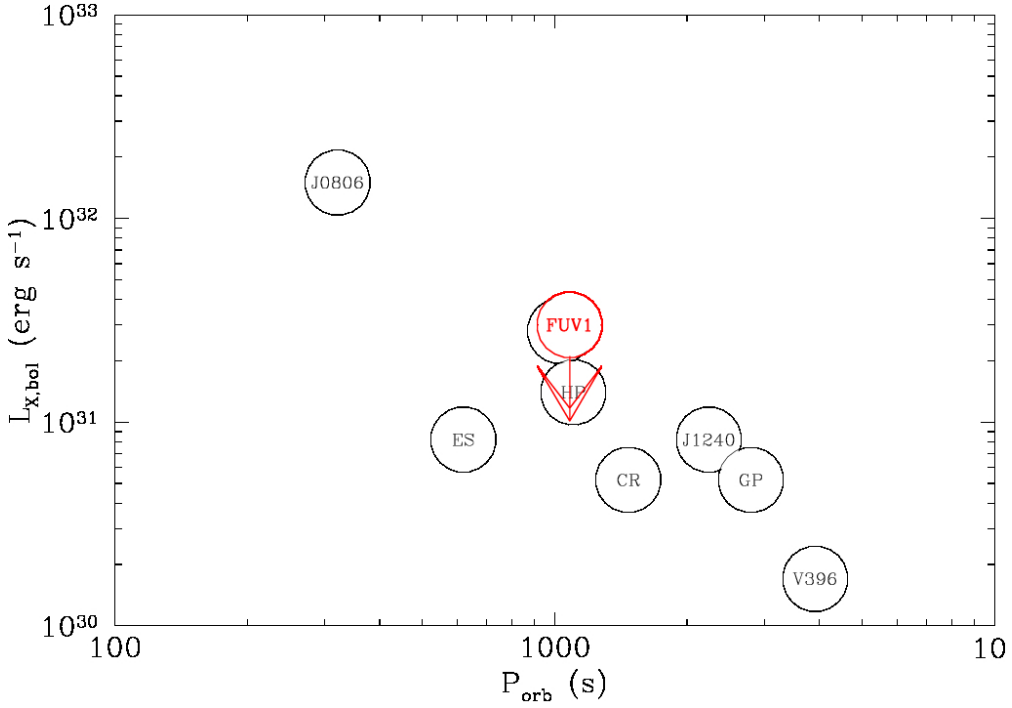

FIGURE 7.9: X-ray luminosity vs orbital period for known AM CVn binarys (Ramsay et al 2014). The X-ray luminosity limit and observed period for N1851-FUV1 are shown in red. The position of N1851-FUV1 is consistent with the location of known AM CVn in this diagram. The labels in the symbols identify the objects shown (e.g. ES = ES Cet).

mag on P_{orb} and $\sim$ 0.01 mag on P_{sh} (Skillman et al. 1999). In the slightly longer period system CP Eri ($P_{orb} \simeq 28.6$ min), the superhump signal has an amplitude in excess of $\sim$ 0.1 magnitudes (Armstrong et al. 2012). If N1851-FUV1 is an AM CVn star, this suggests that the 18-min signal we have detected might actually be due to superhumps, rather than to a true orbital signal. It is also worth noting, however, that the variability amplitudes tend to increase towards the blue. For example, AM CVn's variability amplitude rises to $\sim$ 0.03 in the FUV (Solheim et al 1997), and multi-channel optical observations of the ultra-short period system ES Ceti ($P_{orb} \simeq 10$ min) with ULTRACM also show larger amplitudes at shorter wavelengths (Copperwheat et al. 2011). We therefore conclude that the amplitude of the 18-min signal in N1851-FUV is compatible with an AM CVn interpretation.

The AM CVn model is also consistent with the UV flux and the overall SED of N1851-FUV1. This is illustrated in Figure 7.10, which again shows a two-component model fit to the SED. We once again fit the cool component with the stellar model atmosphere spectrum appropriate for a red giant, but the hot component is now described by a multi-temperature blackbody disk. For the purpose of this fit, the disk is assumed to asymptotically follow the standard $T_{eff} \propto R^{-3/4}$ effective temperature distribution, the accreting WD is assumed to have a mass of $M_1 = 0.7\ M_\odot$ and a radius of $R_1 =$

8×10^8 cm, the mass ratio is taken to be $q = M_2/M_1 = 0.1$, and the accretion disk is assumed to extend all the way to the last non-intersecting orbit around the accretor, $R_{d/a} = 0.6/(1 + q)$ (Warner 1995). The inclination of the disk with respect to the observer is a free parameter in this model, subject to the constraint that $\cos i < 1$. The best fit parameters for the cool component in this case are given by $T_{cool} \simeq 5700$ K and $R_{cool} \simeq 7.6\ R_\odot$. The best-fitting disk parameters are $\dot{M}_{acc} \simeq 10^{-9}\ M_\odot\ yr^{-1}$ and $\cos i \simeq 1$. With residuals of $\simeq 0.12$ mag, formally, this fit is slightly worse than that shown in Figure 7.7, in which the hot component was a single temperature blackbody. However, both residuals are comparable to the level of variability seen in the UV data.

We also show Figure 7.10 the UV spectrum of HP Lib, a well-known AM CVn star with an orbital period of $P_{orb} \simeq 18$ min. Again, this lies quite close to the data in the FUV and also to our model for the hot component. We therefore conclude that the AM CVn model is a viable explanation for N1851-FUV1: it accounts for the 18 min periodic signal, the UV flux level and spectrum, and for the overall SED (albeit by invoking a chance superposition with a red giant to explain the cool component that dominates in the optical region). Unlike the IP scenario, it also naturally accounts for the X-ray weakness of the system. Based on all this, the AM CVn scenario is our preferred interpretation for N1851-FUV1.

7.4 Conclusion

We have presented the discovery N1851-FUV1, an 18 min FUV variable star in the globular cluster NGC 1851. The position of this hot FUV source coincides with a star on the red or asymptotic giant branch in the optical region. However, there is a non-negligible chance that this astrometric match could be the result of a chance superposition. An optical spectrum shows none of the emission lines that might be expected if the two components were physically associated. This makes the obvious interpretation of N1851-FUV1 as a symbiotic star in the cluster unlikely.

If the cool component is unrelated to N1851-FUV1, there are two other obvious interpretations. First, the system may be an IP, i.e. an accreting magnetic WD that is fed by a Roche-lobe-filling main sequence donor star. In this scenario, the 18 min periodic signal represents the spin period of the WD. Second, the system may be an AM CVn star, i.e. a double degenerate interacting binary in which both the accretor and the donor are WDs. In this case, the 18 min signal is the orbital period of the system.

Both the IP and AM CVn models can account for the observed periodic signal, the UV flux level and the overall SED of the system. However, no X-rays are detected from N1851-FUV1 in $\simeq 66$ ksec of exposure with *Chandra*, which implies $L_{X,2-10} < 5 \times 10^{31}$ erg s^{-1}. This is inconsistent with the observed X-ray luminosities of field IPs with comparable spin periods. It is, however, consistent with the X-ray luminosities

of field AM CVn stars. Based on this, we favour the latter scenario for N1851-FUV1, making it the first strong AM CVn candidate known in any globular cluster.

In order to discriminate definitively between the IP and AM CVn models, a FUV spectrum is required. If N1851-FUV1 is an IP, the C IV and He II lines will be preferentially formed in the optically thin accretion curtain surrounding the WD and will therefore be in emission. By contrast, the same transitions will be in absorption if the system is an AM CVn star, since in this case the lines will be formed in the optically thick disk. The presence or absence of a strong Ly α feature would, of course, also favour the IP or AM CVn scenario, respectively.

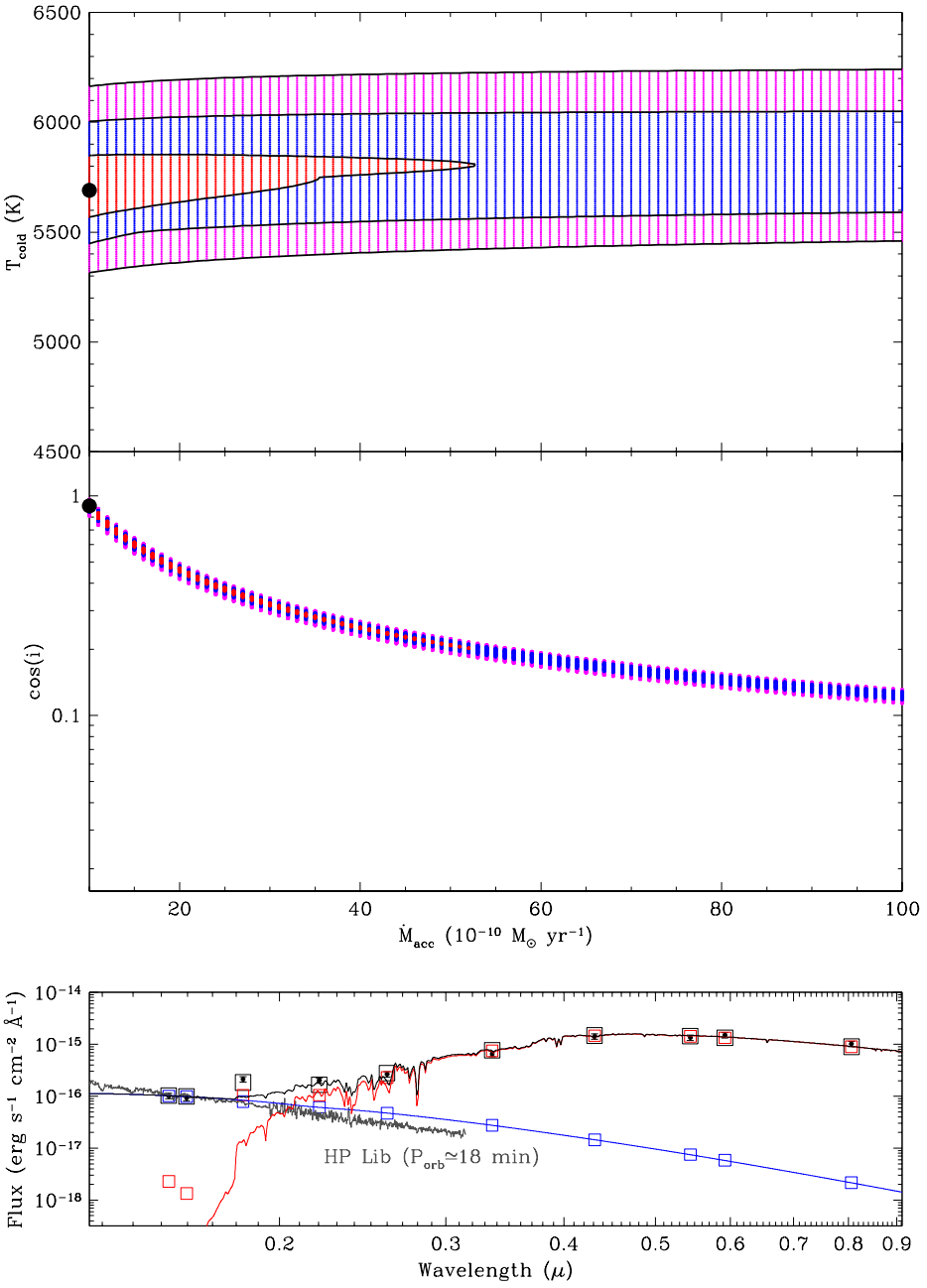

FIGURE 7.10: A two-component model fit to the SED of N1851-FUV1 representing the AM CVn scenario. The cool component is modelled as a stellar model atmosphere, while the hot component is assumed to arise from a multi-temperature accretion disk that locally emits as a blackbody. The top panel shows the best fit (black dot) and 1, 2 and 3 σ contours in the parameter plane defined by the temperature of the cool component and the accretion rate. The middle panel shows the constraints on inclination and accretion rate. In the bottom panel, the predicted spectrum and photometry for the best-fit cool component are shown in red, the predicted spectrum and photometry for the best-fit hot component are shown in red, and the combined best-fit spectrum and photometry are shown in black (solid curves and open squares). The observed photometry for N1851-FUV1 is shown by the black dots (which are mostly located near the center of the black squares). We also show an example blue/ultraviolet spectrum of an AM CVn (HP Lib) with an orbital period similar to the period of N1851-FUV1.

Chapter 8

Conclusions

The stellar densities in a globular cluster is orders of magnitude higher than the field. This greatly increases interactions between stars and binaries. In addition, mass segregation means that the more massive objects tend to migrate to the cluster center and the lowest mass objects migrate to the cluster outskirts (see Chapter 1). Interactions with binaries typically result in binaries with a smaller separation and a third star with added kinetic energy (Portegies Zwart, et al 1997).

The stellar dynamics in GCs, and the associated star-star, binary-star, and binary-binary interactions increases the number of "exotic" objects (Di Stefano & Rappaport 1994). The increase in stellar exotica has been observed among low mass X-ray binaries (Bahramian et al. 2013) and blue stragglers (Knigge et al. 2009). Cataclysmic variables, on the other hand, have not been observed to be enhanced in GCs though predictions (Ivanova et al. 2006) suggest that they should be. In this thesis I have attempted to identify stellar exotica in the two GCs NGC 1851 and NGC 6681.

8.1 NGC 1851

The photometric analysis of far-ultraviolet and optical imaging data for NGC 1851 (Chapter 4) has allowed us to distinguish several key stellar populations. The primary tool in this analysis was the colour-colour diagram (Figure 4.1), which can be divided into 5 distinct regions that contain different populations: (1) main sequence and evolved cool stars, (2) hot horizontal branch and blue straggler stars, (3) UV excess main sequence stars, (4) optically blue sources, and (5) optically red sources.

Interestingly, the classification of objects in the blue straggler region of the CMDs (Figure 4.3 and Figure 4.5) can depend on the wavelengths being considered. For example, the blue straggler stars highlighted in Figure 4.3 can be clearly defined as blue straggler stars in both the optical and ultraviolet. However, the highlighted sources in Figure 4.5

lie on the main sequence in the optical CMD (with 4 exceptions discussed in Chapter Chapter 4), while in the ultraviolet CMD they are distributed to the blue of the main sequence. Some of these sources are in or near the blue straggler area in the ultraviolet CMD and could be classified as blue stragglers on this basis. These ultraviolet-excess blue stragglers likely have a hot companion, which is consistent with similar findings by Gosnell et al (2014) for blue stragglers in open clusters. More specifically, the ultraviolet-excess blue straggler are likely binary systems composed of a (near-)main sequence star with a hot white dwarf companion. Some or all of these systems may be transferring mass, in which case, they would be considered cataclysmic variables. Additional observations (e.g. spectroscopy) are required to test this idea.

I have discovered 36 candidate variables in NGC 1851, distributed across three different parts of the cluster CMD (Figure 5.2): the horizontal branch (both red [RR Lyrae] and blue), the blue straggler region, and the white dwarf sequence (in the ultraviolet). It is likely that 12 of the variable candidates on the horizontal branch are RR Lyrae stars. Their phased light curves generally have saw tooth shapes (Figure 5.3, Figure 5.4, and, Figure 5.5), which is typical of RR Lyraes. Also, their positions in both optical and ultraviolet CMD are in locations consistent with RR Lyraes. The two exceptions, **FUV2** and **FUV12**, also exhibit the distinctive saw-tooth shape in their phased light curves (Figure 5.3 and Figure 5.5 respectively), but **FUV2** is about a magnitude brighter in the optical than the locus of the red horizontal branch, while **FUV12** lies redward of the red giant branch in the optical CMD (Figure 5.2). **FUV2**'s properties might be consistent with an evolved horizontal branch star that lies in the instability strip. However, such systems should be rare, since the time a star spends in this CMD location (Figure 5.2) is about 100 times shorter than the time it spends on the horizontal branch. The other exception, **FUV12**, is located in a region of the optical CMD (Figure 5.2) that also contains the mysterious "red stragglers" (Geller et al. 2017). However, I cannot explain the saw tooth shape of the phased light curve if the source is a red straggler, as this places it well outside the instability strip in the optical. Additional scrutiny of this object at more wavelengths is needed to gain a better understanding of this source.

I have also found 13 variable candidates in NGC 1851 that are located on the blue horizontal branch in the cluster CMD. The amplitude of the variations observed among the 13 candidates is as small as ~ 0.03 magnitudes, which is about twice the uncertainty of the individual photometric measurements in the far-ultraviolet band. These objects may be the globular cluster counterparts of the pulsating sub-dwarf B stars recently discovered in the Galactic field. Additional observations, such as spectroscopy or additional Hubble Space Telescope imaging (data in other filters and/or time series with longer durations and/or better cadence) is strongly encouraged in order to test this hypothesis.

Five of the far-ultraviolet variable candidates in NGC 1851 can be identified as blue stragglers, based on their positions in the CMDs (Figure 5.2). The shortest period system (**FUV14**; $P \approx 109$ minutes), has a very similar phased light curve shape to

that seen in RR Lyrae variables. This suggests that, as in RR Lyraes, the variability is due to pulsations. And indeed, the observed period of the variations is consistent with expectations for SX Phoenicis pulsators. However, there remains some uncertainty regarding the period and/or nature of the sources, since the phased light curve is not smooth, especially at maximum. The other four blue straggler variable candidates have light curves which may indicate they are binaries. If so, this would be an important clue to the dominant formation mechanism of blue stragglers in globular clusters.

I have also discovered 6 variable candidates in NGC 1851 whose photometric properties place them on or near the main sequence in the optical, but blueward of the main sequence in the ultraviolet (Figure 5.2). This is the region where I expect to find white dwarf + main sequence binaries. In one case (**FUV20**), the phased light curve again exhibits the saw-tooth shape that is typical of pulsating variables (such as RR Lyrae stars or **FUV14**). However, the period of ~ 7 hours I estimate for this source is long for an SX Phoenicis variable. It is tempting to suggest that it is a background RR Lyrae star, but this would place the variable at ~ 100 kpc, which is very much at the extreme end of what is considered the Galactic halo. The nature of this source is therefore currently still unclear. The other 5 apparent white dwarf + main sequence binaries are, of course, also worth following up. Are they short-period, perhaps even post-common-envelope systems? Are they perhaps even mass-transferring systems (i.e. cataclysmic variables)? Additional time-series and/or spectroscopic observations will be required to confidently answer these questions.

Finally, the most intriguing far-ultraviolet variable I have discovered in NGC 1851 – **FUV1** – exhibits a clear 18 min periodic signal, yet has photometric properties that seem consistent with those expected for symbiotic binaries. Specifically, its broad-band colours are those of a binary containing a hot white dwarf and a cool star on the (red or asymptotic) giant branch. However, I have obtained an optical spectrum from Hubble Space Telescope using the Space Telescope Imaging Spectrograph, which did not exhibit the emission lines that would be expected if the system is a symbiotic binary. Detailed investigation of the imaging observations (see Chapter 7) suggests that the sources dominating in the blue and the red may actually be unrelated; it is possible that a chance superposition between an asymptotic giant branch star and another hot component is being observed. The 18 min periodicity seen in the far-ultraviolet source is, of course, nevertheless important and demands an interpretation. Imaging with Chandra places stringent limits on the X-ray luminosity of the source, which makes it unlikely that it is a magnetic cataclysmic variable of the intermediate polar type. I therefore suggest that the most likely interpretation for this source is as an AM CVn system, i.e. a mass-transferring double-degenerate binary. Given that the mass-losing donor star in such systems is Hydrogen-deficient, this scenario can be confirmed with far-ultraviolet spectroscopy. If the system is an AM Cvn, there should be no significant intrinsic Lyman-α feature. If such a feature is detected, an intermediate polar interpretation is favoured

despite the unusual X-ray faintness of the source in this scenario. I plan to submit a Hubble Space Telescope proposal during the next cycle to obtain this far ultraviolet spectrum.

8.2 NGC 6681

Dwarf novae are a sub-class of disk-accreting cataclysmic variables that are subject to a disk instability (Mineshige & Osaki 1983). The recurrence time of dwarf nova eruptions can be anywhere from weeks to decades, the outbursts last from days to months, and during outburst the brightness of the system can increase by $3-6$ magnitudes in the optical (see Chapter 6 for more details). I conducted a dwarf nova search of globular cluster NGC 6681 using archival/calibration data taken over ~ 20 years with the far-ultraviolet imaging cameras (Advanced Camera for Surveys/ Solar Blind Channel and Space Telescope Imaging Spectrograph) onboard the Hubble Space Telescope. No such eruptions were found.

The data set for NGC 6681 consists of 80 epochs, of which 47 are spaced more than 1 month apart. If all 80 epochs are considered to be independent, the survey would be essentially 100% complete for dwarf novae with duty cycles $\gtrsim 5\%$, and 60% complete for systems with duty cycles of 1%. Even in a more pessimistic scenario where only 47 epochs are independent, it is still $\gtrsim 99\%$ complete for duty cycles $\gtrsim 10\%$ and $\approx 35\%$ for duty cycles of 1%. In fact, the detection efficiency remains a respectable 13% even for duty cycles as low as 0.3% (as in WZ Sge).

The non-detection of any eruptions therefore places strong constraints on models for the formation of cataclysmic variables in globular clusters. Such models routinely predict the presence of ~ 100 such systems in dense globular clusters, created from primordial binaries, via tidal capture events and/or via 3-body encounters (Di Stefano & Rappaport 1994). Even if most or all cataclysmic variables in globular clusters are faint, low-$\dot{M}$, rarely erupting systems like WZ Sge – as is theoretically expected, in fact – the null result implies that there are likely fewer than ~ 20 such systems in NGC 6681. This limit is in significant tension with theoretical predictions.

8.3 Final Thoughts

The far-ultraviolet, when matched with other wavelengths, is excellent at identifying sources with a hot component. For example, sources which are on the main sequence in an optical CMD but lie to the blue of the main sequence in a FUV CMD. These sources are best explained by a two component system, where one component is a cool main

sequence star and the other is hot white dwarf. These systems are CV candidates but additional information, such as emission lines or variability, is required.

In this thesis I have identified 36 variable candidates using high cadence FUV observations of NGC 1851. These variable candidates are located on the horizontal branch, extended main sequence (i.e. blue straggler region), and where I expect CVs to populate the CMD. Many of these variable candidates require additional information, such as observations with a different cadence, to confirm the variability. The variable candidates, that also have FUV colours that places them where CVs should be in a CMD, require the identification of emission lines to confirm an identification as a CV.

The search for variability on much longer timescales (i.e. months to years) is useful in finding dwarf novae or putting limits on their numbers. I found no dwarf novae in the center of NGC 6681 which places significant limits on their total numbers in this cluster. NGC 6681 is the only cluster that such an extensive dataset exists for, though smaller datasets exist for other clusters. An analysis of all the smaller datasets may provide useful limits for the GC system as a whole.

The Hubble Space Telescope is approaching its end of life in about 6 to 7 years. If additional FUV studies, both photometric and time series, of GC cores are going to happen they need to be proposed for in the next observing cycles. Once the Hubble Space Telescope ceases function it may be many years before another space telescope with the required capabilities, resolution and far-ultraviolet wavelength coverage, is approved and launched.

Chapter 9

Bibliography

Anderson, J., Sarajedini, A., Bedin, L.R., King, I.R., Piotto, G., Reid, I.N., Siegel, M., Majewski, S.R., Paust, N.E.Q., Aparicio, A., Milone, A.P., Chaboyer, B., & Rosenberg, A. 2008, AJ, 135, 2055

Anderson, J., Piotto, G., King, I.R., Bedin, L.R., & Guhathakurta, P. 2009, ApJL, 697, 58

Archibald, A. M., Stairs, I. H., Ransom, S. M., Kaspi, V. M., Kondratiev, V. I., Lorimer, D. R., McLaughlin, M. A., Boyles, J., Hessels, J. W. T., Lynch, R., van Leeuwen, J., Roberts, M. S. E., Jenet, F., Champion, D. J., Rosen, R., Barlow, B. N., Dunlap, B. H., & Remillard, R. A. 2009, Science, 324, 1411

Armstrong, E., Patterson, J., & Kemp, J. 2012, MNRAS, 421, 2310

Avila, R., et al. 2017, "ACS Instrument Handbook", Version 16.0 (Baltimore: STScI)

Bahramian, A., Heinke, C.O., Sivakoff, G.R., & Gladstone, J.C. 2013, ApJ, 766, 136

Bailyn, C.D. 1995, ARA& A, 33, 133

Baker, N. & Kippenhahn, R. 1962, ZA, 53, 114

Balona, L.A., Svanda, M., & Karlicky, M. 2016, MNRAS, 463, 1740

Bedin, L.R., Piotto, G., Anderson, J., Cassisi, S., King, I.R., Momany, Y., & Carraro, G. 2004, ApJL, 605, 125

Bellini, A., Anderson, J., van der Marel, R. P., Watkins, L. L., King, I. R., Bianchini, P., Chaname, J., Chandar, R., Cool, A. M., Ferraro, F. R., Ford, H., & Massari, D. 2014, ApJ, 797, 115

Bellini, A., Anderson, J., Bedin, L. R., King, I. R., van der Marel, R. P., Piotto, G., & Cool, A. 2017, ApJ, 842, 6

Belloni, D., Giersz, M., Askar, A., Leigh, N., & Hypki, A. 2016, MNRAS, 462, 2950

Bergbusch, P.A. 1993, AJ, 106, 1024

Benacquista, M.J. & Downing, J.M.B. 2013, Living Reviews in Relativity, Vol. 16

Bildsten, L., Shen, K.J., Weinberg, N.N., & Nelemans, G. 2007, ApJL, 662, 95

Braga, V.F., Stetson, P.B., Bono, G., Dall'Ora, M., Ferraro, I., Florentino, G., Freyhammer, L.M., Iannicola, G., Marengo, M., Neeley, J., Valenti, E., Buonanno, R., Calamida,

A., Castellani, M., de Silva, R., DegI'Innocenti, S., Di Cecco, A., Fabrizio, M., Freedman, W.L., Giuffrida, G., Lub, J., Madore, B.F., Marconi, M., Marinoni, S., Matsunaga, N., Monelli, M., Persson, S.E., Piersimoni, A.M., Pietrinferni, A., Prada-Moroni, P., Pulone, L., Stellingwerf, R., Tognelli, E., & Walker, A.R. 2016, AJ, 152, 170

Brocato, E., Buonanno, R., Malakhova, Y., & Piersimoni, A. M. 1996, A & A, 311, 778

Brooks, J. Bildsten, L., Marchant, P., & Paxton, B. 2015, ApJ, 807, 74

Brown, T.M., Sweigart, A.V., Lanz, T., Smith, E., Landsman, W.B., & Hubeny, I. 2010, ApJ, 718, 1332

Brown, T.M., Landsman, W.B., Randall, S.K., Sweigart, A.V., & Lanz, T. 2013, ApJL, 777, 22

Cadelano, M., Dalessandro, E., Ferraro, F. R., Miocchi, P., Lanzoni, B., Pallanca, C., & Massari, D. 2017, ApJ, 836, 170

Caloi, V., Castellani, V., Galluccio, D., & Wamsteker, W. 1984, A & A, 138, 485

Cartwright, T.F., Engel, M.C., Heinke, C.O., Sivakoff, G.R., Berger, J.J., Gladstone, J.C., & Ivanova, N. 2013, ApJ, 768, 183

Castelli, F. & Kurucz, R.L. 2003, IAUS, 210, A20

Camilo, F. & Rasio, F.A. 2005, ASPC, 328, 147

Cash, W. 1979, ApJ, 228, 939

Chatterjee, S., Rasio, F.A., Sills, A., & Glebbeck, E. 2013, ApJ, 777, 106

Chomiuk, L., Stradder, J., Maccarone, T.J., Miller-Jones, J.C.A., Heinke, C., Noyola, E., Seth, A.C., & Ransom, S. 2013, ApJ, 777, 69

Clark, G.W. 1975, ApJL, 199, 143

Cohn, H. N., Lugger, P. M., Couch, S. M., Anderson, J., Cool, A. M., van den Berg, M., Bogdanov, S., Heinke, C. O., & Grindlay, J. E. 2010, ApJ, 722, 20

Cool, A.M., Grindlay, J.E., Cohn, H.N., Lugger, P.M., & Bailyn, C.D. 1998, ApJL, 508, 75

Coppejans, D.L., Kording, E.G., Knigge, C., Pretorius, M.L., Woudt, P.A., Groot, P.J., Van Eck, C.L., & Drake, A.J. 2016, MNRAS, 456, 4441

Copperwheat, C.M., Morales-Rueda, L., Marsh, T.R., Maxted, P.F.L., & Heber, U. 2011, MNRAS, 415, 1381

Corsico, A.H., Althaus, L.G., Serenelli, A.M., Kepler, S.O., Jeffery, C.S., & Corti, M.A. 2016, A& A, 588, 74

Corwin, T. M., Catelan, M., Borissova, J., & Smith, H. A. 2004, A & A, 421, 667

Cropper, M. 1990, Space Science Reviews, 54, 195

D'Antona, F., Vesperini, E., D'Ercole, A., Ventura, P., Milone, A. P., Marino, A. F., & Tailo, M. 2016, MNRAS, 458, 2122

Davies, M.B. 1997, MNRAS, 288, 117

Dieball, A., Knigge, C., Zurek, D. R., Shara, M. M., & Long, K. S. 2005, ApJ, 625, 156

Dieball, A., Knigge, C., Zurek, D. R., Shara, M. M., Long, K. S., Charles, P. A., Hannikainen, D. C., & van Zyl, L. 2005, ApJL, 634, 105

Dieball, A., Knigge, C., Zurek, D. R., Shara, M. M., Long, K. S., Charles, P. A., &

Hannikainen, D. C., 2007, ApJ, 670, 379
Dieball, A., Long, K. S., Knigge, C., Thomson, G. S., Zurek, D. R. 2010, ApJ, 710, 332
Dieball, A., Rasekh, A., Knigge, C., Shara, M., & Zurek, D. 2017, MNRAS, 469, 267
Dickey, J. M., & Lockman, F. J. 1990, ARAA, 28, 215
Di Stefano, R., & Rappaport, S. 1994, ApJ, 423, 274
Dotter, A., Chaboyer, B., Jevremovic, D., Kostov, V., Baron, E. & Ferguson, J.W. 2008, ApJ, 178,89
Durrell, P.R. & Harris, W.E. 1993, AJ, 105, 1420
Edmonds, P.D., Gilliland, R.L., Camilo, F., Heinke, C.O., & Grindlay, J.E. 2002, ApJ, 579, 741
Elliott, P., Bayo, A., Melo, C. H. F., Torres, C. A. O., Sterzik, M., & Quast, G. R. 2014, A & A, 568, 26
Ferraro, F.R. 2008, MmSAI, 79, 600
Ferraro, F.R., Beccari, G., Dalessandro, E., Lanzoni, B., Sills, A., Rood, R.T., Fusi Pecci, F., Karakas, A.I., Miochi, P., & Bovinelli, S. 2009, Nature, 462, 1082
Formiggini, L. & Leibowitz, E.M. 2009, MNRAS, 396, 1507
Freire, P.C.C., Ransom, S.M., & Gupto, Y. 2007, ApJ, 662, 1177
Freire, P.C.C. 2013, IAUS, 291, 243
Fruscione, A., et al. 2006, Proceedings of SPIE, 6270
Galbany, L., Stanishev, V., Mourao, A.M., Rodriques, M., Flores, H., Garcia-Benito, R., Mast, D., Medoza, M.A., Sanchez, S.F., Badenes, C., Barrera-Ballesteros, J., Bland-Hawthorn, J., Falcon-Barroso, J., Garcia-Lorenzo, B., Gomes, J.M., Gonzalez Delgado, R.M., Kehrig, C., Lyubenova, M., Lopez-Sanchez, A.R., de Lorenzo-Caceres, A., Marino, R.A., Meidt, S., Molla, M., Papaderos, P., Perez-Torres, M.A., Rosales-Ortega, F.F., & van den Ven, G. 2014, A& A, 572, 38
Geller, A. M., & Leigh, N. W. C. 2015, ApJL, 808, 25
Geller, A. M., Leiner, E. M., Bellini, A., Gleisinger, R., Haggard, D., Kamann, S., Leigh, N. W. C., Mathieu, R. D., Sills, A., Watkins, L. L., & Zurek, D. 2017, ApJ, 840, 66
Gilliland, R. L., Bono, G., Edmonds, P. D., Caputo, F., Cassisi, S., Petro, L. D., Saha, A., & Shara, M. M. 1998, ApJ, 507, 818
Gil-Pons, P., Suda, T., Fujimoto, M.Y., & Garcia-Berro, E. 2005, A& A, 433, 1037
Gonzaga, S., Hack, W., Fruchter, A., & Mack, J. eds 2012, The DrizzlePac Handbook (Baltimore, STScI)
Gosnell, N.M., Mathieu, R.D., Geller, A.M., Sills, A., Leigh, N., & Knigge, C. 2014, ApJL, 783, 8
Grindlay, J.E., Cool, A.M., Callanan, P.J., Bailyn, C.D., Cohn, H.N., & Lugger, P.M. 1995, ApJL, 455, 47
Grindlay, J. E., Heinke, C. O., Edmonds, P. D., Murray, S. S., & Cool, A. M. 2001, ApJL, 563, 53
Han, M., Chun, S.-H., Choudhury, S., Chiang, H., Lee, S., & Sohn, Y.-J. 2017, JASS, 34, 83

Hansen, B.M.S., Anderson, J., Brewer, J., Dotter, A., Fahlman, G.G., Hurley, J., Kalirai, J., King, I., Reitzel, D., Richer, H.B., Rich, R.M., Shara, M.M., & Stetson, P.B. 2007, ApJ, 671, 380
Harris, W.E. 1982, ApJS, 50,573
Harris, W.E. 1996, AJ, 112, 1487
Heber, U. 2009, ARA & A, 47, 211
Heggie, D.C. 1975, MNRAS, 173, 729
Heggie, D.C., & Rasio, F.A. 1996, MNRAS, 282, 1064
Heinke, C. O., Grindlay, J. E., Lugger, P. M., Cohn, H. N., Edmonds, P. D., Lloyd, D. A., & Cool, A. M. 2003, ApJ, 598, 501
Heinke, C. O., Grindlay, J. E., Edmonds, P. D., Lloyd, D. A., Murray, S. S., Cohn, H. N., & Lugger, P. M. 2003, ApJ, 598, 516
Hills, J.G. 1975, AJ, 80, 809
Hills, J.G., & Day, C.A. 1976, ApJL, 17, 87
Hut, P. & Verbunt, F. 1983, Nature, 301, 587
Iaconi, R., Reichardt, T., Staff, J., De Marco, O., Passy, J.C., Price, D., Wurster, J., & Herwig, F. 2017, MNRAS, 464, 4028
Ibata, R.A., Gilmore, G., & Irwin, M.J. 1994, Nature, 370, 194
Ivanova, N., Belczynski, K., Fregeau, J.M., & Rasio, F.A. 2005, MNRAS, 358, 572
Ivanova, N., Heinke, C. O., Rasio, F. A., Taam, R. E., Belczynski, K., & Fregeau, J. 2006, MNRAS, 372, 1043
Ivanova, N., & Nandez, J.L.A. 2016, MNRAS, 462, 362
Jurcsik, J., Smitola, P., Hajdu, G., Sodo, A., Nuspl, J., Kolenberg, K., Furesz, G., Moor, A., Kun, E., Pal, A., Bakos, J., Kelemen, J., Kovacs, T., Kriskovics, L., Sarneczky, K., Szalai, T., Szing, A., & Vida, K. 2015, ApJS, 216, 25
Kadia, Z. I., Gerashchenko, A. N., & Malakhova, Y. N. 1996, IBVS, 4414, 1
Kadia, Z. I., Gerashchenko, A. N., & Malakhova, Y. N. 1998, A & AT, 15, 137
Kalirai, J.S., Richer, H.B., Anderson, J., Dotter, A., Fahlman, G.G., Hansen, B.M.S., Hurley, J., King, I.R., Reitzel, D., Rich, R.M., Shara, M.M., Stetson, P.B., & Woodley, K.A. 2012, AJ, 143, 11
Kato, M., Hachisu, I., & Henze, M. 2013, ApJ, 779, 19
Katz, J. I. 1975, Nature, 253, 698
Kenyon, S. J. 1990, ASPC, 9, 206
Knigge, C., Zurek, D. R., Shara, M. M., & Long, K. S. 2002, ApJ, 579, 752
Knigge, C., Zurek, D. R., Shara, M. M., Long, K. S., & Gilliland, R. L. 2003, ApJ, 599, 1320
Knigge, C., Dieball, A., Maiz Apellaniz, J., Long, K.S., Zurek, D.R., & Shara, M.M. 2008, ApJ, 683, 1006
Knigge, C., Leigh, N., & Sills, A. 2009, Nature, 457, 288
Knigge, C., Baraffe, I., & Patterson, J. 2011, ApJS, 194, 28
Knigge, C. 2012, MmSAI, 83, 549

Kundu, A., Maccarone, T. J., Zepf, S. E., & Puzia, T. H. 2003, ApJL, 589, 81
Kunder, A., Salaris, M., Cassisi, S., de Propris, R., Walker, A., Stetson, P. B., Catelan, M., & Amigo, P. 2008, Mem.S.A.It., 75, 282
Kurtz, D. W., Bowman, D. M., Ebo, S. J., Moskalik, P., Handberg, R., & Lund, M. N. 2016, MNRAS, 455, 1237
Laidler et al. 2005, "Synphot User's Guide", Version 5.0 (Baltimore: STScI)
Landsman, W. B., Sweigart, A. V., Bohlin, R. C., Neff, S. G., O'Connell, R. W., Roberts, M. S., Smith, A. M., & Stecher, T. P. 1996, ApJL, 472, 93
Leigh, N., & Sills, A. 2010, AIPC, 1314, 120
Leigh, N., & Geller, A. M. 2012, MNRAS, 425, 2369
Lee, Y.S., Beers, T.C., Sivarani, T., Johnson, J.A., An, D., Wilhelm, R., Allende, P.C., Koesterke, L., Re, F.P., Bailer-Jones, C.A.L., Norris, J.E., Yanny, B., Rockosi, C., Newberg, H.J., Cudworth, K.M. Pan, K. 2008, AJ, 136, 2050
Levitan, D., Groot, P.J., Prince, T.A., Kulkarni, S.R., Laher, R., Ofek, E.O., Sesar, B., & Surace, J. 2015, MNRAS, 446, 391
Li, J., Kastner, J. H., Prigozhin, G. Y., Schulz, N. S., Feigelson, E. D., & Getman, K. V. 2004, ApJ, 610, 1204
Liller, M. H. 1983, AJ, 88, 1463
Lomb, N. R. 1976, Ap & SS, 39, 447
Lovisi, L., Mucciarelli,A., Lanzoni, D., Ferraro, F.R., Dalessandro, E., & Monaco, L. 2013, ApJ, 772, 148
Lugger, P. M., Cohn, H. N., & Grindlay, J. E. 1995, ApJ, 439, 191
Lugger, P. M., Cohn, H. N., Cool, A. M., Heinke, C. O., & Anderson, J. 2017, ApJ, 841, 53
Lyne, A.G. 1998, AdSpR, 21, 149
Lyne, A.G., Brinklow, A., Middleditch, J., Kulkarni, S.R. & Backer, D.C. 1987, Nature, 328, 399
Maccarone, T.J., Kundu, A., Zepf, S.E., & Rhode, K.L. 2007, Nature, 445, 183
Magrini, L., Perinotto, M., Corradi, R. L. M., & Mampaso, A. 2003, MmSAI, 74, 482
Margon, B., Downes, R.A., & Gunn, J.E. 1981, ApJL, 247, 89
Massari, D., Bellini, A., Ferraro, F. R., van der Marel, R. P., Anderson, J., Dalessandro, E., & Lanzoni, B. 2013, ApJ, 779, 81
Massari, D., Fiorentino, G., McConnachie, A., Bellini, A., Tolstoy, E., Turri, P., Anderson, D., Bono, G., Stetson, P. B., & Veran, J.-P. 2016 A & A, 595, 2
McDonald, I., Zijlstra, A.A. 2015, MNRAS, 448, 502
McMaster, Biretta, et al. 2008, WFPC2 Instrument Handbook, Version 10.0 (Baltimore: STScI)
Milone, A.P., Bedin, L.R., Piotto, G., Anderson, J., King, I.R., Sarajedini, A., Dotter, A., Chaboyer, B., Marin-Franch, A., Majewski, S., Aparicio, A., Hempel, M., Paust, N.E.Q., Reid, I.N., Rosenberg, A., & Siegel, M. 2008, ApJ, 673, 241
Mikolajewska, J. 2003, ASPC, 303, 9

Milone, A.P., Piotto, G., Bedin, L.R., Cassisi, S., Anderson, J., Marino, A.F., Pietrinferni, A., & Aparicio, A. 2012, A& A, 537, 77
Mineshige, S., & Osaki, Y. 1983, PASJ, 35, 377
Moni Bidin, C., Moehler, S., Piotto, G., Momany, Y., & Recio-Blanco, A. 2009, A& A, 498, 737
Moni Bidin, C., Villanova, S., Piotto, G., & Momany, Y. 2011, A& A, 528, 127
Munari, U. & Zwitter, T. 2002, A&A, 383, 188
Nelemans, G., Portegies Zwart, S.F., Verbunt, F., & Yungelson, L.R. 2001, A&A, 368, 939
O'Malley, E. M., Kniazev, A., McWilliam, A., & Chaboyer, B. 2017, arXiv:1706.06962
Ostensen, R.H., Degroote, P., Telting, J.H., Vos, J., Aerts, C., Jeffery, C.S., Green, F.M., Reed, M.D., & Heber, U. 2012, ApJL, 753, 17
Parker, R. J., & Meyer, M. R. 2014, MNRAS, 442, 3722
Pasquato, M., de Luca, A., Raimondo, G., Carini, R., Moraghan, A., Chung, C., Brocato, E., & Lee, Y.-W. 2014, ApJ, 789, 28
Patterson, J. 1994, PASP, 106, 209
Patterson, J., Fried, R. E., Rea, R., Kemp, J., Espaillat, C., Skillman, D. R., Harvey, D. A., O'Donoghue, D., McCormick, J., Velthuis, F., Walker, S., Retter, A., Lipkin, Y., Butterworth, N., McGee, P., & Cook, L. M. 2002, PASP, 114, 65
Piotto, G., Milone, A.P., Anderson, J., Bedin, L.R., Bellini, A., Cassisi, S., Marino, A.F., Aparicio, A., & Nascimbeni, V. 2012, ApJ, 760, 39
Pooley, D., Lewin, W.H.G, Anderson, S.F., Baumgardt, H., Filippenko, A.V., Gaensler, B.M., Homer, L., Hut, P., Kaspi, V.M., Makino, J., Margon, B., McMillan, S., Portegies Zwart, S., van der Klis, M., & Verbunt, F. 2003, APJL, 591, 131
Pooley, D., & Hut, P. 2006, ApJL, 646, 143
Pooley, D. 2010, PNAS, 107, 7164
Press, W.H., & Rybicki, G.B. 1989, ApJ, 338, 277
Pretorius, M. L., Knigge, C., O'Donoghue, D., Henry, J. P., Gioia, I. M., Mullis, C. R. 2007, MNRAS, 382, 1279
Pretorius, M. L., & Knigge, C. 2008, MNRAS, 385, 1485
Pretorius, M.L., & Knigge, C. 2012, MNRAS, 419, 1442
Pretorius, M.L., Knigge, C., & Schwope, A.D. 2013, MNRAS, 432, 570
Pretorius, M.L. & Mukai, K. 2014, MNRAS, 442, 2580
Portegies Zwart, S.F., Hut, P., McMillan, S.L.W., & Verbunt, F. 1997, A& A, 328, 143
Posquato, M., de Luca, A., Raimondo, G., Carini, R., Moraghan, A., Chung, C., Brocato, E., & Lee, Y-W. 2014, ApJ, 789, 28
Ramsay, G., Groot, P.J., Marsh, T.R., Nelemans, G., Steeghs, D. & Hakala, P. 2006, A&A, 457, 623
Randall, S.K., Calamida, A., Fontaine, G., Monelli, M., Bono, G., Alonso, M.L., Van Grootel, V., Brassard, P., Chayer, P., Catelan, M., Littlefair, S., Dhillon, V.S., & Marsh, T.R. 2016, A& A, 589,1

Rebassa-Mansergas, A., Parsons, S.G., Garcia-Berro, E., Gansicke, B.T., Schreiber, M.R., Rybicka, M., & Koester, D. 2017, MNRAS, 466, 1575
Reed, M.D., Eggen, J.R., Harms, S.L., Telting, J.H., Ostensen, R.H., O'Toole, S.J., Terndrup, D.M., Zhou, A.Y., Kienenberger, R.L., & Heber, U. 2009, A& A, 493, 175
Reimers, D. 1975, MSRSL, 8, 369
Reimers, D., & Koester, D. 1982, A& A, 116, 341
Renzini, A., & Fusi Pecci, F. 1988, ARA& A, 26, 199
Riley, A., et al. 2017, "STIS Instrument Hanbook", Version 16.0, (Baltimore: STScI)
Roelofs, G. H. A., Nelemans, G., & Groot, P. J. 2007, MNRAS, 382, 685
Ruiter, A.J., Belczynski, K., & Fryer, C. 2009, ApJ, 699, 2026
Sandage, A.R. 1953, AJ, 58, 61
Sandage, A. & Tammann, G. A. 2006, ARA & A, 44, 93
Sarajedini, A., Chaboyer, B. & Demarque, P. 1997, PASP, 109, 1321
Saviane, I., Piotto, G., Fagotto, F., Zaggia, S., Capaccioli, M., & Aparicio, A. 1998, A & A, 333, 479
Sawyer, H.B. 1938, JRASC, 32, 69
Sawyer Hogg, H. & Wehlau, A. 1964, JRASC, 58, 163
Scargle, J. D. 1982, ApJ, 263, 835
Schirbel, L., Melendez, J., Karakas, A.I., Ramirez, I., Castro, M., Faria, M.A., Lugaro, M., Asplund, M., Tucci Maia, M., Yong, D., Howes, L., & do Nascimento, J.D. 2015, A& A, 584, 116
Shara, M. M., & Drissen, L. 1995, ApJ, 448, 203
Shara, M.M., Bergeron, L.E., Gililand, R.L., Saha, A., & Petro, L. 1996, ApJ, 471, 804
Shara, M.M., & Hurley, J. 2002, ApJ, 571, 830
Shara, M.M., Zurek, D.R., Baltz, E.A., Lauer, T.R., & Silk, J. 2004, ApJL, 605, 117
Shara, M. M., Hinkley, S., Zurek, D. R., Knigge, C., & Dieball, A. 2005, AJ, 130, 1829
Shara, M.M., & Hurley, J. 2006, ApJ, 646, 464
Shara, M.M., Mizusawa, T., Zurek, D., Martin C.D., Neill, J.D., & Seibert, M. 2012, ApJ, 756, 107
Shara, M.M., Wilde, M., Zurek, D. 2017, in preparation
Skillman, D. R., Patterson, J., Kemp, J., Harvey, D. A., Fried, R. E., Retter, A., Lipkin, Y., & Vanmunster, T. 1999, PASP, 111, 1281
Sokoloski, J.L. & Bildsten, L. 1999, ApJ, 517, 919
Solheim, J.-E., Provencal, J. L., Bradley, P. A., Vauclair, G., Barstow, M. A., Kepler, S. O., Fontaine, G., Grauer, A. D., Winget, D. E., Marar, T. M. K., Leibowitz, E. M., Emanuelsen, P.-I., Cheverton, M., Dolez, N., Kanaan, A., Bergeron, P., Claver, C. F., Clemens, J. C., Keinman, S. J., Hine, B. P., Seetha, S., Ashoka, B. N., Mazeh, T., Sansom, A.E., Tweedy, R. W., Meistas, E. G., Bruvold, A., Massacand, C. M. 1998, A & A, 332, 939
Solheim, J.-E. 2010, PASP, 122, 1133
Steinfadt, J.D., Bildsten, L., & Arras, P. 2010, ApJ, 718, 441

Stetson, P.B. 1994, PASP, 106, 250
Stetson, P.B., Vandenberg, D.A. & Bolte, M. 1996, PASP, 108, 560
Strader, J., Chomiuk, L., Maccarone, T.J., Miller-Jones, J.C.A., & Seth, A.C. 2012 Nature, 490, 71
Thomson, G. S., Dieball, A., Knigge, C., Long, K. S., & Zurek, D. R. 2010, MNRAS, 406, 1084
Thomson, G.S., Knigge, C., Dieball, A., Maccarone, T.J., Dolphin, A., Zurek, D., Long, K.S., Shara, M., & Sarajedini, A. 2012, MNRAS, 423, 2901
Urpin, V., Geppert, U., & Konenkov, D. 1998, A& A, 331, 244
VandenBerg, D.A., Bolte, M., & Stetson, P.B. 1996, ARA& A, 34, 461
VandenBerg, D.A. 2000, ApJS, 129, 315
VandenBerg, D.A., Bergbusch, P.A., Ferguson, J.W., & Edvardsson, B. 2014, ApJ, 794, 72
Vennes, S. 1999, ApJ, 525, 995
Walker, A.R. 1992, PASP, 104, 1063
Wang, B., & Han, Z. 2012, NewAR, 56, 122
Warner, B. 1995, Cataclysmic Variable Stars, Cambridge University Press
Watson, A. M., Mould, J. R., Gallagher, J. S., Ballester, G. E., Burrows, C. J., Casertano, S., Clarke, J. T., Crisp, D., Griffiths, R. E., Hester, J. J., Hoessel, J. G., Holtzman, J. A., Scowen, P. A., Stapelfeldt, K. R., Trauger, J. T., & Westphal, J. A. 1994, ApJL, 435, 55
White, S.D., & Frenk, C.S. 1991, ApJ, 379, 52
Wheatley, P.J., Mukai, K., & de Martino, D. 2003, MNRAS, 346, 855
Wheatley, J.M., Welsh, B.Y., Siegmund, O.H.W., Byun, Y.-I., Yi, S., Lee, Y.-W., Madore, B.F., Viton, M., Rich, R.M., Bianchi, L., Barlow, T.A., Donas, J., Forster, K., Friedman, P.G., Heckman, T.M., Jelinsky, P.N., Malina, R.F., Martin, D.C., Milliard, B., Morrissey, P., Neff, S.G., Schiminovich, D., Small, T., Szalay, A.S., & Wyder, T.K. 2005, ApJL, 619, 123
Whitmore, B.C., Gilmore, D., Leitherer, C., Fall, S.M., Chandar, R., Blair, W.P., Schweizer, F., Zhang, Q., Miller, B.W. 2005, AJ, 130, 2104
Willson, L. A. & Marengo, M. 2012, JAVSO, 40, 516
Yaron, O., Prialnik, D., Shara, M.M., & Kovetz, A. 2005, ApJ, 623, 398
Yuasa, T., Nakazawa, K., Makishima, K., Saitou, K. Ishida, M., Ebisawa, K., Mori, H. & Yamada, S. 2010, A&A, 520, 25
Zurek, D., Knigge, C., Maccarone, T.J., Dieball, A. & Long, K.S. 2009, ApJ, 699, 1113
Zurek, D., Knigge, C., Maccarone, T.J., Pooley, D., Dieball, A., Long, K.S., Shara, M.M., & Saradejini, A. 2016, MNRAS, 460, 3660